INFORMATION TO USERS

This dissertation was produced from a microfilm copy of the original document. While the most advanced technological means to photograph and reproduce this document have been used, the quality is heavily dependent upon the quality of the original submitted.

The following explanation of techniques is provided to help you understand markings or patterns which may appear on this reproduction.

1. The sign or "target" for pages apparently lacking from the document photographed is "Missing Page(s)". If it was possible to obtain the missing page(s) or section, they are spliced into the film along with adjacent pages. This may have necessitated cutting thru an image and duplicating adjacent pages to insure you complete continuity.

2. When an image on the film is obliterated with a large round black mark, it is an indication that the photographer suspected that the copy may have moved during exposure and thus cause a blurred image. You will find a good image of the page in the adjacent frame.

3. When a map, drawing or chart, etc., was part of the material being photographed the photographer followed a definite method in "sectioning" the material. It is customary to begin photoing at the upper left hand corner of a large sheet and to continue photoing from left to right in equal sections with a small overlap. If necessary, sectioning is continued again — beginning below the first row and continuing on until complete.

4. The majority of users indicate that the textual content is of greatest value, however, a somewhat higher quality reproduction could be made from "photographs" if essential to the understanding of the dissertation. Silver prints of "photographs" may be ordered at additional charge by writing the Order Department, giving the catalog number, title, author and specific pages you wish reproduced.

University Microfilms

300 North Zeeb Road
Ann Arbor, Michigan 48106

A Xerox Education Company

The Pennsylvania State University

The Graduate School

Department of Mechanical Engineering

Non-Isothermal Gaseous Flow Through Fine Pored Media

A Thesis in

Mechanical Engineering

by

Mason Harold Somerville

Submitted in Partial Fulfillment
of the Requirements
for the Degree of

Doctor of Philosophy

March 1972

Date of Approval:

Feb. 14, 1972 — Donald R. Olson
Professor of Mechanical Engineering
Thesis Co-Adviser

Feb 12, 1972 — Carl H. Wolgemuth
Associate Professor Mechanical Engineering
Thesis Co-Adviser

Feb 14 1972 — Richard G. Cunningham
Professor and Head of the
Department of Mechanical Engineering

ACKNOWLEDGMENTS

The author wishes to express his sincerest appreciation to his adivsers, Dr. Carl H. Wolgemuth and Dr. Donald R. Olson, for their many helpful suggestions and encouragement throughout the research project. Particular thanks are due Dr. Wolgemuth for his aid throughout the entire research project.

The author would also like to thank Mr. George Norton and the men under him for their aid and advice in the building of the experimental equipment. Thanks also go to Mr. Curtis Hunt and the men under him, who, on occasion, aided the author in restoring the experimental equipment to its proper condition.

The financial support of both the Mechanical Engineering Department, and of the Ordnance Research Laboratory of The Pennsylvania State University under contract with the Naval Ordnance Systems Command is sincerely appreciated.

TABLE OF CONTENTS

TABLE OF CONTENTS (CONT.)

TABLE OF CONTENTS (CONT.)

LIST OF FIGURES

LIST OF FIGURES (CONT.)

LIST OF FIGURES (CONT.)

LIST OF TABLES

NOMENCLATURE

Symbol	Description
A	Cross-sectional are, cm^2
A_P	Pore Cross-sectional area, cm^2
A_s	Surface cross-sectional area, cm^2
a	Pore hydraulic radius, μm
a_m	Median pore hydraulic radius, μm
ao	Optical balance factor, dimensionless
$\bar{a}$	Mean pore hydraulic radius, μm
B	Porous medium area property, dimensionless
B_o	Porous medium area property, cm^2
C	Proportionality constant, dimensionless
c	Proportionality constant, dimensionless
F	Attenuation factor, decibels
f	Fraction of molecules undergoing diffuse reflection,dimensionless
f_m	Maximum pore frequency, dimensionless
$f(I_a)$	Number of pores in the class interval I_a, dimensionless
I_a	Class interval of radii, cm
J	Sutherlands constant, 104 for N_2, °K
K	Permeability, cm^2/sec
K_r	System response factor, cm^2-ster-volt/watt

NOMENCLATURE (CONT.)

Symbol	Description
K_s	Slip permeability coefficient, cm
KN	Local Knudsen number $2a/\lambda$ dimensionless
KN_r	Reference Knudsen number, $2a_m/\lambda(P_H, T_L)$, dimensionless
KN_c	Cut-off Knudsen number, dimensionless
k	Porous medium constant for the continuum regime, dimensionless
k'	Porous medium constant for the slip regime, dimensionless
k_a	Pore shape factor for the continuum regime, dimensionless
k_b	Pore shape factor for the slip regime, dimesnionless
L	Thickness of the porous medium, cm
l_f	Focal loss factor, dimensionless
M	Slope of the ϕ versus ln(a) curve, $cm^2/(ln(\mu m)cm^2)$
$\dot{m}$	Gaseous mass flux, gms/cm^2-sec
N	Probability exponent, dimensionless
$\overline{N}_c$	Background radiance, $watts/cm^2$-ster
$\overline{N}_r$	Reference radiance, $watts/cm^2$-ster
$\overline{N}_t$	Target radiance, $watts/cm^2$-ster
n	Number of capillary tubes, dimensionless
P	Absolute pressure, lb_f/in^2
P_p	Pore perimeter, cm

NOMENCLATURE (CONT.)

Symbol	Description
p	Absolute pressure, dynes/cm^2
$\bar{p}$	Average absolute pressure, dynes/cm^2
Q	Volume flow rate, cc/sec
q	Tortuosity, ratio of effective to actual medium thickness, dimensionless
R	Specific gas constant, dyne-cm/gm-°K
r	Radial coordinate, cm
RM	Ratio of pressure to temperature driving forces, dimensionless
S	Pore surface area, cm^2/gm
SA	Attenuation factor, dimensionless
T	Absolute temperature, °K
T_r	Reference absolute temperature, °K
V	Volume, cm^3
V_{out}	Output radiometer voltage, volts
V_{ETO}	Electronic Temperature Offset voltage, volts
V_T	Medium geometric volume, cm^3
v	Specific volume, cm^3/gm
$\bar{v}$	Mean molecular velocity, cm/sec
W	Specific work, dyne-cm/gm
x	Axial coordinate, cm
α	Cylindrical angle coordinate, degrees
Δ	Difference between inlet and outlet conditions

NOMENCLATURE (CONT.)

Symbol	Description
∇	The operator: $\frac{\partial}{\partial x} + \frac{\partial}{\partial y} + \frac{\partial}{\partial z}$, cm^{-1}
δ	An empirical medium constant representing the portion of diffuse reflections, dimensionless
ε	Porosity, cm^3/gm
ζ	Slip distance, cm
η	Absolute viscosity, dyne-sec/cm^2
η_r	Reference absolute viscosity, 174 x 10^{-6} poise for N_2, dyne-sec/cm^2
θ	Contact angle, degrees
λ	Mean free path, cm
μ	Micrometer, 10^{-6} meters
π	3.14159 ..., dimensionless
ρ	Density, gm/cc
ρ_m	Porous medium, density, gm/cc
$\overline{\rho}$	Average density, gm/cc
σ	Surface tension, dynes/cm
ϕ	Cumulative specific area, cm^2/cm^2
ϕ_m	Maximum cumulative specific area, cm^2/cm^2
ϕ_o	Original cumulative specific area, cm^2/cm^2

Subscripts

c	Continuum flow contribution
e	Effective property of gas-porous media interaction
f	Free molecule contribution

NOMENCLATURE (CONT.)

Subscripts

H	Maximum value
L	Minimum value
S	Slip flow contribution
t	Thermal creep contribution
x	Denotes values of medium properties associated with the smallest pore radius used
y	Denotes values of medium properties associated with the largest pore radius used
0	Inlet state conditions
1	Outlet state conditions

Superscripts

*	Denotes a nondimensionalized variable

CHAPTER I

INTRODUCTION

1.1 General Statement of the Problem

Gaseous flow through porous media encompasses many fields and applications. Continuum flow applications, such as encountered in gas recovery and turbine blade cooling, are widely recognized. However, some of the porous media being used in gas cooled reactors and fuel cells have very fine or small pores and present a more difficult modeling problem to the designer. This research is directed toward the modeling of a gaseous flow in a fine pored porous medium under non-isothermal conditions where both continuum and free molecular phenomena occur and interact.

The modeling of such a gas-porous medium interaction has two major problem areas, the description of the porous medium itself, and a description of a flow characteristics of the gas.

1.2 The Porous Medium

Generally speaking, the pore diameters of a porous medium will vary; as a result, a pore diameter distribution is used to represent the porous medium. Of fundamental importance is the determination of the pore size distribution that characterizes the porous medium from a hydraulic point of view. Previous attempts to determine this distribution have been largely unsuccessful. Fuel cell grade carbons have median

pore diameters that commonly vary from 0.01μ to 15μ with pore size distributions that vary over two orders of magnitude. In this research project, only isotropic porous media, those whose pore size distributions are plane independent, were considered. Typical median pore diameters of the fine pored media studied range from 0.5μ to 10μ.

1.3 Gaseous Flow Phenomena in Fine Pored Media

The descriptions of gaseous flow phenomena fall into two fundamental regimes, continuum and free molecular. In the continuum regime the molecules of the gas interact much more frequently with one another than they do with the porous medium; as opposed to free molecular behavior where they interact much more frequently with the porous medium. The transition, or slip regime is that regime where the probability of a molecule-molecule collision is of the same order as the probability of a molecule-wall collision.

Continuum and free molecular flow are quite different in several respects. The most important of these is that the temperature gradient acts as a driving force in the free molecular regime, while it does not in the continuum regime. On the other hand, the density and viscosity have temperature effects in the continuum regime but not in the free molecular regime. Another distinction is that the free molecular mass flux is thought to be proportional to the hydraulic radius while the continuum mass flux is proportional to the square of the hydraulic radius (1)*.

---

*Numbers in parenthesis refer to items in the bibliography.

Free molecular flow phenomena are encountered if the density of gas is low (10^{-5} gm/cc) and/or the characteristic hydraulic dimension is small ($\sim$ .1μ). A porous medium that can support free molecular flow at ordinary pressures is considered to be fine pored. Because most media have a pore size distribution, it is conceivable that a fine pored porous media could support both free molecular and continuum flow.

1.4 Research Objective

The objective of this work was to model a gaseous flow through fine-pored porous media under non-isothermal conditions. Specifically, the parameters governing the flow were to be determined, evaluated and utilized in an alytical model of the gas-porous media interaction. In addition, the results of the study were to be compared with the results of experimental flow tests. The experimental effort consisted of two parts, determination of the pore size distribution and the experimental evaluation of the flow characteristics of several porous media.

CHAPTER II

A REVIEW OF EXISTING, PERTINENT WORK

2.1 Introduction

As previously mentioned, the description of gaseous flow through porous media has two major areas of concern: the description of the medium itself and a description of the flow phenomena. Some studies are concerned with only one of the above areas; the majority of such studies are in the former area, while others consider both areas. For this reason the review will be divided into two parts: a review of the techniques used to describe porous media, and a review of existing flow studies and models.

2.2 Techniques Used to Describe Porous Media

A photomicrograph of a polished cross section of a typical porous carbon (Figure 1) shows that the pores vary in size and shape. There are at least three methods of collecting experimental data that can be used to characterize such a porous medium: the mercury porosimeter, a technique utilizing the scanning electron microscope, and flow studies. The last technique will be discussed in Section 2.3 of this chapter; the first two will be discussed here.

2.2.1 Determination of Pore Diameter Distribution and Other Porous Media Flow Parameters.

Washburn (2) and Washburn and Bunting (3) were the first workers to suggest that a pore diameter could

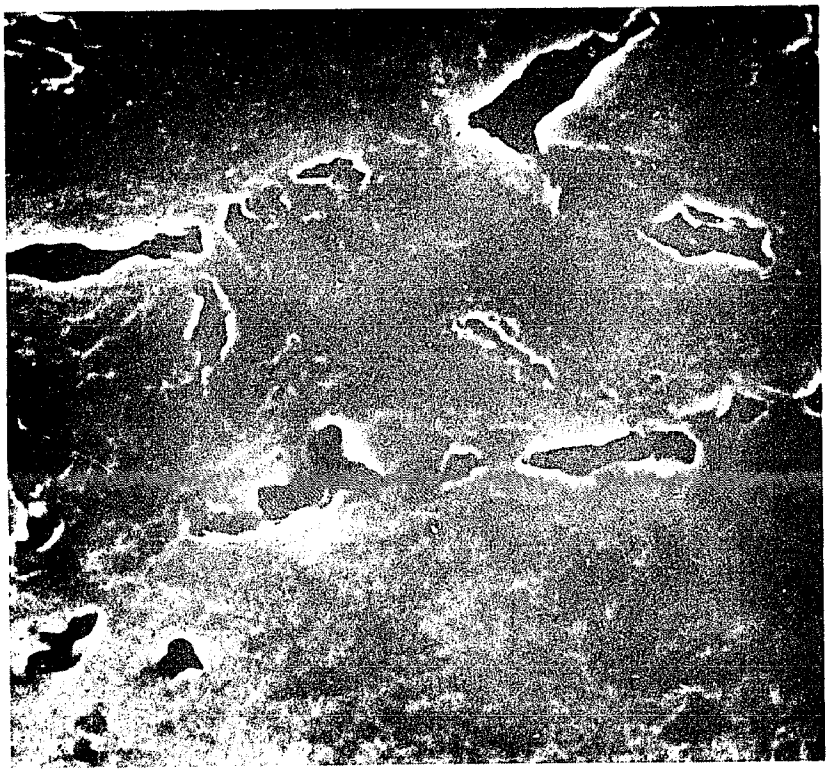

Figure 1 - SEM Photomicrograph, FC-25, Unfilled at 3000 X

be determined by the phenomenon of capillary depression. They determined that the minimum pressure, p, required to force a non-wetting liquid into a pore of radius, a, is:

$$p = \frac{2\sigma \cos \theta}{a} \quad , \tag{2.1}$$

where θ is the contact angle (greater than 90° for a non-wetting fluid), and σ is the surface tension of the liquid. Subsequently, this technique was used to determine the pore diameter distribution of a porous material (4). The experimental method was further extended to include pore diameters as small as 0.004μ and as large as 200μ (5,6).

All of the above authors make two fundamental assumptions which are presently used in the commercial determination of pore size distributions. These assumptions are that the pore is circular in cross section [i.e., that Equation (2.1) may be used to determine pore size], and the wetting angle, θ, of mercury is constant at 130°.

From Figure 1, it is obvious that the pores are not circular. The assumption that the pores are of circular cross section may lead to qualitatively, as well as quantitatively, incorrect conclusions (7). Furthermore, the contact angle of mercury has been found to vary between 112° and 142° (8) introducing the possibility of an error in pore radius as large as ±20%. Further errors in this technique are examined by Bickerman (9). Thus, there is some uncertainty concerning the validity of the mercury penetration technique; nevertheless, it is the most popular technique for determining the pore diameter distribution. There are several commercially available porosimeters (8, 10).

The experimental result of a mercury penetration test of a porous sample is a set of data relating the cumulative absorption of the mercury (cc) to the pressure (psia) required to fill the sample with that quantity of mercury. A typical set of mercury porosimeter data is shown in Figure 2. The porosity of the sample is determined by dividing the cumulative volume of the mercury by the apparent (geometric) volume of the sample. The pore radius is determined from Equation (2.1). A mercury penetration experiment on a single rigid porous specimen would yield the pore size distribution directly, where all cracks, crevices, holes, and fissures are termed pores.

The surface area of the pores may be determined from a mercury penetration experiment in the following fashion (8). The work, dW, required to immerse an area, dS, of a non-wetting powder in mercury is:

$$dW = - \sigma \cos \theta \cdot dS \quad , \tag{2.2}$$

and since the work is done by an external pressure force,

$$dW = p \, dV \quad . \tag{2.3}$$

The surface area, S, can be found by solving Equations (2.2) and (2.3) yielding,

$$S = - \frac{\int p \, dV}{\sigma \cos \theta} \quad . \tag{2.4}$$

The surface area, determined by either the above techniques or from adsorption tests, is used by some authors together with the specific displaced volume (cc/gm) to define an average hydraulic radius.

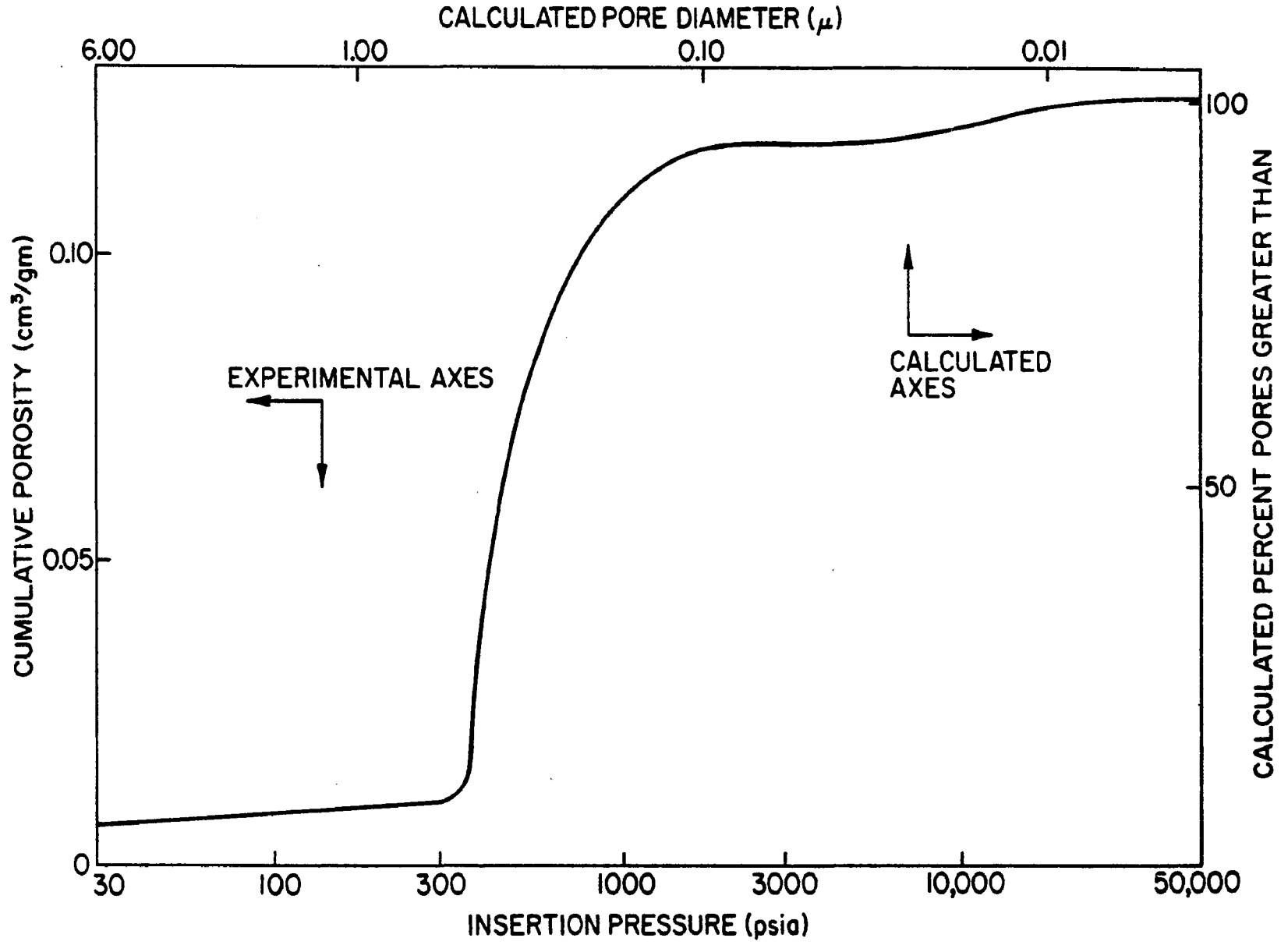

Figure 2 - Cumulative Porosity

2.2.2 A Technique Utilizing the Scanning Electron Microscope.

In this technique, the porous medium to be analyzed is sectioned, polished and inserted into the scanning electron microscope (SEM). The SEM is basically an electronic device that directs a beam of electrons across the specimen surface in a rapid scanning fashion. The result of the impinging electron beam hitting the surface is that the surface emits back scattered and secondary electron beams which are detected within the microscope. The resultant electronic signal from a detector is then amplified and displayed on a cathode ray tube. Figure 1 is a photograph of such a display. In addition to the above display, the amplified electronic signal from the detectors can be digitized and stored on a magnetic tape. The data can then be analyzed and reduced on a digital computer (11).

This technique has one major assumption. In the electronic processing of the image, a cut-off signal voltage level must be chosen by the user. The chosen voltage level determines which data will be counted as pores in the analysis. A satisfactory level is chosen by considering both the resulting statistics and a comparison of the computer representation of the surface with a photograph of the surface. Utilizing this technique, one can obtain the distribution of the ratio of the pore's cross-sectional area to its perimeter.

2.3 Some Previous Experiments and Analytical Flow Studies

The problem of modelling the flow of a gas through a porous medium is concerned not only with the mechanics of the gas but also with

the properties of the medium itself. As a result of this, the determination of the properties of the medium restricting the flow is an important, and usually integral, part of most studies.

2.3.1 Background. Gaseous flow in most porous media obeys Darcy's Law which is (12):

$$\overline{Q}p = + KA \frac{\Delta P}{L} \quad , \tag{2.5}$$

where Q is the volume flow rate, K the permeability, A the cross-sectional area, ΔP the pressure drop across the medium, $\overline{p}$ the mean pressure, and L the thickness of the sample. Darcy's Law is a good representation of common gaseous flow through porous media under isothermal conditions. The volume flow through a capillary tube of circular cross-section under laminar, incompressible flow conditions is given by Equation (2.5) with the permeability, K,

$$K = \frac{a^2}{8\eta} \overline{p} \quad , \tag{2.6}$$

where η is the viscosity.

Because of the similarity between Equation (2.5) as applied to a single tube and applied to a porous medium, many authors have chosen to use bundles of capillary tubes as the basis for a model of the porous medium. That is, Equation (2.5) infers that some material or medium constant, B_o, could be determined by:

$$B_o = \frac{K\eta}{\overline{p}} \tag{2.7}$$

and then related to porous media properties.

Unfortunately, Equations (2.5) and (2.7) do not adequately account for all the flow phenomena encountered in porous media, particularly slip and free molecular flow, and non-isothermal phenomena.

Slip flow (actual movement of the gas immediately adjacent to the boundary) will occur in a tube when the Knudsen number (the ratio of the tube diameter to the mean free path of the gas) is greater than 0.1 and less than 10 (13). A similar phenomenon occurs in a porous medium at similar Knudsen numbers where the Knudsen number is based upon the hydraulic diameter of the pore (14).

The permeability, K for a capillary tube in which slip flow is occurring is given by (15):

$$K = \frac{a^2 \bar{p}}{8\eta} + \frac{\pi a \bar{v}}{8}\left(\frac{2-f}{f}\right) \quad , \tag{2.8}$$

where

$$\bar{v} = \sqrt{8RT/\pi} \tag{2.9}$$

is the mean molecular velocity and f denotes the fraction of molecules undergoing diffuse, rather than specular, reflection at the wall. It should be noted that the material constant in the slip regime, given by Equation (2.7), is no longer independent of the mean pressure. By using the Chapman-Enskog relation for the mean free path,

$$\lambda = 2\eta/\bar{\rho}\,\bar{v} \quad , \tag{2.10}$$

it can be shown that

$$B_o = \frac{a^2}{8}\left(1 + \frac{4c\lambda}{a}\right) \quad , \tag{2.11}$$

in the slip regime. Thus the permeability constant of a porous medium, B_o, becomes a function of the pressure of the gas as λ is a function of pressure (16).

If the mean pressure of the gas is very low and the Knudsen number is less than 0.1, then free molecular flow is thought to occur within a porous medium (17). The flow through a capillary tube under isothermal conditions is given as (18):

$$\overline{Qp} = \frac{2\pi}{3}\left(\frac{2-f}{f}\right)\ \overline{v}\ a^3\ \frac{\Delta P}{L} \quad , \tag{2.12}$$

where all molecules are assumed to be reflected diffusely (f=1).

By using the definition of the permeability [Equation (2.5)] it can be shown that the free molecular permeability is

$$K = \frac{2}{3}\left(\frac{2-f}{f}\right)\ \overline{av} \quad . \tag{2.13}$$

The capillary model was adapted to porous media by using the following porous media parameters: the porosity, ε; the pore surface area per unit volume, S, as determined by BET adsorption tests or from mercury porosimeter tests; the tortuosity, q, defined as the ratio of the effective to apparent thickness (19) and shape factors, k_a and k_b. A mean hydraulic radius can then be defined as (19):

$$\overline{a} = \varepsilon/S \quad . \tag{2.14}$$

2.3.2 Previous Models Based on the Capillary Tube Concept.

Adzumi (20) was the first author to attempt to model the gaseous flow phenomena in a porous medium. He based his model on n capillary tubes of mean radius a. His resultant expression for the permeability took the form:

$$K = \frac{na^2}{8\eta} \bar{p} + \delta \frac{2na}{3} \bar{v} \quad , \tag{2.15}$$

where δ accounts for specular reflection and is less than unity.

Adzumi experimentally determined that the permeability was a linear function of the mean pressure with a non zero intercept for the media tested. He was unable to predict the quantitative values of the slope and intercept of the permeability versus mean pressure curve. This failure was attributed to his description of the porous medium and led to further research in describing porous media.

Holmes (21) reasoned that the effective area of the medium, A_e, was proportional to the porosity in the following fashion:

$$\frac{A_e}{A_S} = \frac{V_e}{V_T} = \varepsilon \quad , \tag{2.16}$$

and that the mean hydraulic radius was given by Equation (2.14). The porous medium permeability under free molecular conditions can then be shown to be (21):

$$K = \frac{4}{3} \bar{v} \frac{\varepsilon^2}{S} \quad . \tag{2.17}$$

Carman and Arnell (19) hypothesized that a gas molecule traversing a porous medium traveled a distance greater than the nominal thickness of that medium. The ratio of the effective distance traveled to the nominal thickness is the tortuosity. The area ratio was then hypothesized to be equal to (19):

$$\frac{A_e}{A_S} = \frac{\varepsilon}{q} \quad . \tag{2.18}$$

The porous medium permeability is given by (19):

$$K = \frac{\varepsilon^3 \overline{p}}{k\eta S^2} + \frac{4}{3}\frac{\delta}{k'}\frac{\varepsilon^2}{S}\overline{v} \tag{2.19}$$

with

$$k = \frac{1}{k_a q^2} \tag{2.20}$$

and

$$k' = \frac{1}{k_b q^2} \quad , \tag{2.21}$$

where k_a and k_b are shape factors of the porous medium for the continuum and slip flow regimes, respectively. Since ε, k, k', and S are all functions of the porous medium, Equation (2.19) can be express in the following form (22):

$$K = \frac{B_o \bar{p}}{\eta} + \frac{4}{3} K_o \bar{v} \quad . \tag{2.22}$$

The work of Hutcheon et. al., (23), Barrer and Strachan (24) and Ford (25) demonstrates that Equation (2.22) is a good representation of isothermal gaseous flow through porous media.

The model represented by Equation (2.19) has several drawbacks which subsequent authors have pointed out. Ash and Grove (26) have questioned the use of the pore surface area to determine the mean hydraulic radius. Owen (27) has pointed out that the tortuosity as determined from electrical conductivity tests may not represent the gaseous flow tortuosity. Hewitt (28) completed a study utilizing liquid bismuth in which he shows that the factors k and k' in Equation (2.19) are not solely properties of the material and that they do not necessarily represent constants for a particular material. Pollard and Present (29) showed analytically that the graph of the permeability versus the mean pressure should not exhibit a minimum if the gas molecules follow a tortuous path in traversing the porous medium. Grove and Ford (25) present experimental data indicating the existence of a minimum in the permeability curve.

The isothermal model represented by Equation (2.19) requires the evaluation of six experimental constants, (k_a, k_b, q, S, δ, ε), thereby demanding a fairly extensive experimental effort on the part of the user. Another disadvantage of the model is that it represents only isothermal flow. Hanley (17) and Lammers (30) have both observed thermal pumping effects in a fine-pored medium, indicating that a new model should account for temperature gradient effects.

2.3.3. Other Models. Evans, Watson, and Mason (31, 32, 33) used statistical mechanics to model the gas-porous medium interaction. They envisioned the gas as interacting with large dust particles, which represented the porous medium. Their model has the advantage that the entire Knudsen number range can be formally represented and that there are fewer adjustable parameters than in the above capillary model and in the models of Weber (34) and Liang (35). The disadvantages are that the porous medium is difficult to describe and that the porosity and tortuosity are retained as meaningful properties. However, their model does predict the Knudsen minimum in the permeability curve for a capillary tube. Hanley (17) presented an experimental verification of Evan's, Watson's and Mason's work.

Other authors have tried similar approaches to the one above; for example, Broadbent and Hammersley (36) present a model based on a Monte Carlo approximation to the gas-porous medium interaction.

2.4 Summary

There are three types of models of the gas-porous medium interaction available in the literature: the capillary model, the statistical model of Evans et. al., and the random model of Broadbent and Hammersley.

The models of Evans et. al., and Broadbent and Hammersley are fundamental in nature and do not attempt to independently model the gas or the medium. The disadvantage here is that the properties of the medium that control the flow in the model are not easily determined from the physical properties of the medium itself. Although the models do

predict the qualitative behavior of the system over the entire Knudsen number range, the quantitative application of the models to a new medium with different properties is difficult. Unfortunately, the model of Evans et. al., retains the use of the porosity, pore surface area and tortuosity which, as the literature search has shown, is open to question.

The capillary models, as a general rule, predict the behavior of the flow quite well in the continuum regime under isothermal conditions. However, the choice of constants and parameters has forced the models based on capillaries to be largely empirical and quite limited in application. Furthermore, the present capillary models do not predict the existence of a minimum in the permeability versus mean pressure curve.

In light of the existing literature, the general differential equations of capillary flow were retained, but the parameters needed to describe the gas-porous medium were altered. In addition, the effects of a temperature gradient were accounted for, as this could change the pressure profile in a porous medium significantly ($\sim$ 20%), and is encountered in the design of fuel cells, gas recovery work, and nuclear reactor design.

CHAPTER III

ANALYTICAL MODEL OF THE GAS-POROUS MEDIUM INTERACTION

3.1 Introduction

The majority of the work concerned with the capillary model indicates that behavior of a gas in a porous medium is similar to the behavior it exhibits in a capillary tube; indicating that the governing differential equations of the two flow situations are similar. The parameters of hydraulic radius, as defined by Equation (2.14), tortuosity and pore shape factor do not seem to contribute sufficiently to the model to merit their continued use, especially in the light of the questions that were raised by the literature search. Thus, an effort was undertaken to determine new and meaningful properties of the porous media related to flow. An effort was also made to include the effects of a temperature gradient upon the medium and the flow rate. The literature search indicated that the central difficulty lay in modelling the porous medium itself, while the mechanical behavior of the gas seemed to be fairly well understood, with the exception of the effects of the temperature gradient.

In this Chapter an unpublished model of the porous medium and of the gas-porous medium system is presented. The two new models eliminate the empirical constants presently used and allow the permeability characteristics of a porous medium to be determined from a knowledge of the pore size and temperature distributions of the medium.

3.2 Mathematical Description of the Flow Regimes

3.2.1 Continuum Flow Regime. The flow is assumed to be in the continuum region, if the Knudsen number is greater than 10. Here, it is assumed that the gas properties are independent of the radius, that the radial velocity component of the flow is small in comparison to the axial flow component and that the flow is steady ($\dot{m}$ = constant). Then, if the Mach number is low, an expression for the mass flux in a capillary tube,

$$\dot{m}_c = - \frac{\rho a^2}{8\eta} \nabla P \quad , \tag{3.1}$$

can be determined in terms of the density, ρ, viscosity, η, radius, a, and the pressure gradient ∇P. Here, "a" is assumed to represent the hydraulic radius of a pore and, thus, Equation (3.1) represents the mass flux through a pore of radius a, not through a porous medium of mean hydraulic radius, $\bar{a}$, as defined by Equation (2.14).

The viscosity, η, in Equation (3.1) is determined from Sutherlands relationship (37):

$$\eta = \eta_r \left(\frac{T_r + J}{T + J} \right) \left(\frac{T}{T_r} \right)^{3/2} \quad , \tag{3.2}$$

where T_r, η_r, and J are constants for a particular gas.

The density, ρ, is assumed to follow the ideal gas equation of state because the gas is at a low pressure ($P/P_{critical} < 0.1$), thus,

$$\rho = P/RT \quad , \tag{3.3}$$

where R is the specific gas constant, T, the absolute temperature and P, the absolute pressure. If the mass flux is assumed one-dimensional, then,

$$\nabla P = dP/dx \quad . \tag{3.4}$$

3.2.2 Slip Flow Regime. If the Knudsen number lies in the regime of 0.1 to 10, then two new phenomena are encountered: a movement of the gas immediately adjacent to the wall of the container due to the decreased pressure (referred to as slip flow) and a movement of the gas adjacent to the wall due to a temperature gradient (thermal creep). The slip phenomena can be modelled by the use of a coefficient of slip (38)

$$\xi \equiv u / \left(\frac{dv}{dr}\right)_{wall} \quad ,$$

where u is the velocity of the gas at the wall and $\frac{dv}{dr}$ the axial velocity gradient at the wall. This definition is analogous to moving the wall out a distance ξ, where the relative velocity of the gas adjacent to the wall would be zero. The thermal creep contribution to the mass flux can be shown to be (39):

$$\dot{m}_t = \frac{3\eta}{4T} \nabla T \quad . \tag{3.5}$$

The total mass flux in the transition (slip) regime can be found by summing the continuum contribution [Equation (3.1)] with the thermal creep contribution [Equation (3.5)] and the slip contribution, $(-4\rho\xi a^2/(8\eta a)\ \nabla P)$. Thus, the total mass flux in the transition regime is:

$$\dot{m}_s = -\frac{\rho a^2}{8\eta}\left(1 + \frac{4\xi}{a}\right)\nabla P + \frac{3\eta}{4T}\nabla T \quad , \tag{3.6}$$

where ξ is the slip distance at the wall of the tube and $\dot{m}_s$ is the mass flux through a passage with hydraulic radius, a, in the slip regime. It should be noted that both slip and thermal creep can increase the flow rate.

3.2.3 Free Molecule Regime. If the probability of a gas molecule hitting the wall of a container is much higher than its probability of hitting another molecule, then the gas is said to be in free molecule regime. This condition commonly occurs if the Knudsen number is less than 0.1. In this regime, the flow through a capillary tube is given by (39):

$$\dot{m}_f = -\frac{4}{3}\sqrt{\frac{2\pi}{R}}\, a\, \nabla\left(P/\sqrt{T}\right) \quad . \tag{3.7}$$

Through suitable algebraic manipulations, one can expand this to the following form:

$$\dot{m}_f = -\frac{16}{3}\frac{a}{v}\left[\nabla P - \frac{P}{2T}\nabla T\right] \quad . \tag{3.8}$$

It should be noted that it is possible to have a mass flux due solely to a thermal gradient (i.e., under isobaric conditions) in both the free molecule case [Equation (3.8)] and in the slip case [Equation (3.6)]. Note that in the free molecule regime the ratio of the pressure contribution to the thermal contribution is

$$RM = \frac{\nabla P}{P} \frac{2T}{\nabla T} \quad . \tag{3.9}$$

If ∇P is of the same order as P, as is often the case, then the value of the ratio is determined by the temperature and temperature gradient. If RM is approximately unity, then,

$$\nabla T \tilde{=} T \quad . \tag{3.10}$$

As a general rule then, ∇T must be quite high before an appreciable thermal gradient effect will be noticed. The thermal creep contribution in the slip regime is even smaller (by several orders of magnitude) than the thermal contribution in the free molecule regime.

It should be noted that the flow formulae, [Equations (3.6) and (3.8)], that describe the mass fluxes in the slip and free molecule regime are not continuous at their intersection Knudsen number, [0.1]. A continuous model of gaseous flow through a capillary tube over the entire Knudsen number range, (0 to ∞), does not exist. This discontinuity was tolerated because of a desire to account for free molecule flow phenomena. However, the model of the gas-porous medium system to be presented (Section 3.4) is continuous.

3.3 Physical and Mathematical Model of the Porous Medium

The objective is to model the flow area distribution of a porous medium. Flow area is defined as the area available for flow through a representative differential thickness of the medium. This area is a distribution because the number of pores for any given pore diameter varies within a given medium and with different media.

Consider a gaseous flow about to enter a porous medium as shown in Figure 3. Clearly, the pore area distribution of the surface would be the distribution sought if the porous medium were very thin (say ten molecule diameters). In this case, the gas could be visualized as flowing through a thin orifice plate with the surface pore area distribution. In this situation, the large pores contribute significantly to the flow rate and all the pores go through the plate. This is not the case within a porous medium.

The number of pores that go entirely through a representative differential thickness of a fine pored medium in a straight line is negligible. This is verified by the opaqueness of the material both to the eye and under the microscope (Figure 1). This infers that the pore area distribution of the surface would, if used, over-predict the flow rate. This, in fact, is the case. Since the pores on the surface do not proceed through the medium in a straight line there must be something immediately behind the surface. It is hypothesized that another plane or orifice plate, with an identical pore area distribution to that of surface, lies at random behind the surface. Figure 4 shows two such planes stacked one behind the other. There are two observations that

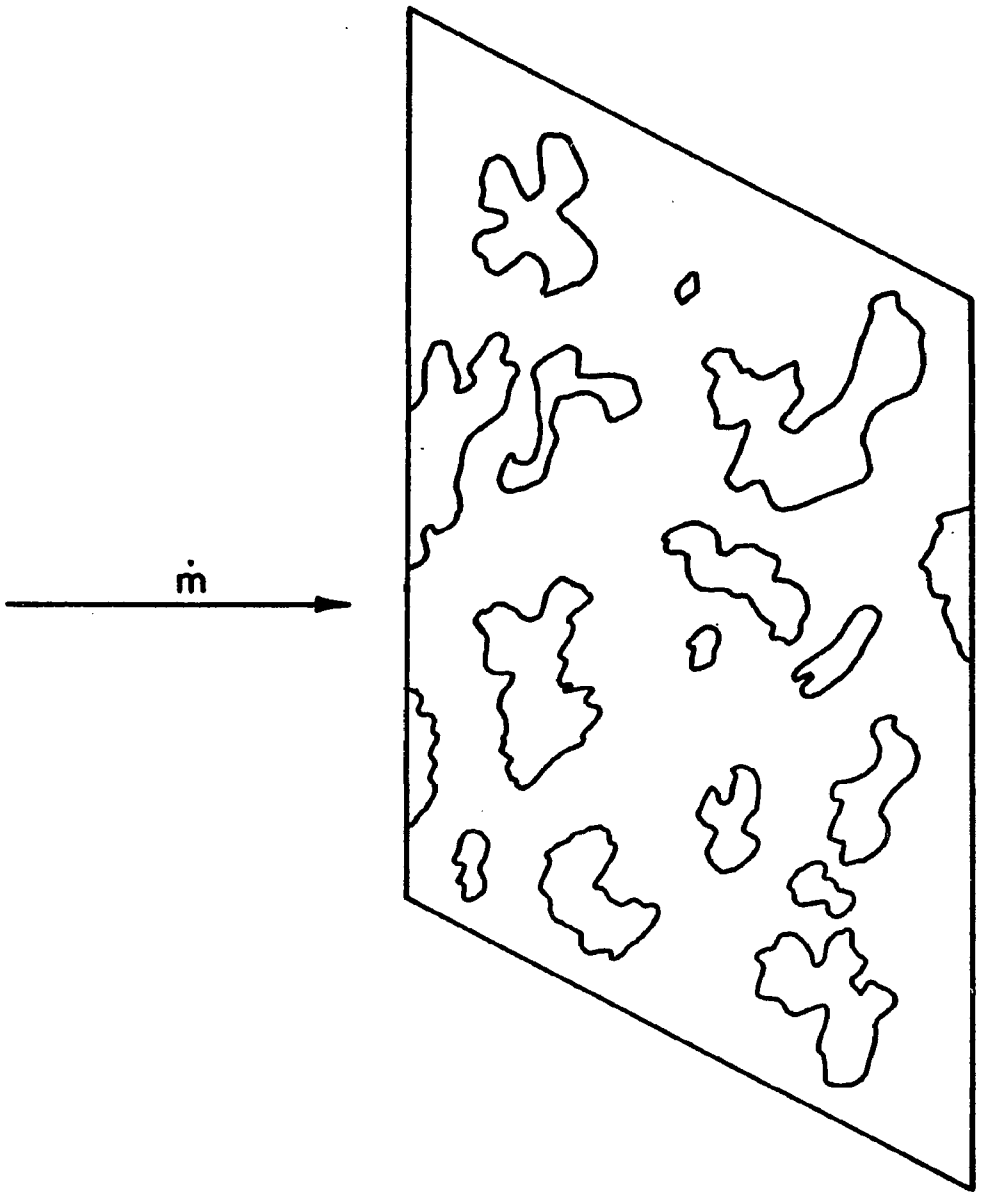

Figure 3 - Polished Porous Medium Surface

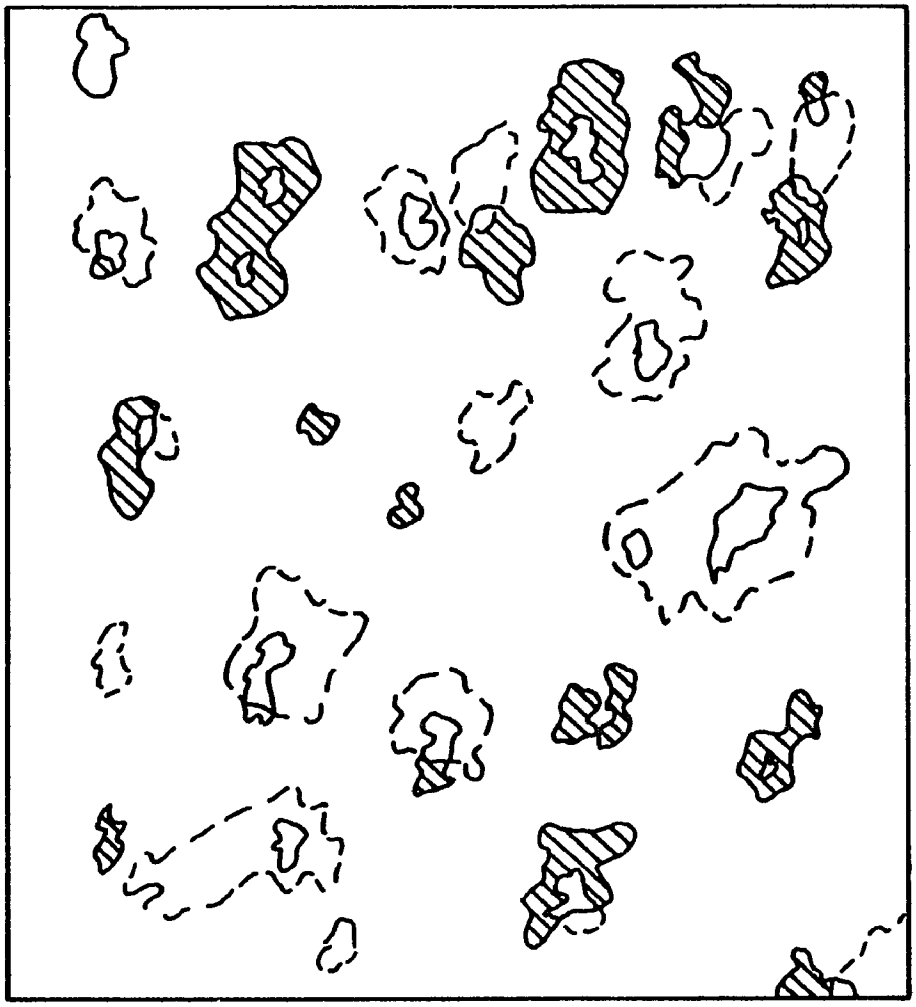

Figure 4 - Stacked Planes of Pores

should be made: the number of large holes of the two stacked planes has decreased over the single plane value and that a gas molecule traveling through the planes is allowed some lateral movement due to different pore sizes being stacked one behind the other. The first observation is true because the likelihood of a small hole falling in front of (or behind) a large one is considerably higher than two large pores falling together (in a fine pored medium there are many small pores and few large ones). The second observation is true because the medium is assumed to be homogeneous; that is, the lateral and axial pore structures are identical. It is conceivable that a third or fourth stacked plate would completely eliminate the straight paths through the plates, forcing all the gas molecules to travel laterally as well as axially. This, of course, makes the stacked plates opaque to the eye in the same fashion that a fine pored medium is. Another consequence of stacking additional plates is to further reduce the significance of the large diameter pores; making them unimportant as far as axial flow is concerned. The physical model of the porous medium, then, is a grouping of very thin (ten times the gas molecular diameter) orifice plates one behind the other in a random fashion.

There are several characteristics of this physical model that should be noted. The most important of these characteristics is that the flow resistance increases as the number of stacked planes increases. This is due to the fact that the larger the number of planes the more likely that the small pores will control the flow. A second important feature is the concept of very thin plates. These are thick enough to

allow lateral movement of the gas but are thin enough so that they do not interfer with the lower bound of the physical (as opposed to mathematical) differential thickness. This means that the number of planes needed to represent the required resistance is independent of the minimum physical differential thickness of the medium. This will be borne out later (Figure 53) where it will be seen that the smaller the median pore diameter, the larger the number of stacked planes; yet, the minimum physical differential thickness increases with median pore diameter. This effect is illustrated in Figure 5.

The mathematical model of the medium is conceptually based on the above physical model and the following assumptions:

1. The probability of a gas molecule, about to enter the medium, and finding a pore of radius a or larger is given by the cumulative pore area distribution of the surface, $\phi_o(a)$.
2. A pore at the entrance to an incremental thickness is connected to the exit by some path.
3. The probability that a gas molecule will remain in a pore of radius a or larger as it travels through the N orifice plates is given by the normalized cumulative pore area distribution, $\phi_o(a)/\phi_m$, raised to the power N. Hereafter N will be referred to as the probability exponent.

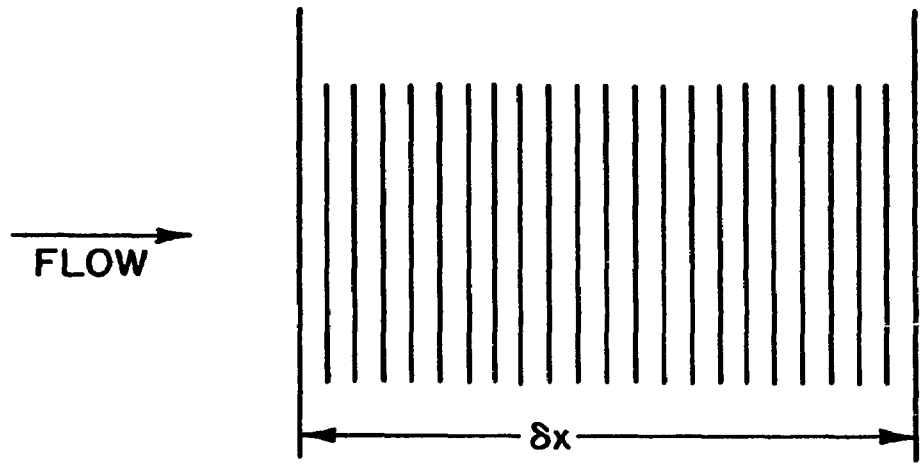

$\delta x_{min} = 40\mu$, $N = 22$, $a_m = 0.4\mu$

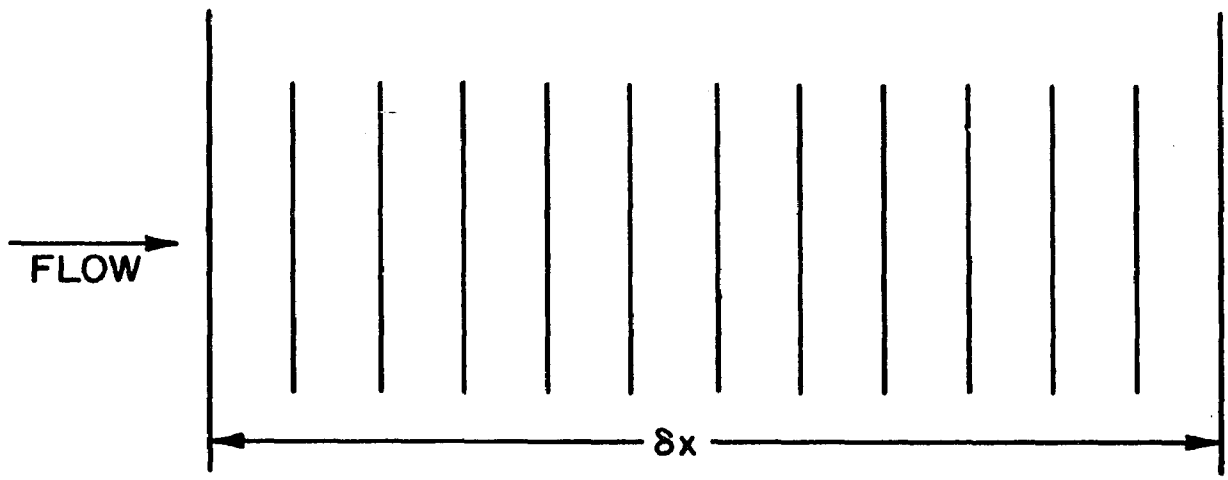

$\delta x_{min} = 1000\mu$, $N = 12$, $a_m = 10.0\mu$

Figure 5 - Independence of N and dx

A representative flow area distribution is then given by:

$$\phi(a) \equiv \phi_o(a) \left(\frac{\phi_o(a)}{\phi_m} \right)^N \tag{3.11}$$

where $\phi(a)$ is the effective cumulative pore area distribution. $\phi(a)$ is assumed to represent the flow area distribution for a representative imcremental thickness of the porous medium. The relationship between $\phi(a)$ and $\phi_o(a)$ is shown in Figure 6. It should be noted that the total area available for flow remains constant (because of the lateral flow paths) but that the average pore diameter of the medium decreases with increasing N.

Thus the porous medium can be modeled if the cumulative pore area distribution of the surface and the number of planes required to model the medium, can be experimentally determined.

3.3.1 Determination of a Specific Cumulative Pore Area Distribution for a Porous Medium. There are two ways of collecting experimental data related to the pore area distribution: a technique utilizing the mercury porosimeter and a technique utilizing the Scanning Electron Microscope. The procedures of determining the cumulative specific pore area distribution for a single plane, $\phi_o(a)$, from the data of each of the above techniques, are quite different.

In the reduction of the mercury porosimeter data, the pore radius in microns is determined from the pressure by:

$$a = \frac{88.4}{P} \quad , \tag{3.12}$$

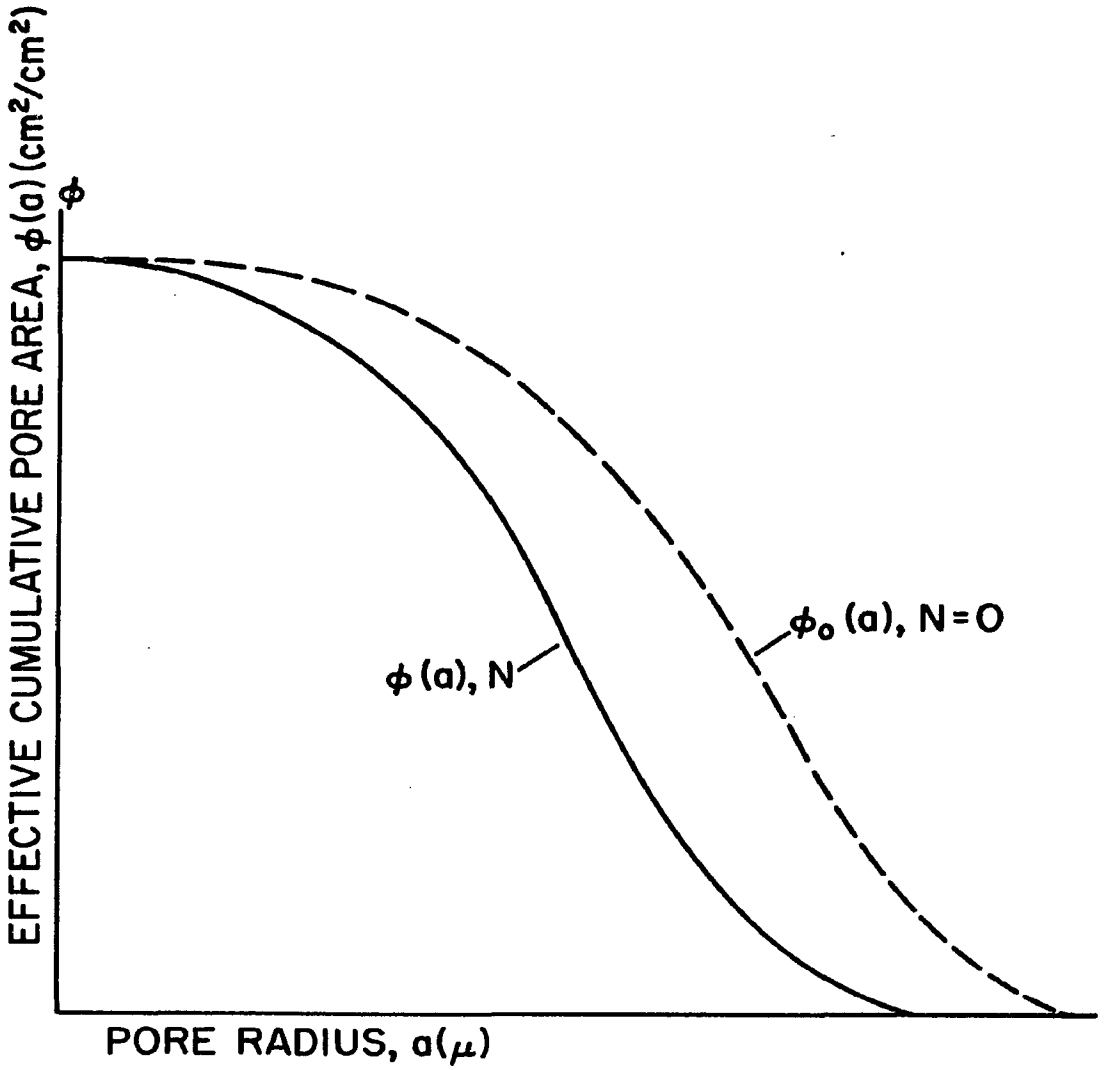

Figure 6 - Effect of Stacking Planes on the Cumulative Area Distribution

where P is the mercury insertion absolute pressure in pounds force per square inch. The specific cumulative pore area, $\phi_o(a)$ is determined from the porosity, $\varepsilon(a)$ and the porous medium density, ρ_m, by:

$$\phi_o(a) = K_p \, (\varepsilon(a) \cdot \rho_m)^{2/3} \quad , \tag{3.13}$$

where

$$K_p = \pi \left(\frac{3}{4\pi} \right)^{2/3} \tilde{=} 1.21 \tag{3.14}$$

if the pores are assumed to be "spherical". The above relationships [Equations (3.12) and (3.13)] are based upon the reasoning that the average pore cross-sectional area is proportional to the pore volume raised to the two-thirds power. The cumulative distribution curve, $\phi_o(a)$, is similar in shape to the original porosity curve, $\varepsilon(P)$, as is shown qualitatively in Figures 7a and b.

The Scanning Electron Microscope technique provides the data required to calculate $\phi_o(a)$ and the pore radius, a, from their definitions. Thus, the radius,

$$a = \frac{2A_p}{P_p} \quad , \tag{3.15}$$

where A_p is the area of the pore and P_p is the perimeter of the pore. The specific cumulative pore area,

$$\phi_o(a) = \sum_{I_a} f(I_a) \circ A_p(I_a) \quad , \tag{3.16}$$

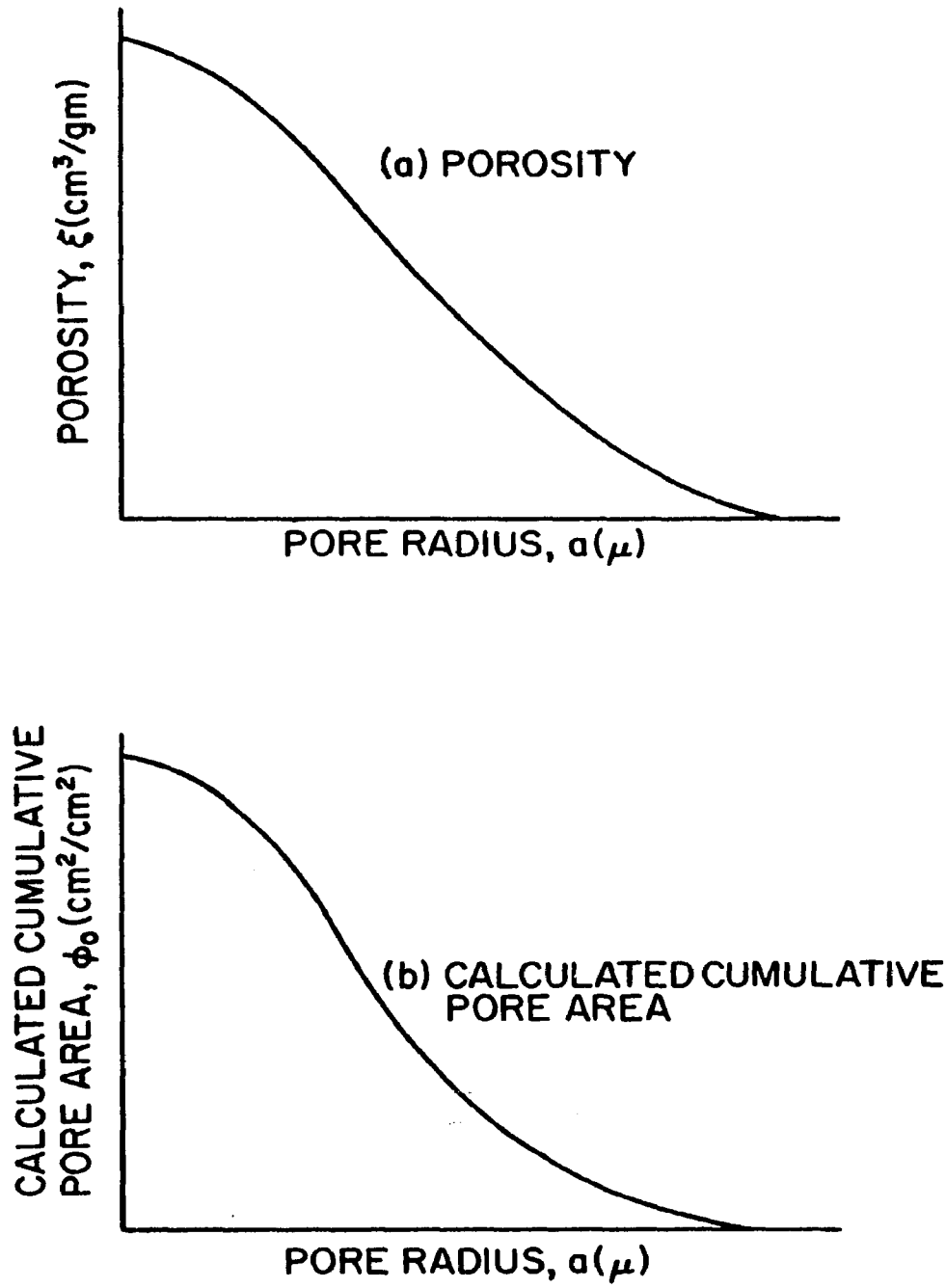

Figure 7 - Relation of ϕ_o to ε

where I_a represents a class interval of radii (i.e., a range of radii), and $f(I_a)$ the number of pores of area $A_p(I_a)$ in the class interval I_a per unit surface area. This results in a functional form for $\phi_o(a)$ that is typified by Figure 7b.

3.4 The model of the Gas-Porous Medium System

The model of the gas-porous medium system is based upon the following physical assumptions:

1. Only one flow regime is encountered within a given pore and differential thickness.
2. The entrance pore diameter and gas state control the flow regime for any differential thickness.
3. The portion of the flow falling in a particular regime can vary from one differential thickness to the following one.
4. There are multiple parallel flow paths (different parallel pores), which allow the three flow regimes to occur in parallel within a given differential thickness.
5. The pressure and temperature are uniform at the inlet and outlet of each differential thickness.

It is further assumed that a representative incremental thickness can be found and that the cumulative pore area distribution is known. Equations (3.1), (3.6), and (3.8) are assumed to model the mass flux per unit cross-sectional area of pore. The product of one of the

differential equations [Equations (3.1), (3.6), and (3.8)] and $d\phi$ governs the mass flux (per unit cross-sectional area of porous medium surface) over a range of radii, da, about the radius, a, for that flow regime. The mass flux (per unit porous medium surface area) in any flow regime is then given by the integral of its differential equation over the area contribution, $\Delta\phi$, for that regime. The total mass flux for the porous medium is the sum of each of these contributions and is given by:

$$\dot{m} = \int_0^{\phi_1} \dot{m}_c \, d\phi + \int_{\phi_1}^{\phi_2} \dot{m}_s \, d\phi + \int_{\phi_2}^{\phi_3} \dot{m}_f \, d\phi \quad , \tag{3.17}$$

where the limits on the integrals are determined by the state at a particular location [i.e., P(x), T(x)] and the cut-off Knudsen number. The value of the cut-off Knudsen number was chosen as 10. The cut-off criterion

$$KN > KN_c, \quad \text{continuum regime} \tag{3.18}$$

$$0.01\ KN_c \leq KN \leq KN_c, \quad \text{slip regime} \tag{3.19}$$

$$KN < 0.01\ KN_c, \quad \text{free molecule regime} \tag{3.20}$$

are somewhat arbitrary, but do represent generally accepted cut-off points (40). These criteria determine the radii at which the limits of the integrals are evaluated, giving:

$$\phi_1(a) = \phi_1(5\lambda) \tag{3.21}$$

and

$$\phi_2(a) = \phi_2\ (0.05\lambda) \quad . \tag{3.22}$$

$\phi_o(a)$ and $\phi_3(a)$ are determined, respectively, by the upper and lower values of the radius experimentally encountered in the pore size determination as shown in Figure 8. $\phi_o(a)$ is always zero because of the manner in which the cumulative area distribution is determined, either with the mercury porosimeter or the Scanning Electron Microscope.

By substituting Equations (3.1), (3.4), (3.6) and (3.8) into Equation (3.17) the total mass flux,

$$\dot{m} = \int_0^{\phi_1} -\frac{\rho a^2}{8\eta}\frac{dP}{dx}\,d\phi + \int_{\phi_1}^{\phi_2} -\frac{\rho a^2}{8\eta}\left(1 + \frac{4\xi}{a}\right)\frac{dP}{dx} + \int_{\phi_1}^{\phi_2} \frac{3}{4}\frac{\eta}{T}\frac{dT}{dx}\,d\phi$$

$$+ \int_{\phi_2}^{\phi_3} -\frac{16}{3}\frac{a\sqrt{T}}{\bar{v}}\frac{d\left|P/\sqrt{T}\right|}{dx}\,d\phi \quad . \tag{3.23}$$

where it has been assumed that the flow is one-dimensional.

3.5 Non-Dimensionalization

The continuum mass flow was chosen as the normalizing mass flux because, as a general rule, most of the flow falls into the continuum regime.

The continuum mass flux is

$$\dot{m}_c = -\frac{\rho}{8\eta}\frac{dP}{dx}\int_0^{\phi_1} a^2\,d\phi \tag{3.24}$$

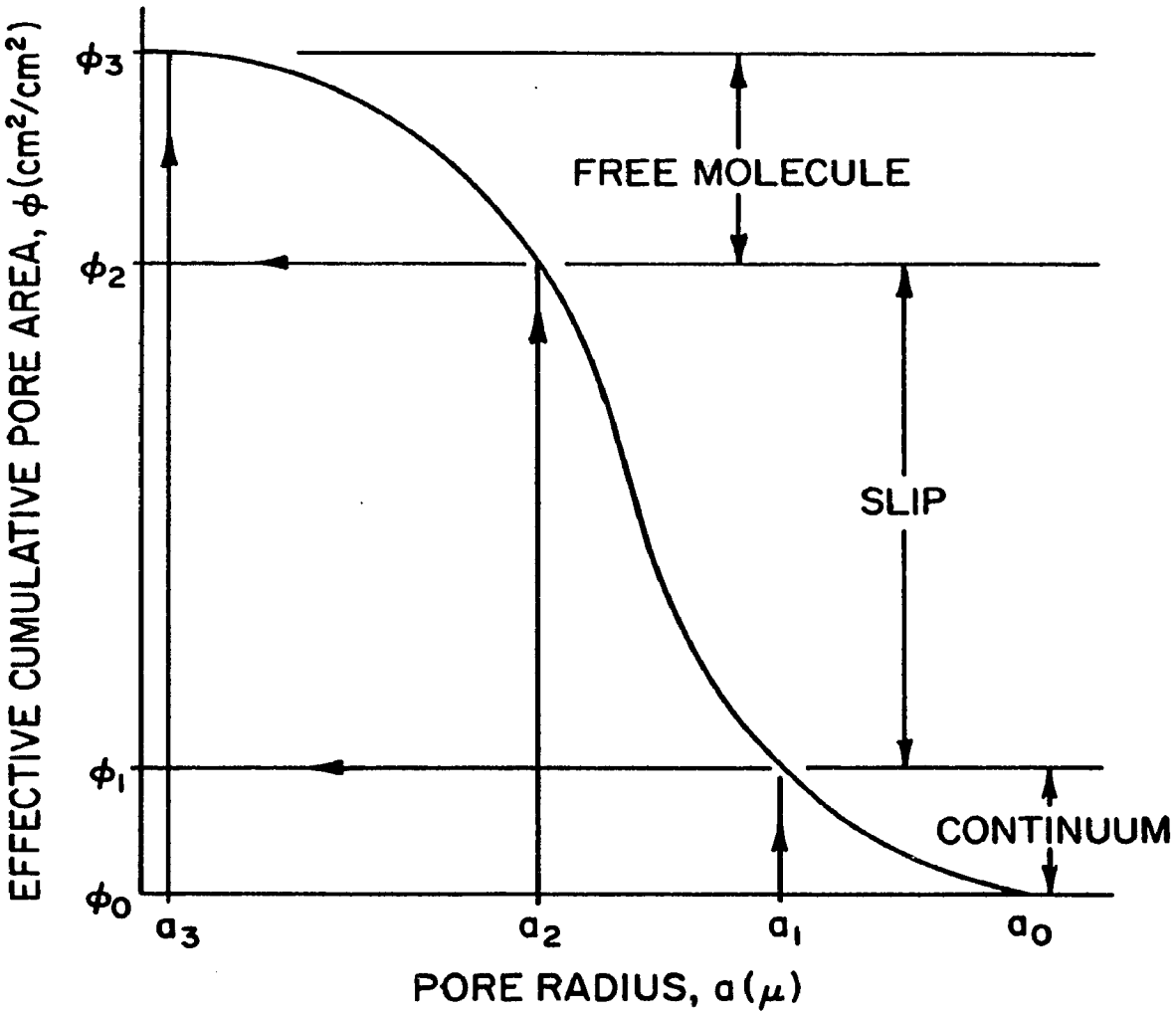

Figure 8 - Area Distribution Limits of the Mass Flux Integrals

and can be maximized by maximizing ρ, $\frac{dP}{dx}$ and $\int_0^{\phi_1} a^2\, d\phi$, and minimizing η. If P_H and T_L are, respectively, the high pressure and low temperature, then the maximum density is

$$\rho_H = P_H/RT_L \quad , \tag{3.25}$$

and the maximum pressure gradient is

$$\left.\frac{dP}{dx}\right|_{max} = P_H/L \quad , \tag{3.25}$$

where L is the thickness of the sample and the exit pressure has been assumed to be zero. The minimum value of viscosity, η, is

$$\eta_L = \eta_r \left(\frac{T_r + J}{T_L + J}\right) \left(\frac{T_L}{T_r}\right)^{3/2} \quad , \tag{3.27}$$

where T_r and J are constants. It is much more difficult to find a maximum value of $\int_0^{\phi_1} a^2\, d\phi$; however, an approximation can be found.

Since a is a monotonic function of ϕ,

$$\int_0^{\phi_x} a^2\, d\phi > \int_0^{\phi_1} a^2\, d\phi \quad \text{if and only if } \phi_x > \phi_1 \quad . \tag{3.28}$$

Thus, an upper-bound to the $\int_0^{\phi_x} a^2\, d\phi$ could be found if the functional relationship between a and ϕ were known. An approximation to this function is that the logarithm of a is linearly dependent upon ϕ, as shown by the dashed line in Figure 9. Using this assumption the radius, a, can be shown to be:

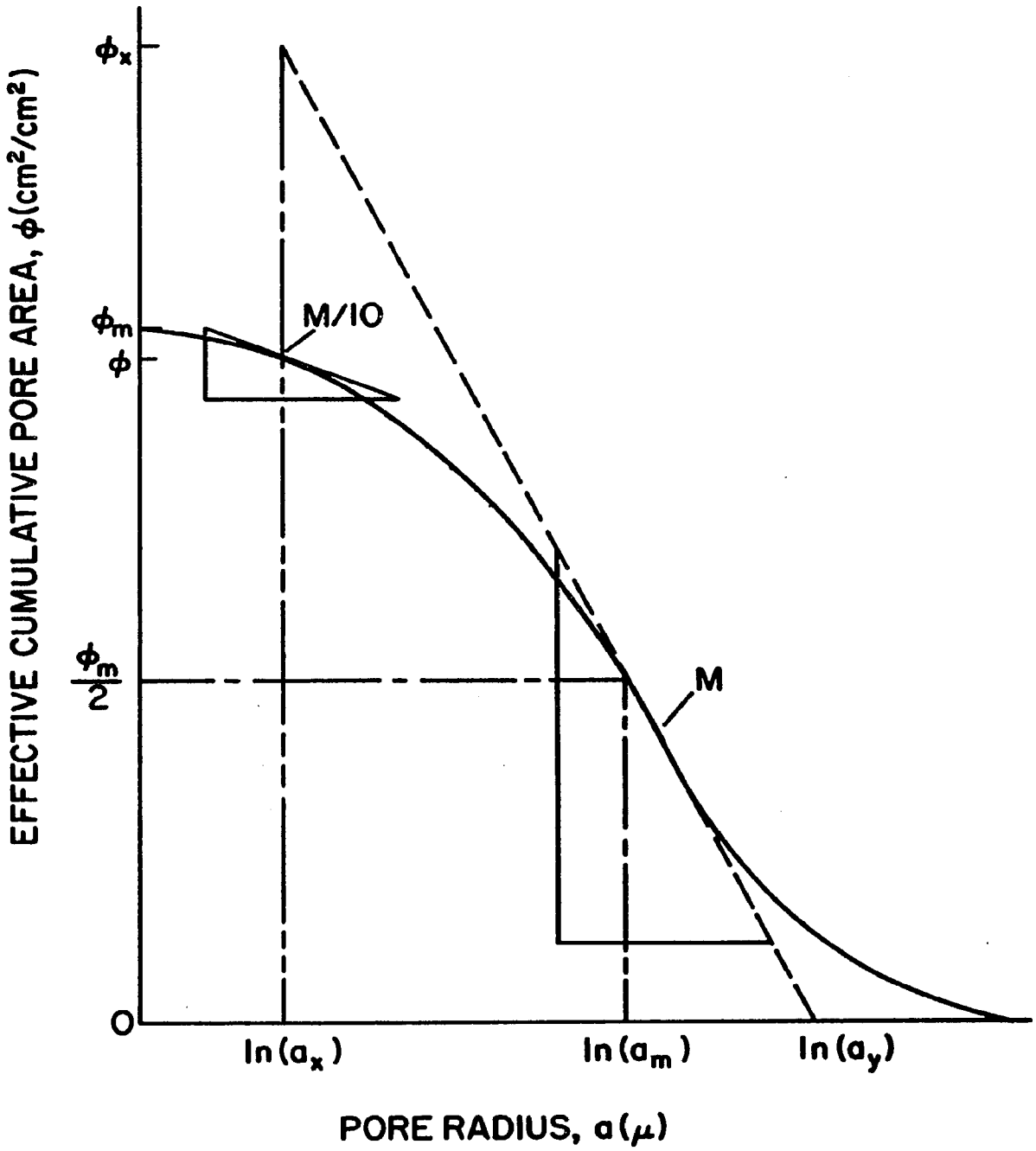

Figure 9 - Determination of a_x, a_y and ϕ_x

$$a = a_y \, e^{\phi/M} \quad , \tag{3.29}$$

where

$$M = \phi_x / \ln \left(\frac{a_x}{a_y}\right) \quad , \tag{3.30}$$

where a_x and a_y are, respectively, the smallest and largest pore radii considered. The left-hand side of the inequality [Equation (3.28)] is:

$$\int_0^{\phi_x} a^2 d\phi \simeq \frac{a_y^2 \, \phi_x}{2 \ln(a_y/a_x)} \quad , \tag{3.31}$$

where it has been assumed that the ratio $(a_x/a_y)^2$ is much smaller than unity since (a_x/a_y) is usually less than a tenth. A dimensionless resistance parameter, B, can now be formed using the maximum value of the cumulative area, ϕ_m, and the median pore radius a_m. The dimensionless resistance parameter, B, is defined as:

$$B \equiv \frac{2 \ln (a_x/a_y)}{\left(\frac{a_y}{a_m}\right)^2 \left(\frac{\phi_x}{\phi_m}\right)} \quad . \tag{3.32}$$

The normalized mass flux is then based on a_m^2 and ϕ_m.

One procedure for determining ϕ_x and a_x is to define the point where the slope of the ϕ versus ln(a) curve is ten percent of the maximum slope, as having the coordinates, ϕ_m and $\ln(a_x)$. The intersection of the maximum slope line with $\ln(a_x)$ would define the value of ϕx. These choices are shown in Figure 9 and were made for two reasons.

The maximum frequency, f_m, Figure 10, is proportional to the maximum slope of the ϕ versus ln(a) curve and this, in turn, is completely specified by ϕ_x, a_x, and a_y. Secondly, the product of the median diameter squared and ϕ_m represents a characteristic flow area of the porous medium.

The non-dimensional variables can now be defined:

$$P^* \equiv P/P_H \quad , \tag{3.33}$$

$$T^* \equiv T/T_L \quad , \tag{3.34}$$

$$a^* \equiv a/a_m \quad , \tag{3.35}$$

$$x^* \equiv x/L \quad , \tag{3.36}$$

$$\eta \equiv \eta/\eta(T_L) \quad , \tag{3.37}$$

$$\rho \equiv \rho/\rho(P_H, T_L) \quad , \tag{3.38}$$

$$\phi \equiv \phi/\phi_m \tag{3.39}$$

$$\dot{m}^* \equiv \dot{m} \Big/ \left\{ \frac{\rho_H}{8\eta_L} \cdot \frac{\phi_m a_m^2}{B} \frac{P_H}{L} \right\} \quad . \tag{3.40}$$

Substituting Equations (3.32) through (3.40) into Equation (3.23) yields an expression for the non-dimensional mass flux in terms of the non-dimensional variables,

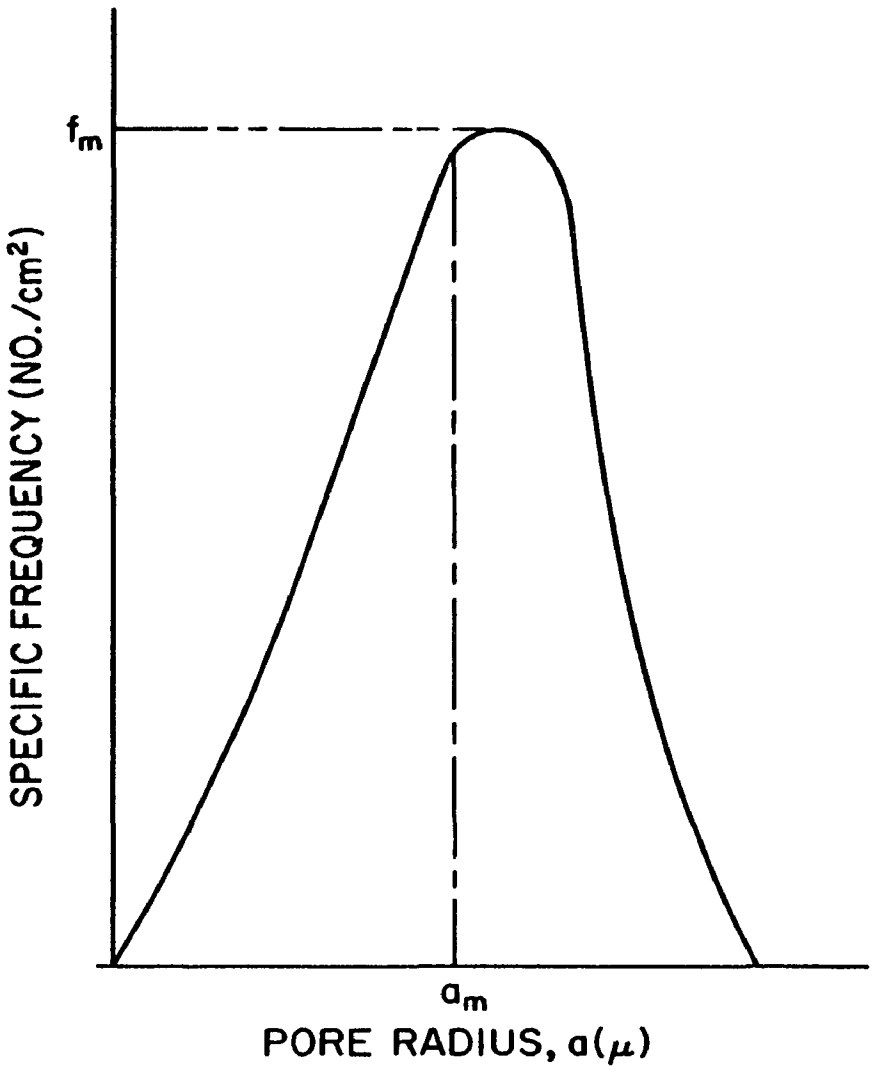

Figure 10 - Frequency Distribution of Pore Diameters

$$\dot{m}^* = B\left[- \frac{\rho^*}{\eta^*} \frac{dP^*}{dx^*} \left\{ \int_0^{\phi_1^*} a^{*2}\, d\phi + \int_{\phi^*_1}^{\phi_2^*} a^{*2} \left(1 + \frac{8}{KNa^*}\right) d\phi^* \right\} + \frac{48(\phi_2^* - \phi_1^*)}{\pi\, KN_r^2} \frac{\eta^*}{T^*} \frac{dT^*}{dx^*} - \frac{64}{3KN_r} \frac{dP^*/\sqrt{T^*}}{dx^*} \int_{\phi_2^*}^{\phi_3^*} a^*\, d\phi^* \right], \tag{3.41}$$

where

$$KN = 2a_m/\lambda(P^*, T^*) \tag{3.42}$$

and

$$KN_r = 2a_m/\lambda(P_H, T_L) \quad . \tag{3.43}$$

Note that the medium property, "B", acts as the proportionality constant between the driving forces $\frac{dP^*}{dx^*}$, $\frac{dT^*}{dx^*}$ and the mass flux. The Knudsen numbers, KN and KN_r control the contribution of slip, thermal creep and free molecular flow. Large values of the Knudsen numbers (> 10) indicate that the limits, ϕ_1^*, ϕ_2^*, and ϕ_3^* are very close to each other, thereby forcing to zero the integrals with any two of these variables as limits. Conversely, if the Knudsen numbers are small (< 0.1), then the free molecular, thermal creep, and slip portions of the flow become dominant. This means that free molecule flow is not normally encountered because the mean free path of the gas is usually much smaller than the pore radius. At standard conditions, the mean free path of nitrogen is approximately 0.06μ; as a result, a porous medium would have to have a median pore diameter of approximately 0.006μ to support mostly free molecular flow at these standard conditions.

3.6 Solution Technique and Assumptions

Since the pressure is not known, a priori, as a function of the position it is not possible to calculate the mass flux, $\dot{m}^*$, directly. Instead, one must view Equation (3.41) as a non-linear first order ordinary differential equation with the pressure as the dependent variable.

It is assumed that mass flow of the gas through the medium does not affect the steady state temperature distribution and that the gas adopts the local temperature of the porous medium. With these and other minor assumptions, the solution to the energy equation describing the temperature characteristics of the porous medium sample can be obtained and shows that:

$$\frac{T - T_o}{T_1 - T_o} = x/L \tag{3.44}$$

and that

$$\frac{dT}{dx} = \frac{T_1 - T_o}{L} \quad . \tag{3.45}$$

Now, if a value of the mass flux, $\dot{m}^*$, is chosen, Equation (3.41) becomes a nonlinear first order differential equation in the pressure, where the only unknown is the pressure as a function of the displacement. It can then be shown that

$$\frac{dP^*}{dx^*} = \frac{\left[\frac{dT^*}{dx^*}\frac{48}{\pi KN_r^{\,2}}\frac{\eta^*}{T^*}(\phi_2^* - \phi_1^*) + \frac{32}{T^{*3/2}}\int_{\phi_2^*}^{\phi_3^*} a^*\, d\phi^*\right] - \frac{\dot{m}^*}{B}}{\frac{\rho^*}{\eta^*}\left[\int_0^{\phi_2^*} a^{*2}\, d\phi^* + \frac{8}{KN}\int_{\phi_1^*}^{\phi_2^*} a^*\, d\phi^* + \frac{64}{3KN_r}\frac{1}{T^*}\int_{\phi_3^*}^{\phi_3^*} a^*\, d\phi^*\right]} \quad . \tag{3.46}$$

Equation (3.46) is non-linear because both KN and the limits of the integrals, ϕ_1^*, ϕ_2^* are functions of the pressure, P*. The solution of this equation requires that one know T*(x*) and $\frac{\dot{m}^*}{B}$ and yields a functional relationship:

$$P^* = P^*(x^*, T^*, KN_r, \frac{\dot{m}^*}{B}) \quad . \tag{3.47}$$

Equation (3.46) was solved by using Hammings predictor-corrector method with a Runga-Kutta start-up routine. The program utilized was written by I.B.M., is named DHPCG, and is part of I.B.M.'s Scientific Subroutine Package. The solutions obtained are presented in Chapter V.

3.7 Characteristics of the Differential Equation in the Limits of Continuum and Free Molecular Flow

In the continuum flow regime, the governing differential equation reduces to a first order non-linear equation, that is:

$$\frac{dP^*}{dx^*} = - \frac{\frac{\dot{m}^*}{B}}{\frac{\rho^*}{\eta^*} \int_0^{\phi_3^*} a^{*2} \, d\phi^*} \quad . \tag{3.48}$$

This equation can be solved if one assumes that

$$\eta^* = T^{*3/2} \tag{3.49}$$

and

$$T^* = T_0^* - (T_0^* - T_1^*)x^* \quad . \tag{3.50}$$

Equation (3.48) when solved for the pressure yields

$$P^* = \left\{ 1 - \left[\frac{\dot{m}^*}{B \int_0^{\phi_3^*} a^{*2}\, d\phi^*} \right] - \left[\frac{4}{7(T_0^* - T_1^*)} \right] \left[(T_0^* - (T_0^* - T_1^*)x^*)^{7/2} - T_0^{*7/2} \right] \right\}^{1/2} ,$$

$$T_0^* > T_1^* \ , \ T_1^* = 1 \quad . \tag{3.51}$$

In the free molecular regime, the governing differential equation takes the form,

$$\frac{dP^*}{dx^*} = T^{*1/2} \left[\frac{\dot{m}^*}{A^*} - \frac{P^*}{2T^{*3/2}} \frac{dT^*}{dx^*} \right] , \tag{3.52}$$

with

$$A^* = \frac{64B}{KN_r} \int_0^{\phi_3^*} a^*\, d\phi^* , \tag{3.53}$$

and a solution,

$$P^* = \left(1 - \left(\frac{T_0^* - T_1^*}{T_0^*} \right) x^* \right)^{1/2} - \frac{\dot{m}^*}{A^*} \frac{(T_0^* - (T_0^* - T_1^*)x^*)^{3/2}}{T_0^* - T_1^*} ,$$

$$\text{for } T_0^* \neq T_1^* \quad . \tag{3.54}$$

Note that if $\dot{m}^*$ is zero, then Equation (3.54) gives the Knudsen relationship for the pressures:

$$P^* = \left(\frac{T_1^*}{T_0^*} \right)^{1/2} \quad . \tag{3.55}$$

3.8 Summary of Gas-Porous Medium Model

An analytical model of the gas-porous medium interaction under non-isothermal conditions has been presented. The porous medium and gaseous flow phenomena have been modeled independently and then combined to form a model of the gas-porous medium interaction. The resulting non-linear differential equation describes the pressure as a function of the position into the medium, the mass flux of the gas, temperature gradient, and medium properties.

The differential equation was non-dimensionalized, yielding two parameters: a medium resistance parameter and a characteristic Knudsen number.

CHAPTER IV

EXPERIMENTAL APPARATUS AND PROCEDURES

4.1 Objective of the Experimental Study

The experimental objective was to collect the data needed to correlate the results of the analytical study with physical fact. The probe consisted of two distinct portions: determination of the flow properties of a gas in different media under non-isothermal conditions and the determination of the pore size distributions of the media used.

4.2 Porous Media Sample Construction, Mounting and Leakage Tests

Four different porous media were considered in this study. Three of the porous media were purchased from Pure Carbon Company of Saint Marys, Pennsylvania and are denoted by the prefix "FC". A fourth carbon, Poco-Ax, was donated by the General Motors Research Laboratories of Warren, Michigan. Table I lists several property values for the different media used.

TABLE I

POROUS MEDIA SAMPLES

Type	Medium Pore Radius, μ*	Pore Volume From 88.4 to 0.00 1768μ, Radius, cc/gm**	Average Density gm/cc**
FC-01	0.2	0.124137	1.77
FC-11	6.0	0.253424	1.32
FC-25	0.8	0.101700	1.82
POCO-AX	0.9	0.620080	0.85***

(*) Provided by Micrometrics Instrument Corp., Norcross, Georgia.
(**) Provided by Pure Carbon Co., Saint Marys, Pa. except POCO.
(***) Measured by the author.

The pore volumes for each sample were determined from the same block of material from which the samples for the flow experiments and Scanning Electron Microscope were taken. The porous samples were constructed for the flow tests by machining them into circular disks, 2-3/4 inches in diameter. Three thicknesses (1/2, 1/4, 1/8 inches) of each porous sample were used resulting in a total of twelve samples. Each porous sample was radially sealed by using a ceramic ring which was cemented to the circumferential edge of the porous sample itself with epoxy cement. A detailed construction plan of the samples is shown in Figure 11. The ceramic ring radially insulated the sample creating a uniform surface temperature as well as preventing radial flow. All of the samples were leak tested for radial leaks by blocking axial flow through the porous sample at the exit and applying a three-atmosphere pressure differential across the ceramic ring as shown in Figure 12.

During these tests, the sample was sandwiched between the heater assembly, (Item 5, Figure 12), the water cooled head (Item 1, Figure 12), and two gaskets, numbered 2 and 4 in Figure 12. The gas flow rate was found to be zero up to a three-atmosphere differential for all samples. At a pressure differential of four atmospheres, a slight leak was noticed (5 cc/min). This was hypothesized to be due to the compression of the rear gasket (Item 4, Figure 12) by the applied pressure differential. This allowed a leak to occur between the sample and the front gasket, (Item 2, Figure 12). The leakage could be stopped by further tightening the screws joining the heater assembly to the water cooled head.

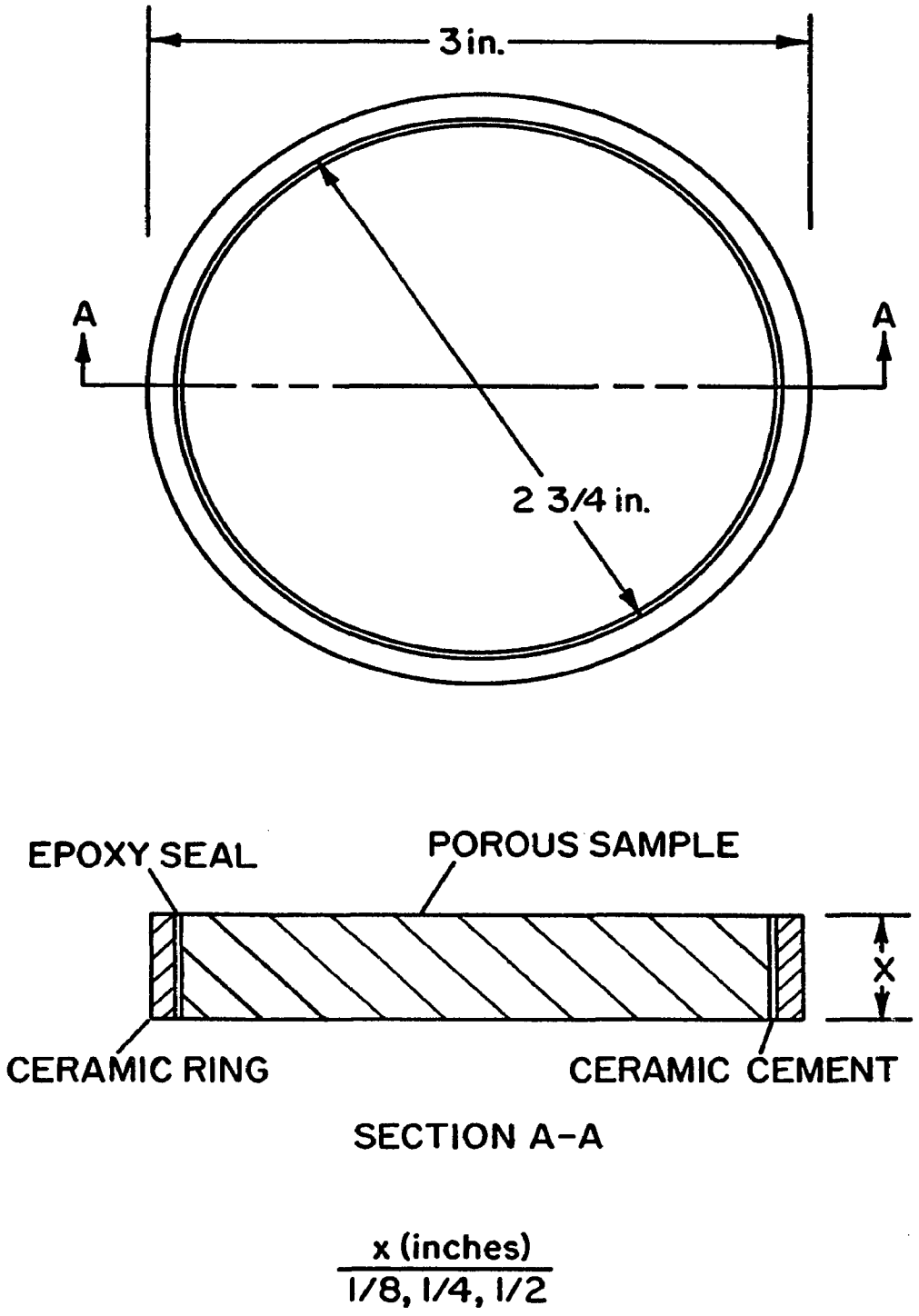

x (inches)
1/8, 1/4, 1/2

Figure 11 - Sample Construction

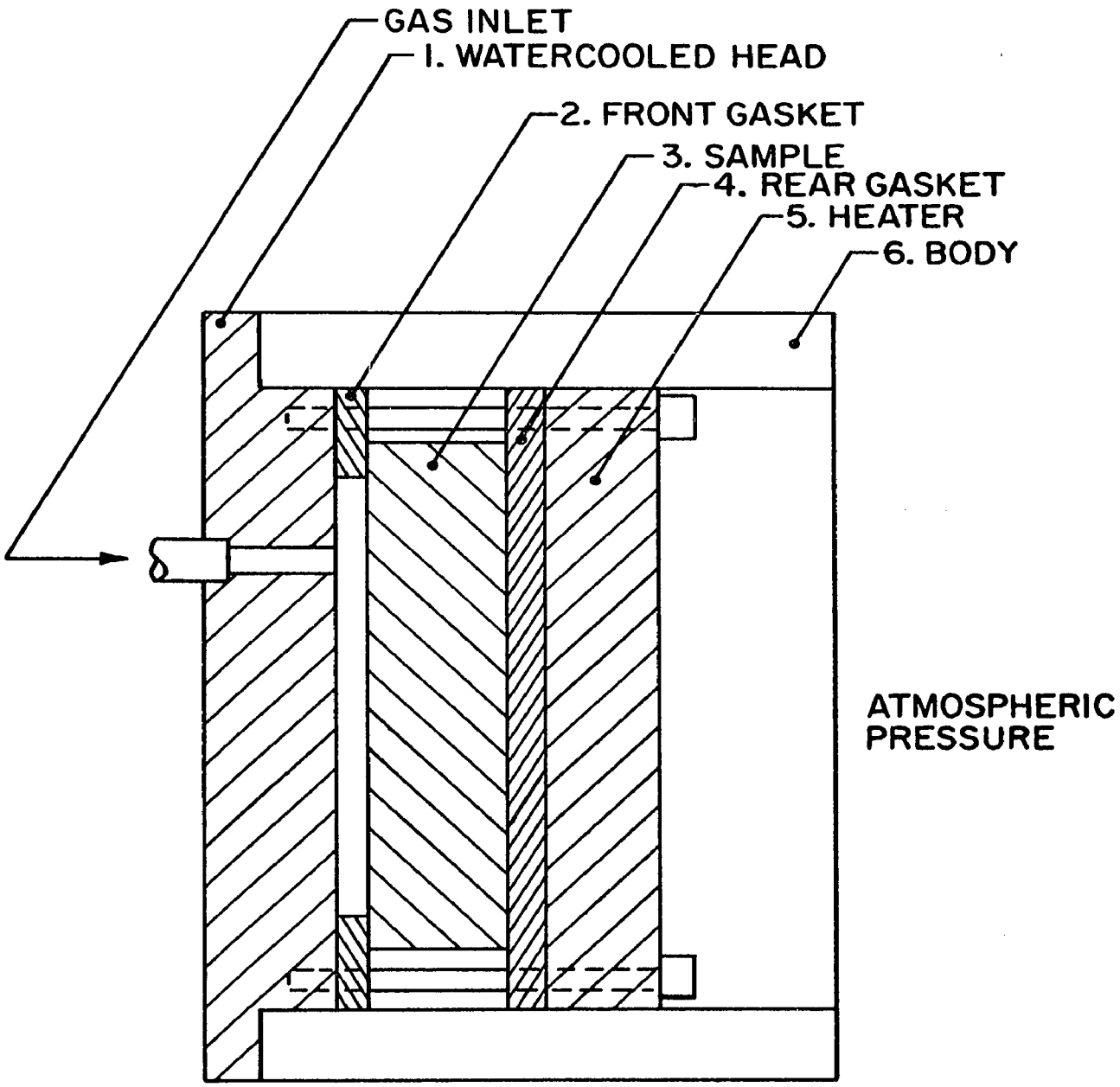

Figure 12 - Cross Section of Apparatus Used for Radial Leakage Tests

Under normal flow conditions, the apparatus is arranged as shown in Figure 12 except that the rear gasket (Item 4, Figure 12) is removed, allowing the gas to flow axially. Thus, the leakage test as performed above verifies that there is negligible radial leakage below a three atmosphere pressure differential, and the method of mounting the sample is satisfactory.

4.3 The Porous Medium Sample Holder

A sketch of the complete sample holder is shown in Figure 13. The sample itself, Item 1, Figure 13, is compressed between the water cooled head, Item 4, the Sealing gasket, Item 9, and the heater support, Item 3. The compression of the gasket is obtained by a set of screws (not shown) that run through the heater support and are attached to the water cooled head, thereby drawing the heater support and the water cooled head together. Different thicknesses of samples are accommodated by different lengths of screws. The surfaces of the sample are heated or cooled by thermal radiation from the heater and the water cooled head. The temperatures of the sample's surfaces were measured in two ways: with thermocouples and with a Barnes Radiometer, model R8-T1-C. The optical paths of the thermal radiation signal are shown as dashed lines, Items 10 Figure 13. Sodium chloride windows, Item 6, Figure 13, were used to seal against gas leakage but permitted transmission of the thermal radiation signal in the wavelength range of 0.1 to 100μ. The radial temperature gradient was measured by means of three thermocouples placed at different radial locations on the porous sample of highest

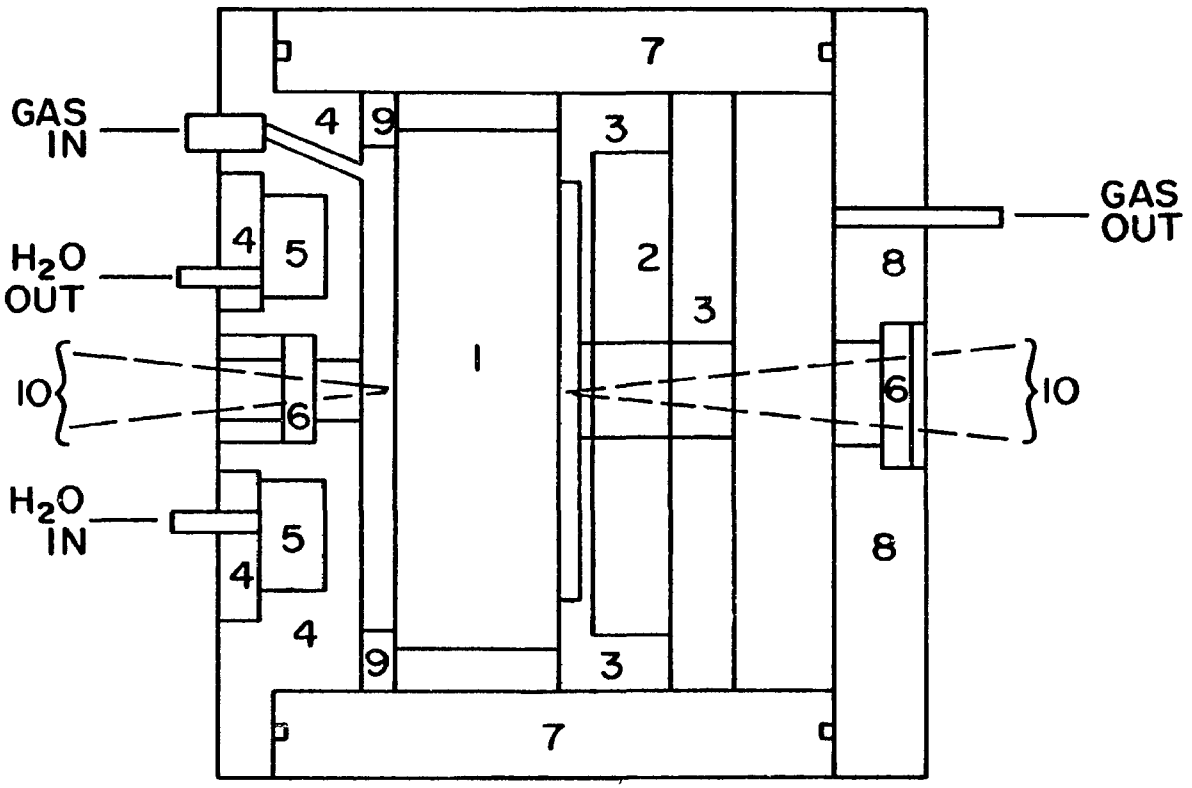

KEY

1. POROUS SAMPLE
2. HEATER
3. HEATER SUPPORT
4. WATER-COOLED HEAD
5. WATER CAVITY
6. NaCl WINDOWS
7. SAMPLE-HOLDER BODY
8. SEALING HEAD
9. GASKET
10. RADIOMETER VIEWING PATH

Figure 13 - Sample Holder Components

thermal conductivity. At the maximum surface temperature of the heater (∿550°C), the radial gradient of the sample was found to be 3°C/cm as compared with the axial gradient of 100°C/cm.

Two possible gas flow paths are available by inverting the incoming and exiting gas lines, allowing the effect of a positive and negative temperature gradient to be investigated.

4.4 Experimental Support System

A schematic diagram of the experimental support system is shown in Figure 14; a photograph of the support system is shown in Figure 15. The porous medium sample holder, Item 1, Figure 14, is shown in the center. The nitrogen gas (< 0.1% impurities) used for all of the flow experiments is stored in a high pressure tank, Item 2, Figure 14. Nitrogen flows from this storage tank through two stages of regulation, an upstream rotometer, Item 3, Figure 14, at pressure P_3 and then through an upstream throttling valve, Item 4, Figure 14, existing at pressure P_4. The gas then enters the sample holder at pressure P_4, exits at pressure P_5 and flows through a downstream throttling valve, Item 5, Figure 14, existing at pressure P_6. The nitrogen is then drawn through a choked nozzle, Item 6, Figure 14, by a vacuum pump, Item 7, and exhausted to the atmosphere.

The combination of the rotometer and choked nozzle allowed flow rates from 10 cc/min to 550 cc/min (at standard conditions) to be measured. The two throttling valves allowed the inlet pressure to the sample, P_4, and the mass flow rate to be varied independently as long as neither one of the valves was choked.

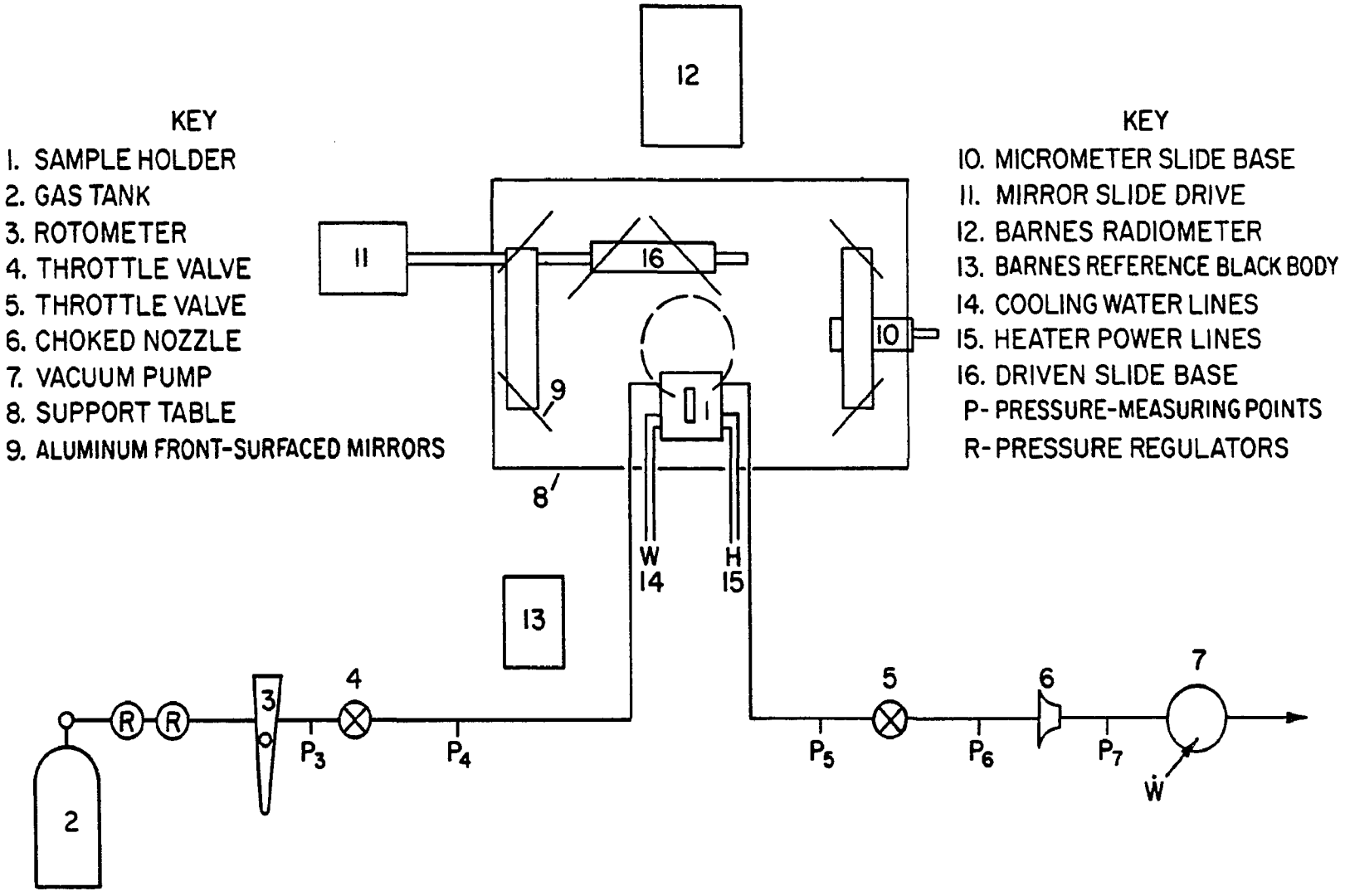

Figure 14 - Experimental Support System

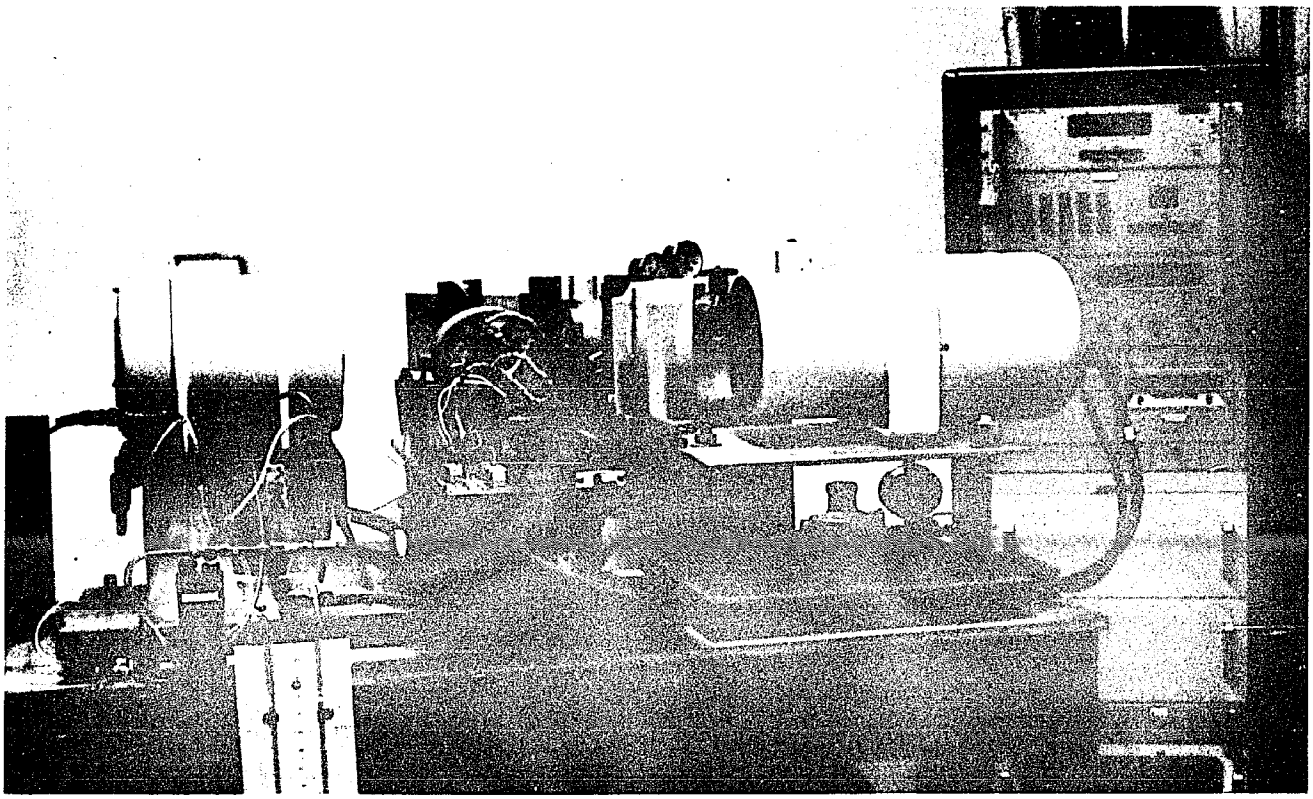

Figure 15 - Photograph of Experimental Apparatus

The support table, Item 8, Figure 14, was mounted on a ten-inch milling table so that the position of the sample holder and front surfaced aluminium mirrors, Item 9, Figure 14, could be adjusted with respect to the radiometer, Item 12, Figure 14. Each front surfaced mirror was mounted on a base which allowed it to be rotated about its vertical centerline. The mirror slide assembly, Item 16, Figure 14, in the position shown, allows the radiometer to view the heated side of the porous sample. If the slide assembly were shifted to the right, in Figure 14, then the cooled side of the porous sample would be viewed. The micrometer slide base Item 10, Figure 14, allowed the optical path of the radiometer to be kept constant when the sample thickness was changed. The blackbody reference source, Item 13, Figure 14 was used to calibrate the radiometer.

The pressure, P_3, P_4, P_6, P_7 were measured with mercury manometers. The pressure P_5 was measured directly with a mercury manometer is the pressure drop across the sample was greater than three inches of mercury. If the pressure drop across the sample was less than three inches of mercury, then the pressure differential, $P_4 - P_5$, was determined using an ethylene glycol differential manometer. Ethylene glycol was chosen because of its low vapor pressure, high sensitivity and availability.

The entire system was leak tested and found to have a leakage rate of less than 0.005 cm/min or less than 0.1% of the minimum flow rate. This was found to be reproducible after the system had been opened and reclosed. The choked nozzle and rotometer were calibrated using standard water displacement techniques. The radiometer was calibrated using the

blackbody reference source and the salt windows actually used in the experiments. In addition, its output was compared with the surface temperature of the carbon samples as determined by a thermocouple. The calibration of the radiometer and its general use is outlined in Appendix A.

All thermocouples used were calibrated at the ice point and boiling point of water and were found to lie within 1°C of the tabulated values and within 1°C of each other. The thermocouples used to measure the surface temperature of the carbon were made of 5 mil chromel-alumel thermocouple wire. The thermocouples were manufactured by the electric arc technique and were checked for continuity. The approximate time constant of such a thermocouple is one second (assuming a free convection flow field). As a result, the thermocouples were capable of following the experimental thermal transients without significant transient error. A commercial reference source, "Auto Ref" manufactured by Thermo Electronic Corporation, provided a 150°F reference temperature for the thermocouples. The output of the thermocouples and reference source was measured with a Model 2401B integrating digital voltmeter manufactured by Dymec Corporation. A Dymec channel scanning device, Model 2901A controlled by a Dymec digital clock, Model 2509A, allowed sequential scanning of up to twenty-five channels. This allowed the thermocouple and radiometer outputs to be sequentially measured by the digital voltmeter and recorded by a Dymec Model 562A, digital recorder.

4.5 Experimental Procedure of the Gaseous Flow Tests

Prior to inserting the porous sample into the sample holder it was cemented to the rubber gasket, Item 9, Figure 13, which sealed against radial flow. This insured that the sample was properly centered in the apparatus and that a good radial seal was obtained. After the apparatus was assembled, the upstream throttling valve was closed and the downstream portion of the system was evacuated to a pressure of 1 mm. Hg. Nitrogen gas was then admitted to the system at the maximum flow obtainable (always greater than 20 cc/min) for a period of eight hours. This procedure not only flushed the system's volume (6000 cc), but also allowed transient adsorption effects (if any) to occur. The above procedure was followed each time the system was opened to the atmosphere. After completing the above procedure, the isothermal flow rate was selected by adjusting the upstream throttling valve and the pressure drop was recorded. The heater was then turned on and the system allowed to reach thermal equilibrium.

The flow was then adjusted to the isothermal value, while maintaining the inlet pressure constant. After flow equilibrium had been obtained, the new outlet pressure was noted. This procedure was repeated for a second temperature gradient (heater setting) prior to changing the inlet state conditions of flow rate and pressure. The inlet pressure was then reduced by throttling the upstream flow, and a new flow rate and pressure drops were then noted for the isothermal and two non-isothermal cases. The system was then shut off and the flow

direction inverted. The above tests were then repeated at the same flow rates, inlet pressures and heater settings, and the corresponding outlet pressures noted. This procedure was followed for each of the porous samples.

Thermal equilibrium was determined by observing the radiometer output while focused on the cooled side of the apparatus. Thermal equilibrium was assumed to be reached if the output of the radiometer had changed by less than 1% (approximately 1°C) in an hour. A typical thermal transient response of a thermocouple mounted immediately beneath the surface of the sample due to a step input of 80 volts to the heater is shown in Figure 16. This indicates that thermal equilibrium of the system is obtained in approximately two hours, as the system behavior appears to be expotential.

4.6 Experimental Determination of the Pore Size Distribution by the Mercury Porosimeter Technique

The cumulative specific pore volume, cc/gm, hereafter referred to as the porosity, of each porous sample was determined commercially by Micrometrics Instrument Corporation of Norcross, Georgia. They used a Micrometrics Model 905, 0-50,000 psia, Porosimeter to determine the porosity as a function of the pore diameter. A contact angle of 130° was assumed in determining the pore radius as a function of pressure. That is, the pore radius and insertion pressure were related by the following expression:

$$a = \frac{88.4}{P} \quad . \qquad (4.1)$$

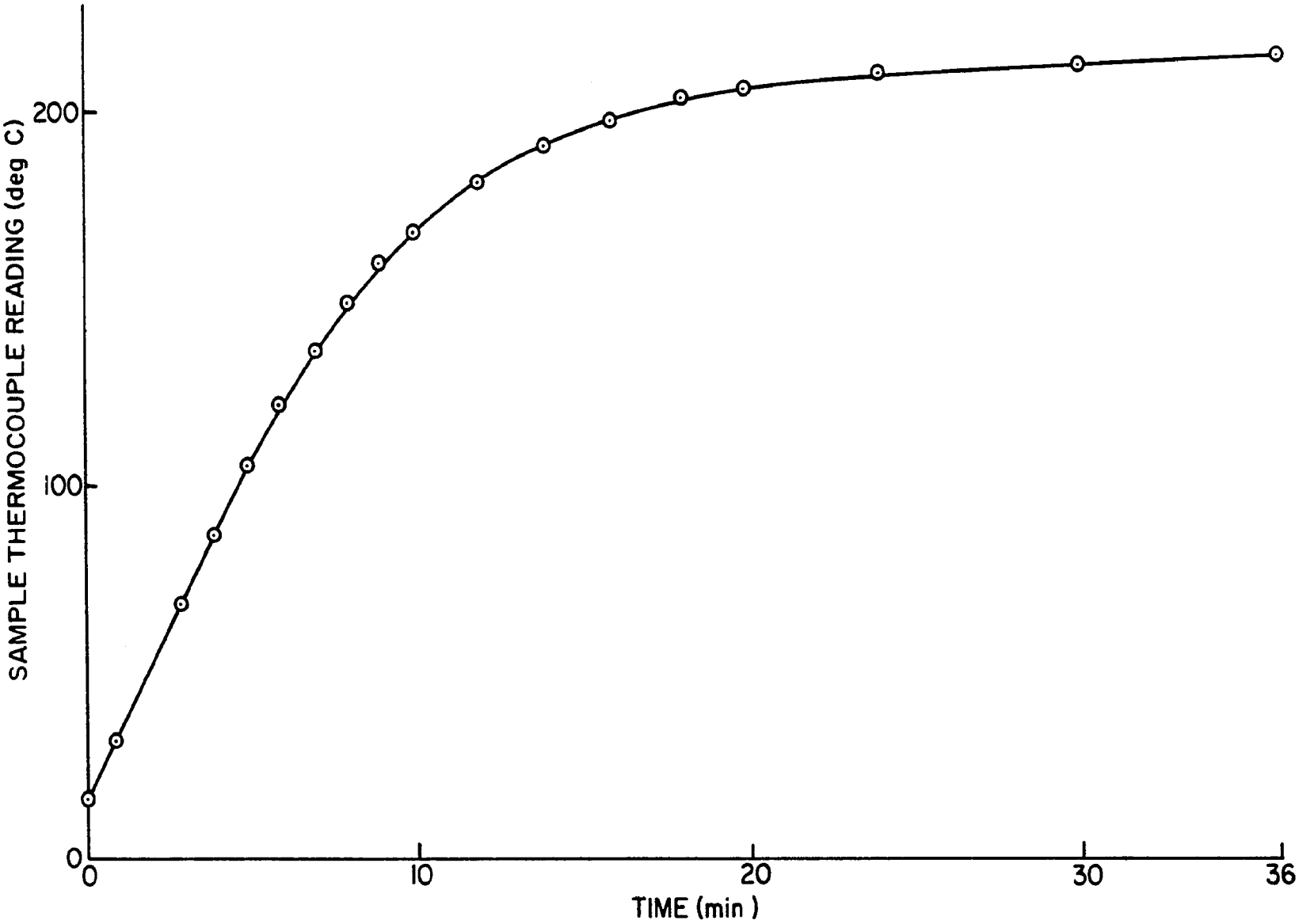

Figure 16 - Sample Surface Temperature Versus Time

The results of the porosimeter tests are shown in Figures 17 through 20. The cumulative area distribution curves for each sample were then determined from the porosity data by utilizing the relationships:

$$\phi_o(a) = (\varepsilon\rho)^{2/3} \tag{4.2}$$

and

$$\phi(a) = \phi_o(a)\left[\frac{\phi_o(a)}{\phi_m}\right]^N \quad . \tag{4.3}$$

The cumulative area distribution curves are shown in Figures 21 through 24.

4.7 Experimental Determination of the Pore Size Distribution Utilizing the Scanning Electron Microscope

The Scanning Electron Microscope (SEM) is a relatively new scientific instrument that became commercially available in the mid 1960's. Its chief attributes are that it offers a superior depth of focus over optical systems and ease of sample preparation as compared with that required by the Transmission Electron Microscope. Other attributes are that its output signal can be monitored, altered, magnetically stored and, as a result, easily processed on an electronic digital computer.

The pore size distribution of the porous sample is determined from the magnetically stored electronic signal by proper processing on the digital computer. E. W. White of the Materials Research Laboratory

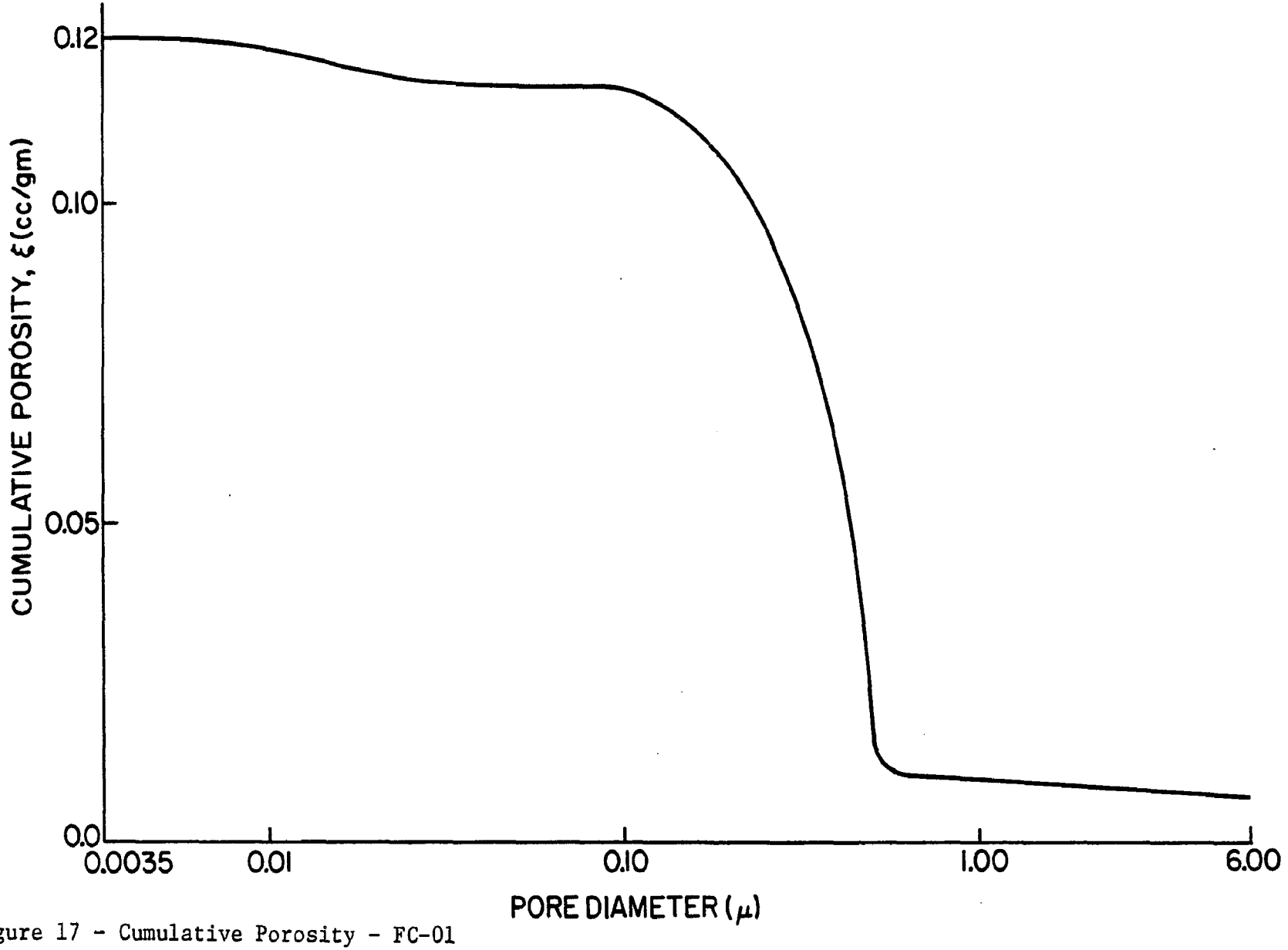

Figure 17 - Cumulative Porosity - FC-01

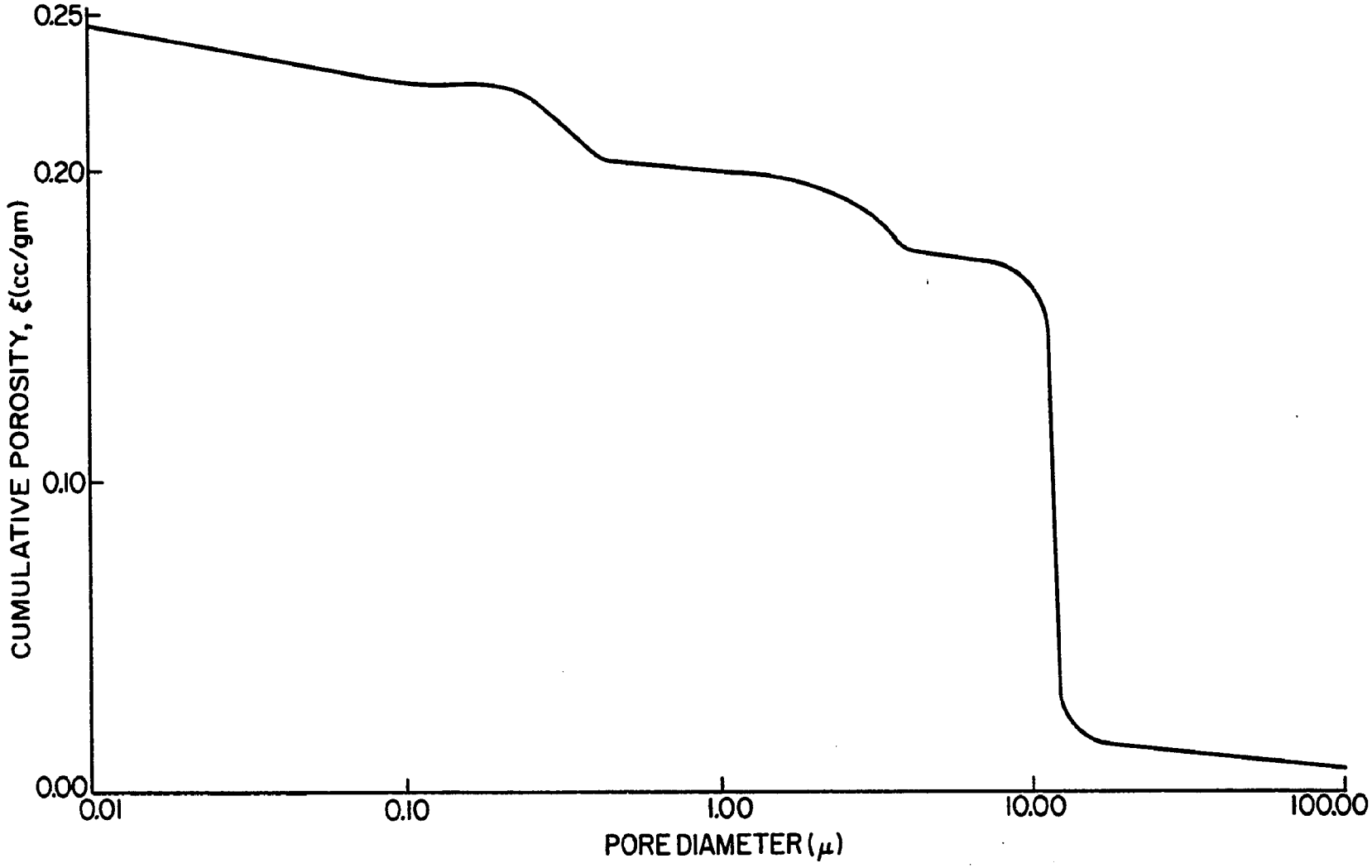

Figure 18 - Cumulative Porosity - FC-11

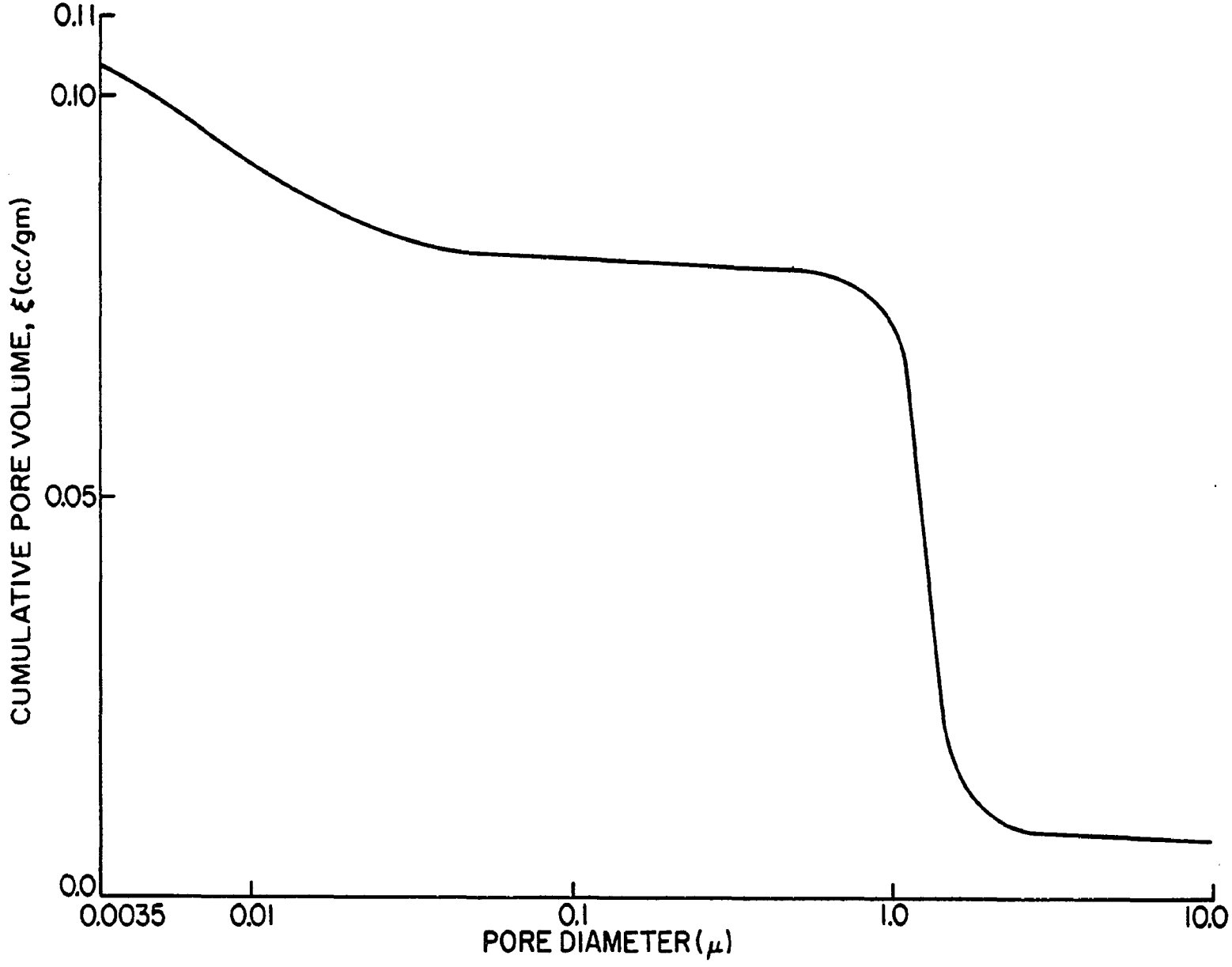

Figure 19 - Cumulative Porosity - FC-25

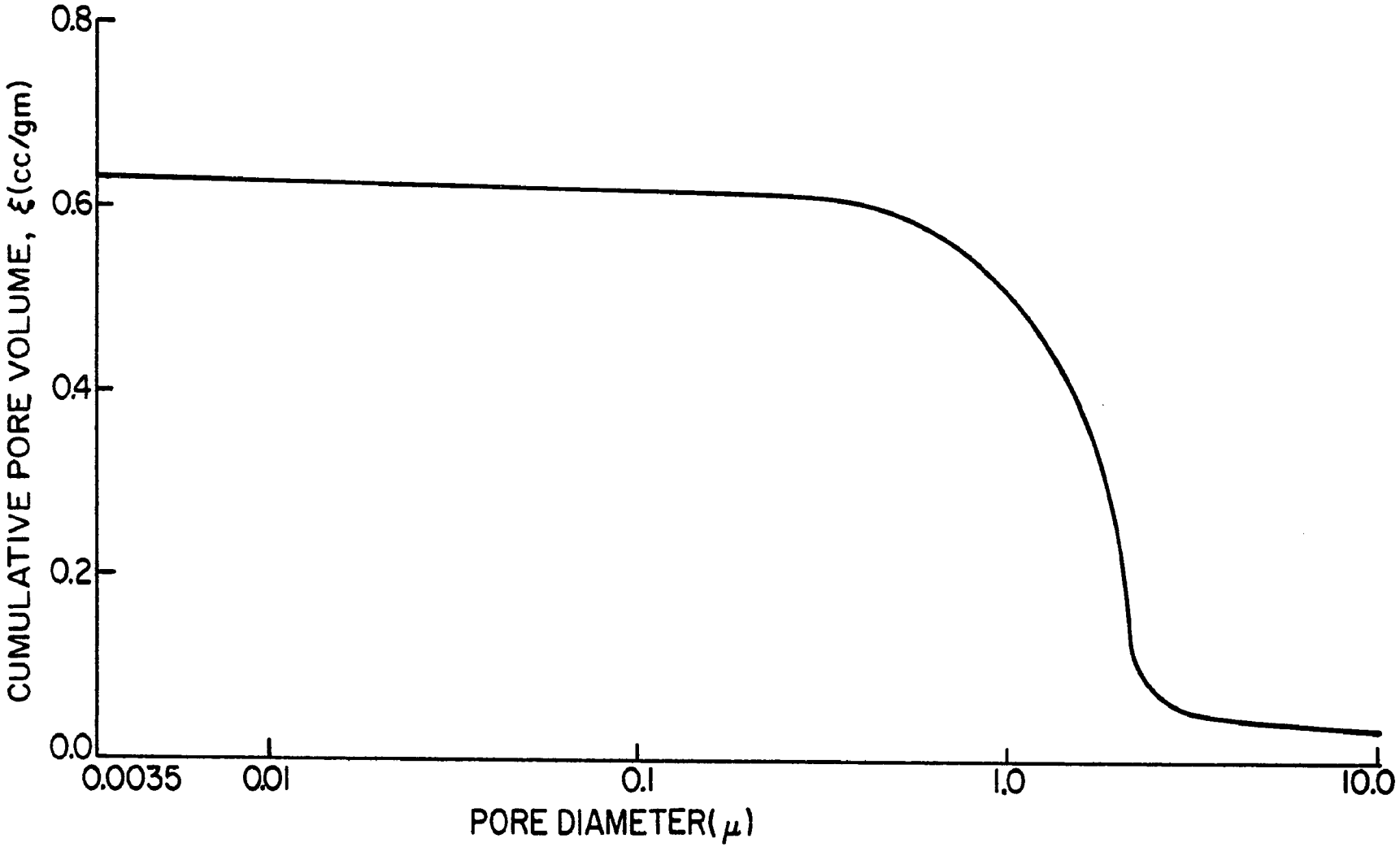

Figure 20 - Cumulative Porosity - POCO-AX

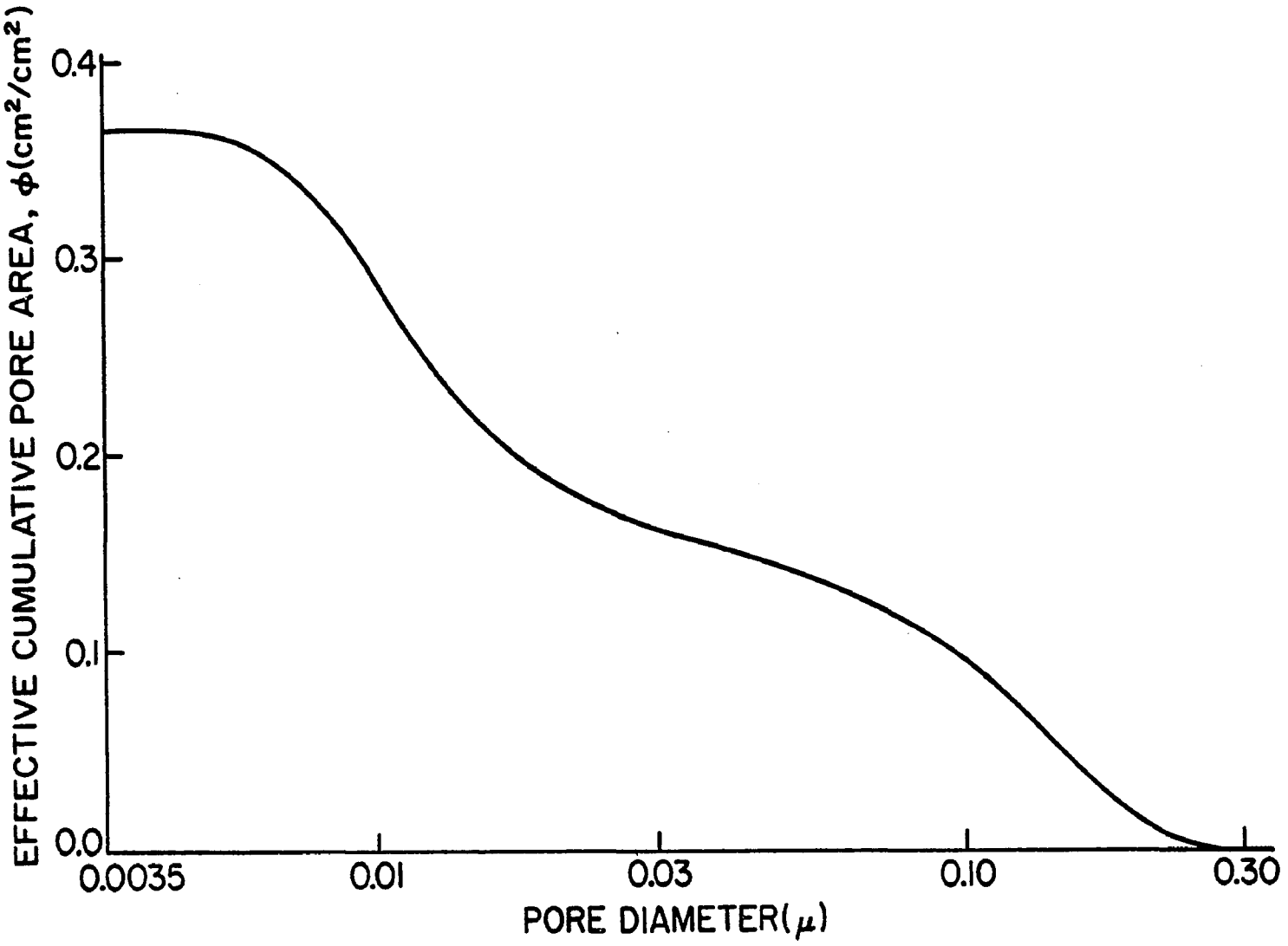

Figure 21 - Effective Cumulative Pore Area - FC-01, N=22

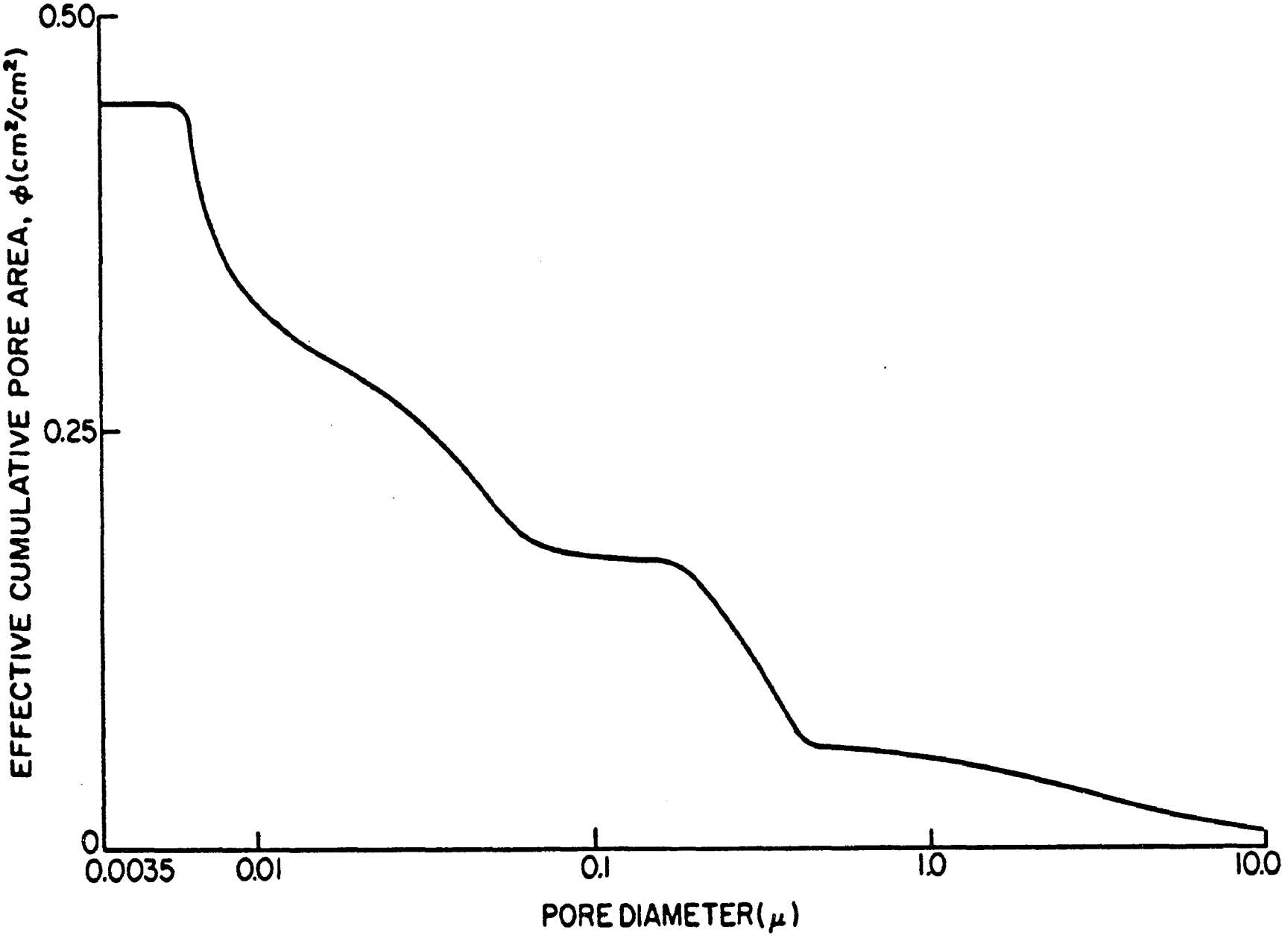

Figure 22 - Effective Cumulative Pore Area - FC-11, N=12

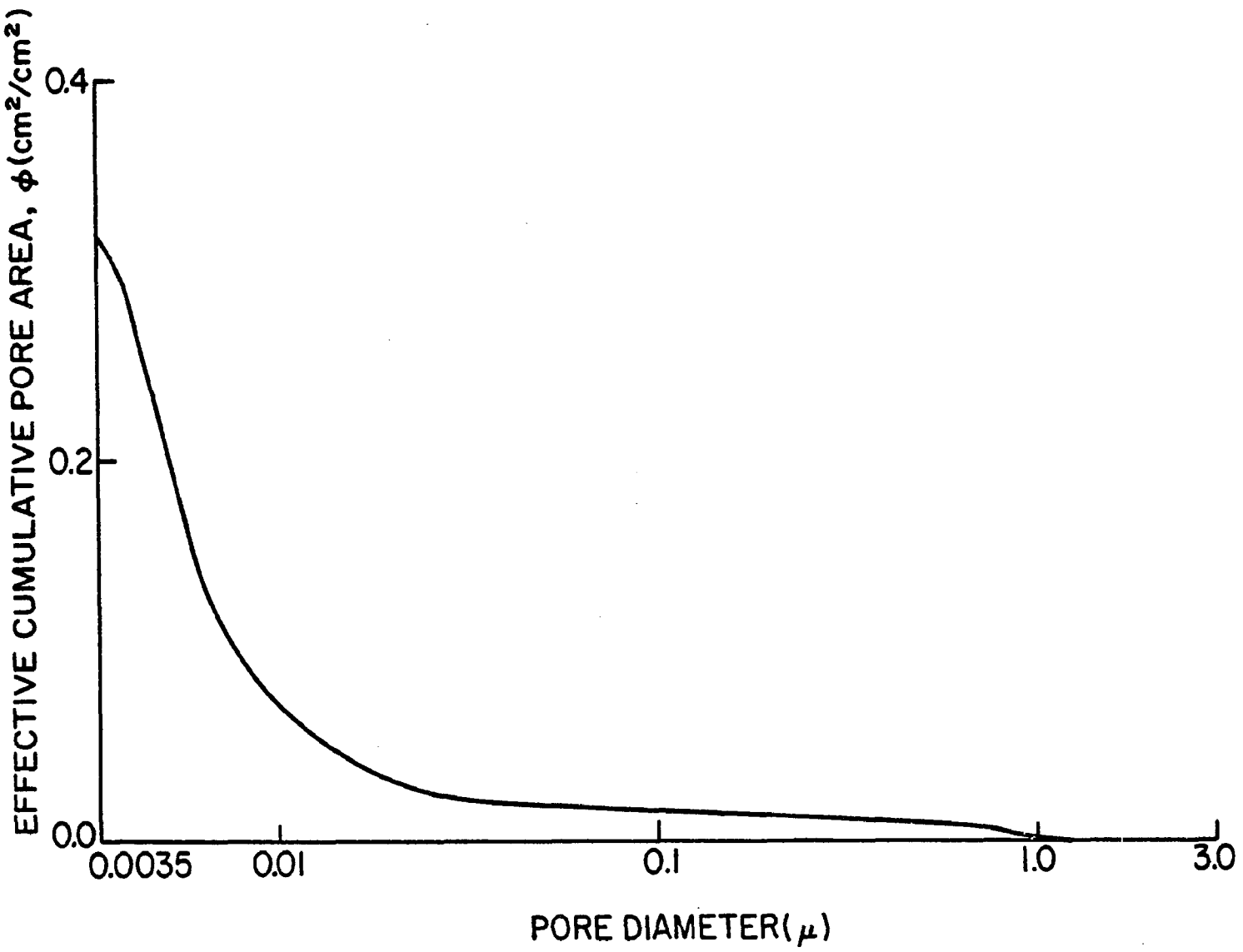

Figure 23 - Effective Cumulative Pore Area - FC-25, N=18

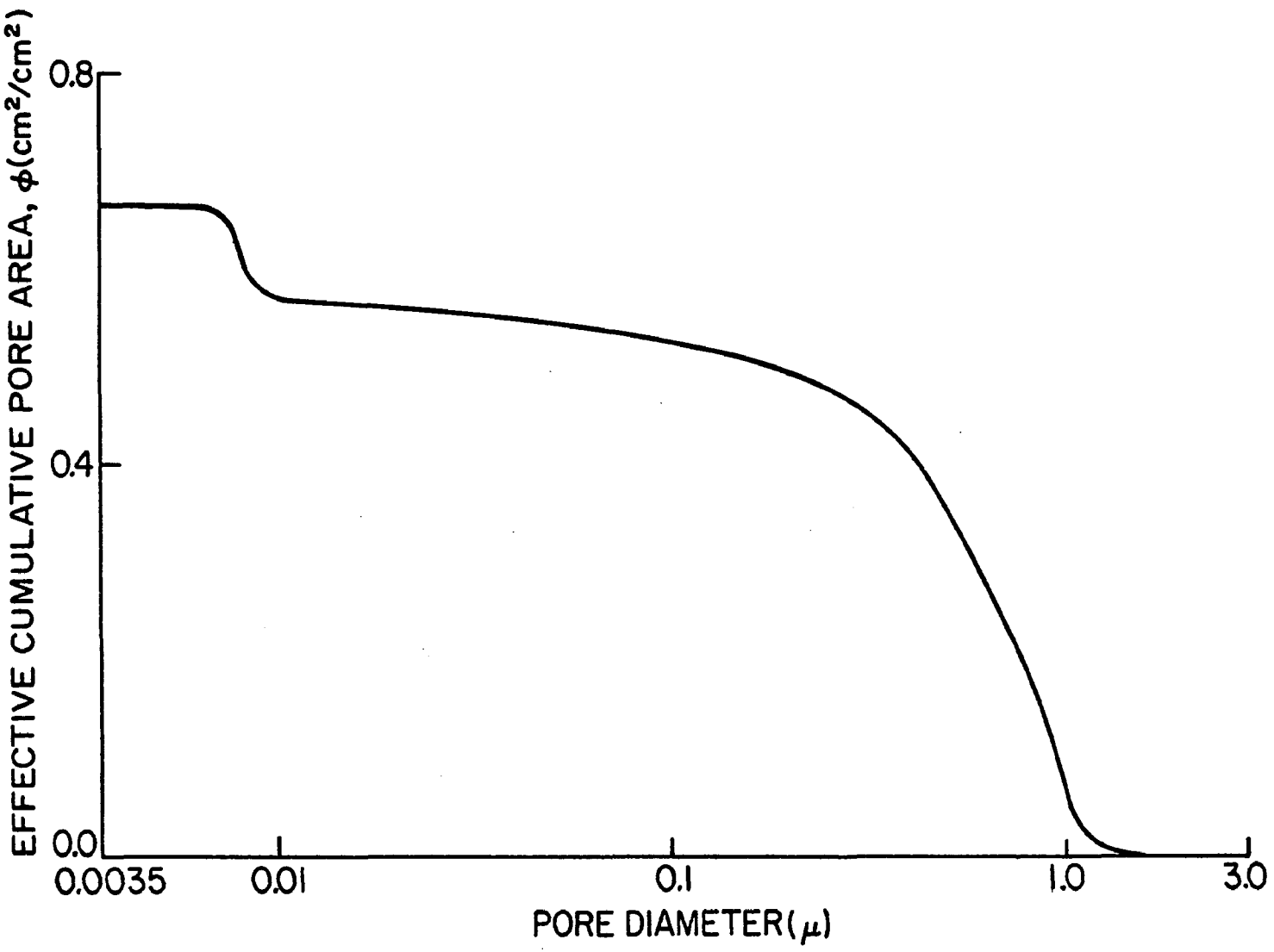

Figure 24 - Effective Cumulative Pore Area - POCO-AX, N=16

of The Pennsylvania State University has developed the software required to determine the pore size distribution from the electronic signal of the SEM.

The major difficulty with the technique is that the boundaries of the pores and pore areas must appear at a significantly higher (or lower) intensity than the background in order for the signal to be processed on the computer. This requirement, in turn, specifies that the surface to be viewed be planar. Considerable difficulty was encountered because of this requirement. Five of the porous samples that were used were so soft that a satisfactory planar surface was never developed. However, a sixth sample, FC-25, was hard enough to obtain the required surface.

A photomicrograph of the planar surface is shown in Figure 25 which clearly shows the irregularly shaped pores. Unfortunately, computer processing of the signal corresponding to this photograph was not successful. The computer processing of this photograph could not be carried out successfully because the level of signal intensity from pores on the surface could not be distinguished from that generated by the voids beneath the surface. The voids immediately beneath the surface of the sample are visible as the apparent dark shadows in Figure 25. This problem was overcome by vacuum depositing gold on the surface of the sample, and by viewing the inverted electronic back scattered image.

The result of this technique is shown in Figure 26 where the light areas correspond to the pore areas and the dark areas to the background. The electronic signal from this was successfully processed.

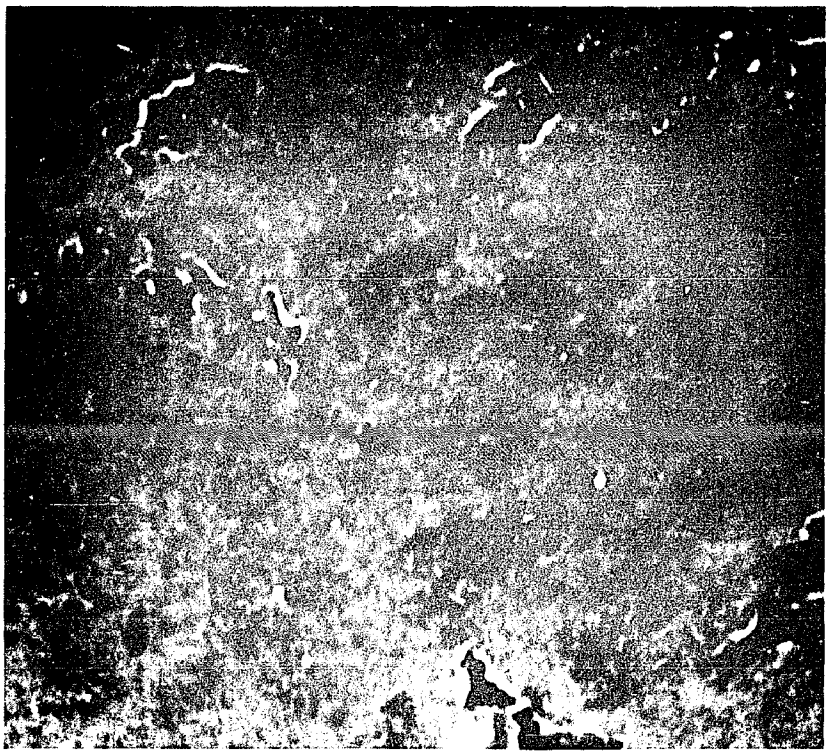

Figure 25 - SEM Photomicrograph, FC-25 Unfilled, Uncoated, 3000 X

Figure 26 - SEM Photomicrograph, FC-25 Goldplated,
Inverted Backscattered Image, 3000 X

The photograph appears hazy because it is taken during the electronic processing and storage of the signal on magnetic tape which is performed at a relatively slow scanning speed. A clearer photograph of the surface is shown in Figure 27. The absence of the shadows in Figure 27 as compared with those present in Figure 25 is due to the gold plating of the sample.

An additional experiment was performed to determine what portion of the pores were voids within the material that had no connecting path with the surrounding pores. In this experiment, a steady flow of a chlorinated hydrocarbon fluid with a suitable catalyst (t-butyl perbenzoate) was forced through the carbon sample mounted in the apparatus shown in Figure 28. After a steady flow had been observed in the glass tube, the flow was shut off, the sample removed and cured at 100°C for several hours. The sample was then sectioned and polished following the techniques outlined above. The resulting photomicrograph of the surface, Figure 29, indicated that virtually all the pores were filled. Only two unfilled pores were found over the entire area of the sample's surface (approximately 0.25 cm^2).

In the scanning electron microscope technique, the cumulative area distribution, ϕ, and pore radius are determined directly from their definitions.

Thus,

$$\phi_o(a) = \sum_{\substack{\text{class} \\ \text{Intervals}}} (A_P/A_S), \ldots , \qquad (4.3)$$

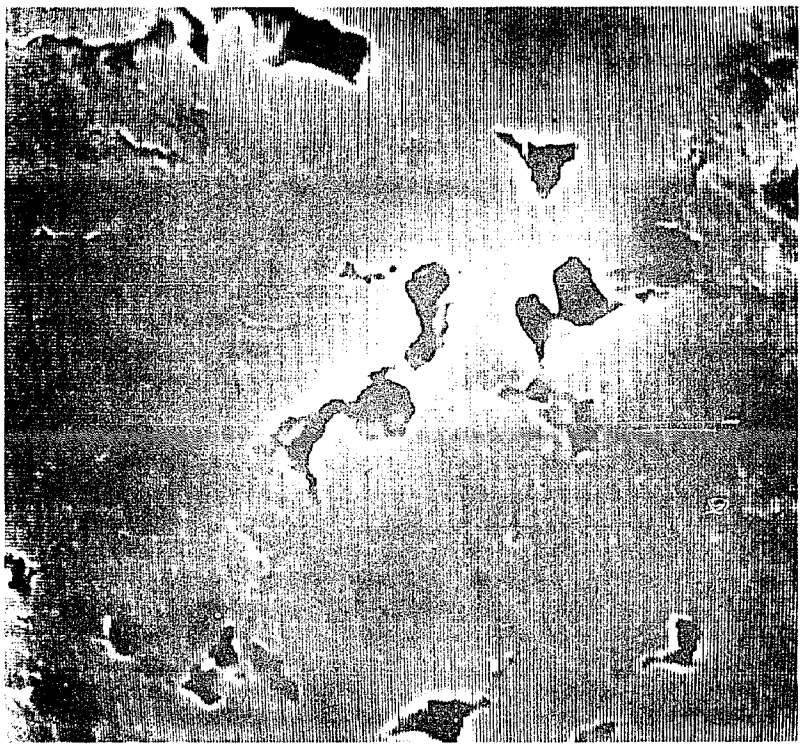

Figure 27 - Sem Photomicrograph, FC-25, Goldplated, Secondary Electron Image, 3000 X

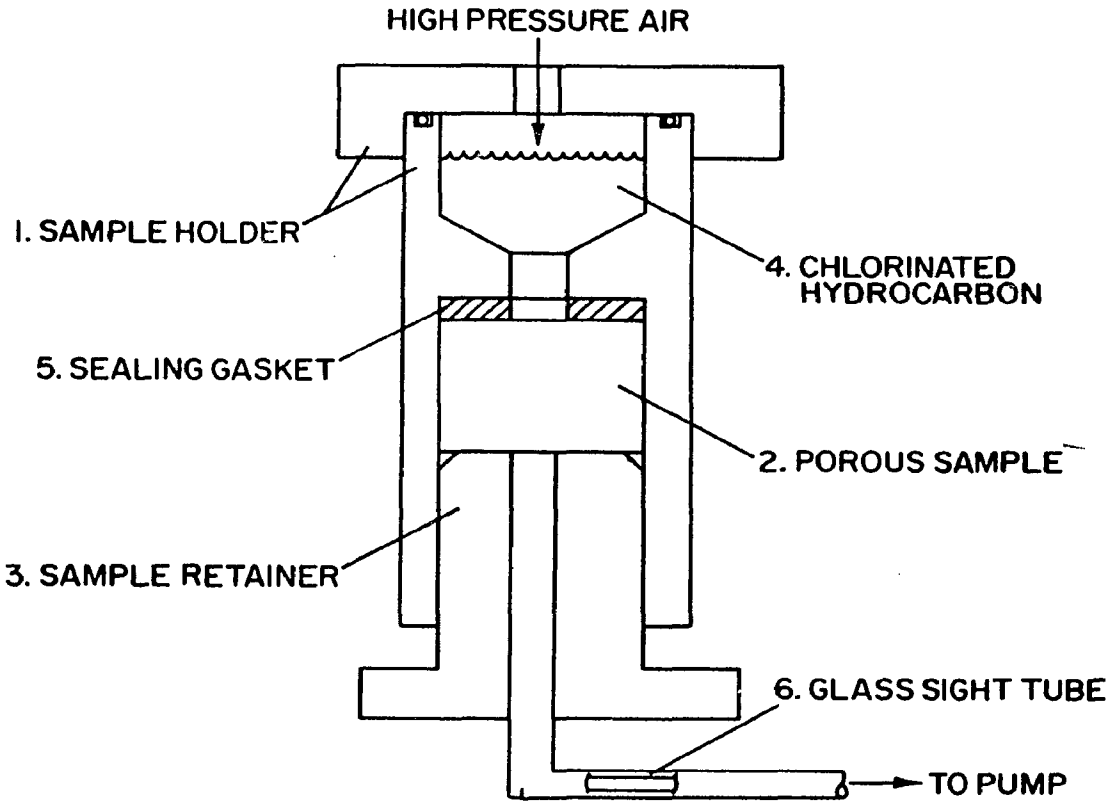

Figure 28 - Experimental Apparatus for Filling of SEM Samples

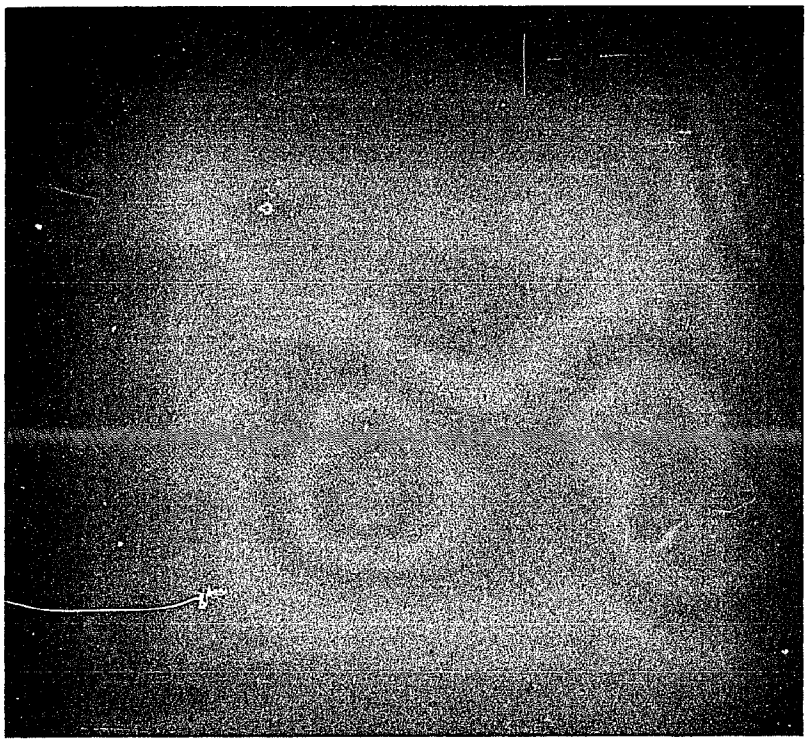

Figure 29 - SEM Photomicrograph, FC-25, Filled and Plated, Inverted Electron Backscattered Image

$$\phi(a) = \phi_o(a)\left[\frac{\phi_o(a)}{\phi_m}\right]^N \quad . \quad . \quad . \quad . \quad , \qquad (4.4)$$

and the pore radius,

$$a = 2\ A_p/P_p \quad . \qquad (4.5)$$

The cumulative area distribution for FC-25 determined by the SEM technique is shown in Figure 30.

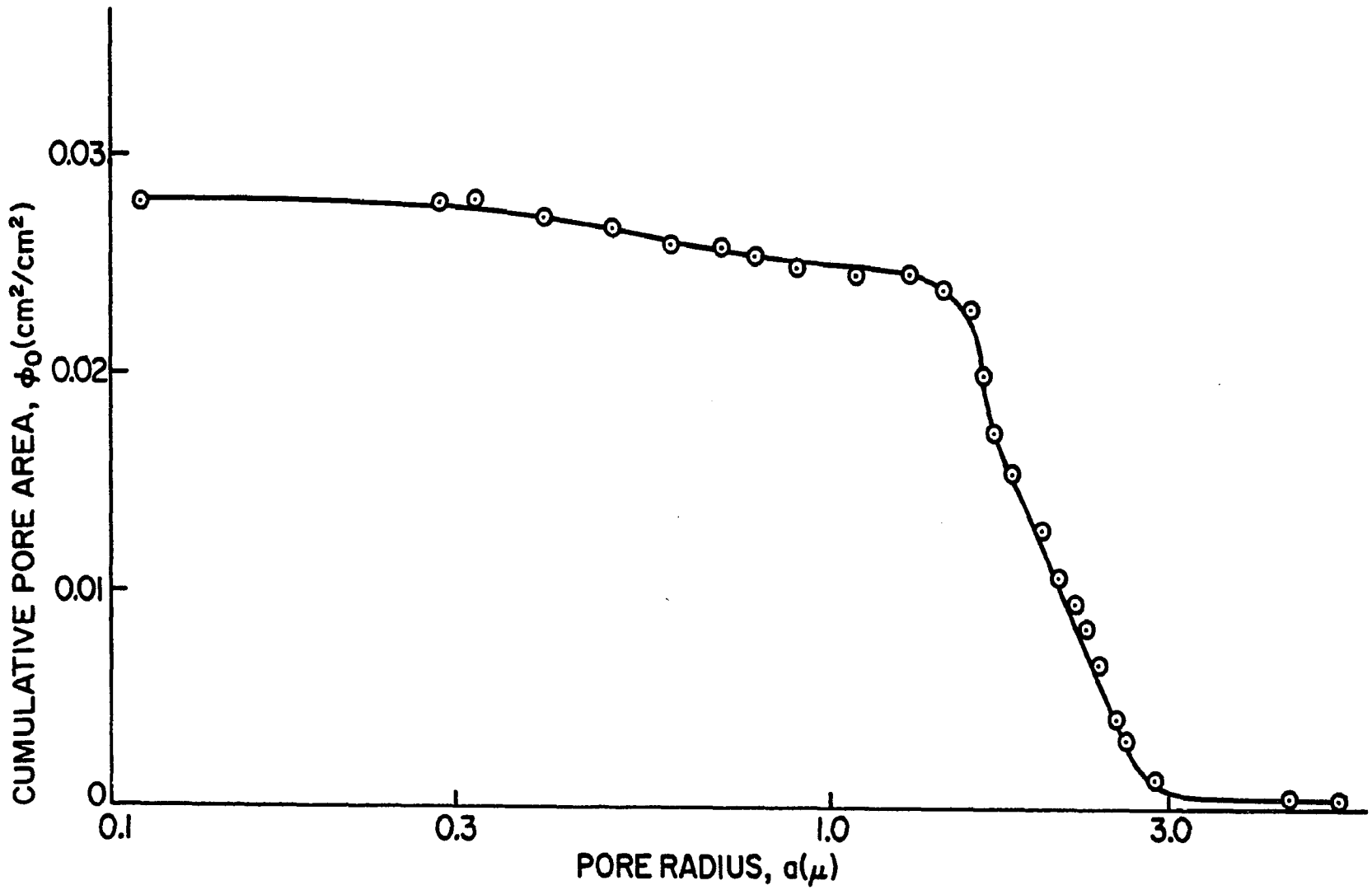

Figure 30 - Cumulative Pore Area, FC-25, SEM Data

CHAPTER V

COMPARISON AND ANALYSIS OF RESULTS

5.1 Pore Size Investigation

The pore size distribution of one medium, FC-25, was determined by two separate techniques: the mercury porosimeter and the scanning electron microscope. The results of those investigations are shown in Figures 31 and 32, respectively. Note that the median pore diameters of the two techniques are quite close, 1.35μ (mercury porosimeter) and 1.9μ. The literature had indicated that the porosimetry technique might under-predict the diameter of the pore. Unfortunately, the cumulative area of the two techniques differ by an order of magnitude. The mercury porosimeter data is thought to be the more reliable for the following reasons. The density of solid carbon can be predicted within ten percent from the mercury porosimeter data, while the SEM data would over-predict the density by an order of magnitude. This discrepancy is hypothesized to be due to the filling of the pores of the sample during the polishing phase of the sample preparation. This would also tend to shift the median pore diameter to a larger size, since the polishing would fill more of the small holes. It is further hypothesized that the shadows apparent in Figure 25 are pores that were filled during the polishing process.

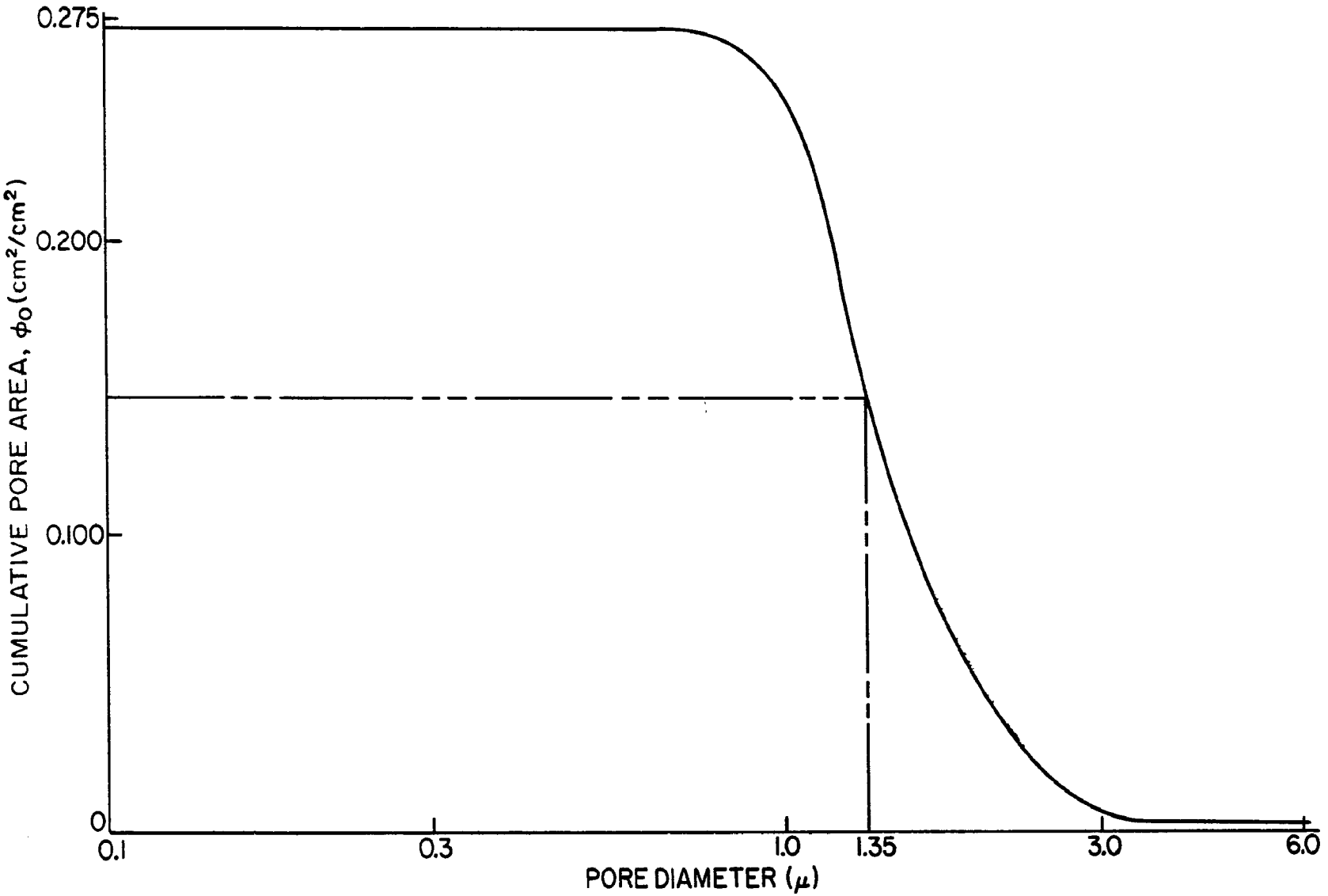

Figure 31 - Cumulative Pore Area, FC-25, Mercury Porosimeter Data

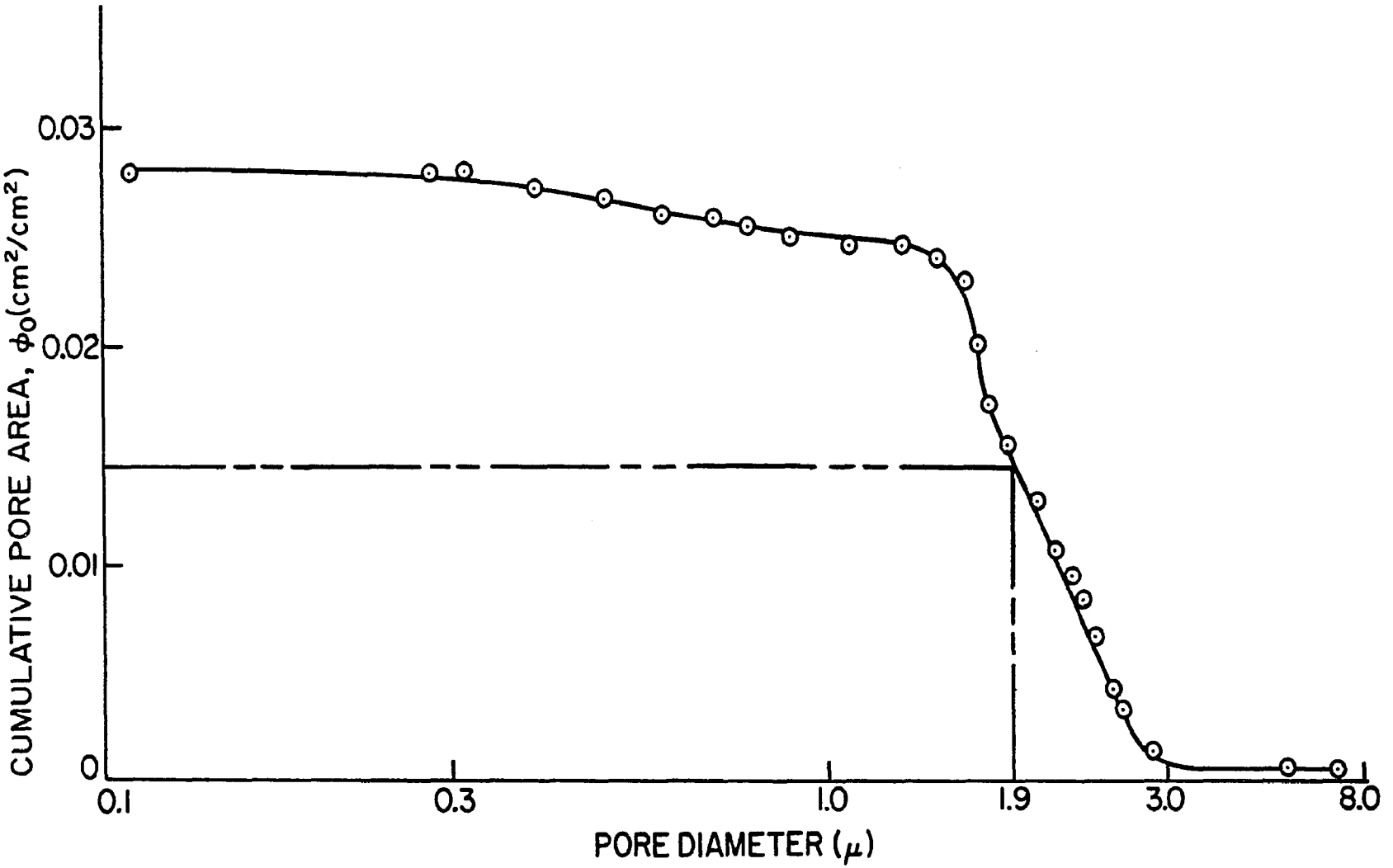

Figure - 32 Cumulative Pore Area, FC-25, SEM Data with Median Diameter

5.2 Solution Technique and Data Presentation

An attempt to obtain a closed form solution of the governing differential equation was not successful. Instead, a numerical solution technique, Hammings Predictor-Corrector method (41) was utilized. In addition, the equation was solved utilizing the Runge-Kutta numerical algorithm (42) for one set of data for each carbon. Table II presents the results of a step size and error size study for a particular set of flow data and carbon medium. It can be seen that the dependent variable does not change significantly, indicating that the step size, error size, and the solution technique used were satisfactory. The results presented here are typical of the results obtained for all the media.

TABLE II

EFFECT OF ERROR AND STEP SIZE UPON

THE DEPENDENT VARIABLE

STEP SIZE CM	ERROR SIZE %	PRESSURE X 10^{-6} dynes/cm^2	
		Hammings	Runge Kutta
0.1	1. x 10^{-1}	0.53364241	0.53364407
0.05	0.5 x 10^{-1}	0.53364969	0.53365012
0.01	1. x 10^{-2}	0.53365671	0.53365184
0.0001	1. x 10^{-3}	0.53364952	0.53364861

The solutions to the differential equation [Equation (3.23) on p. 35] are presented in the following sections. The numerical solution data are all presented as lines, while the experimental data are presented as encircled points.

The outlet pressures for the maximum thickness (1/2 inch) and maximum flow rates for that thickness were used to determine the value of the exponent to be used in the model. Other flow rates for both isothermal and non-isothermal conditions were then predicted using this exponent. The probability exponents used in this study are given in Table III.

TABLE III

PROBABILITY EXPONENT, N, USED FOR ANALYTICAL FLOW PREDICTIONS

MEDIUM	PROBABILITY EXPONENT, N
FC-01	22
FC-11	12
FC-25	18
POCO-A	16

5.3 Comparison and Analysis of Experimental and Analytical Results

5.3.1 Permeability Comparisons. The experimental permeability results are compared with the analytical results in Figure 33 through 36. It should be noted that the range of permeabilities of the four porous media investigated cover over three orders of magnitude (0.5 to 900 cm^2/min). The analytical and experimental permeability data lie within five percent of one another. This correlation is considered good. A tabulation of the experimental permeabilities is presented in Appendix B.

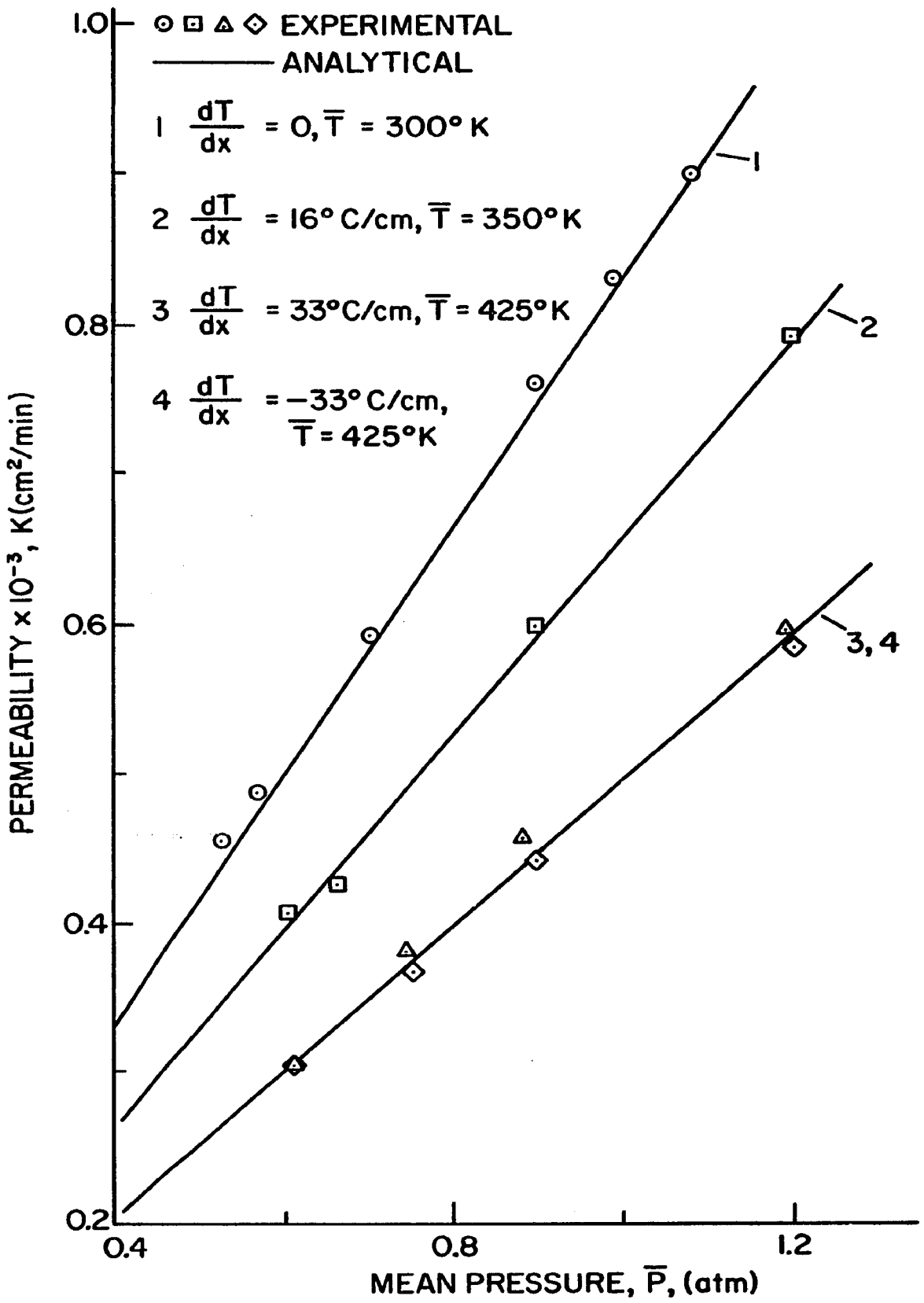

Figure 33 - Permeability Versus Mean Pressure for FC-11

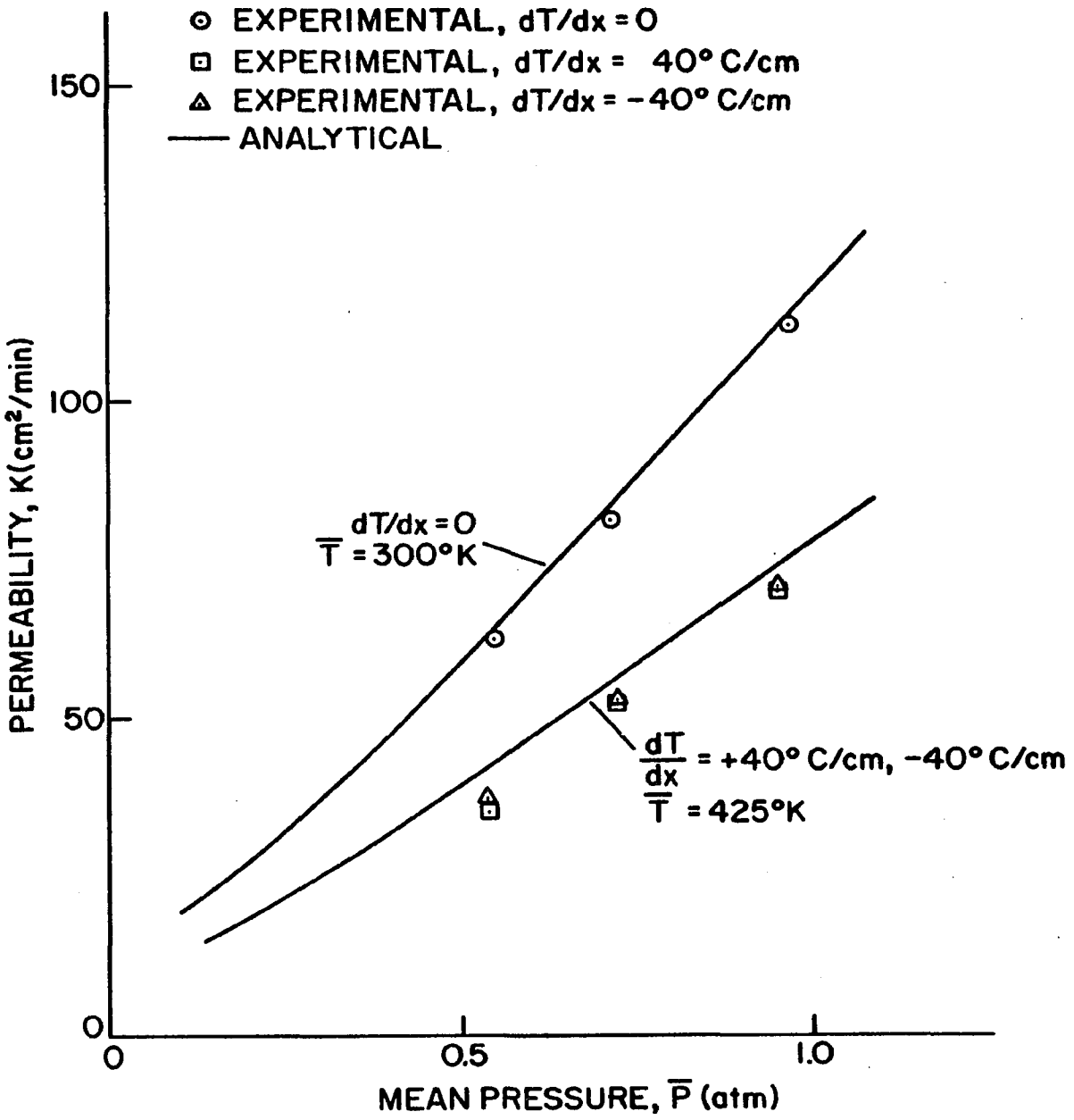

Figure 34 - Permeability Versus Mean Pressure for POCO-AX

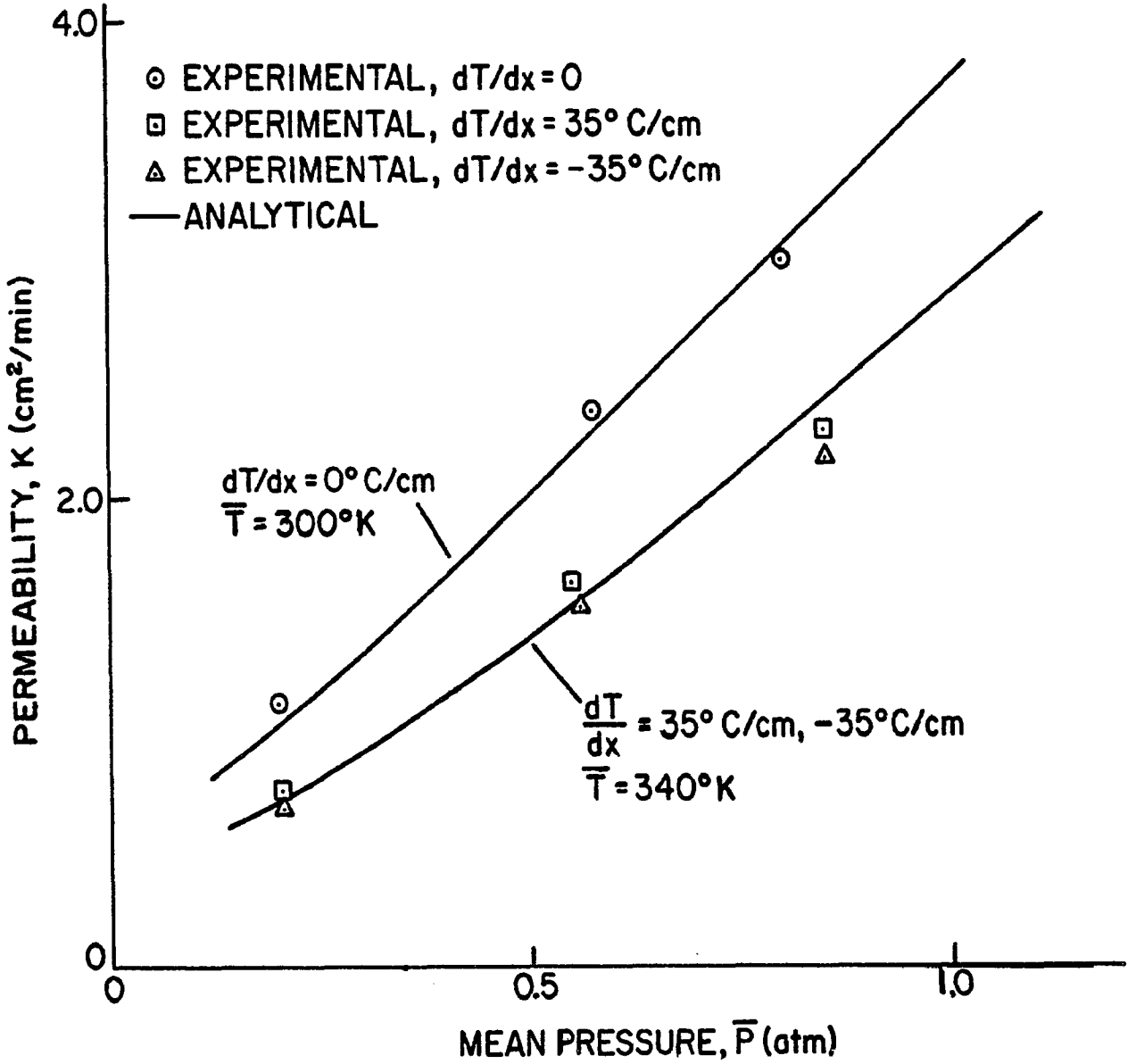

Figure 35 - Permeability Versus Mean Pressure for FC-25

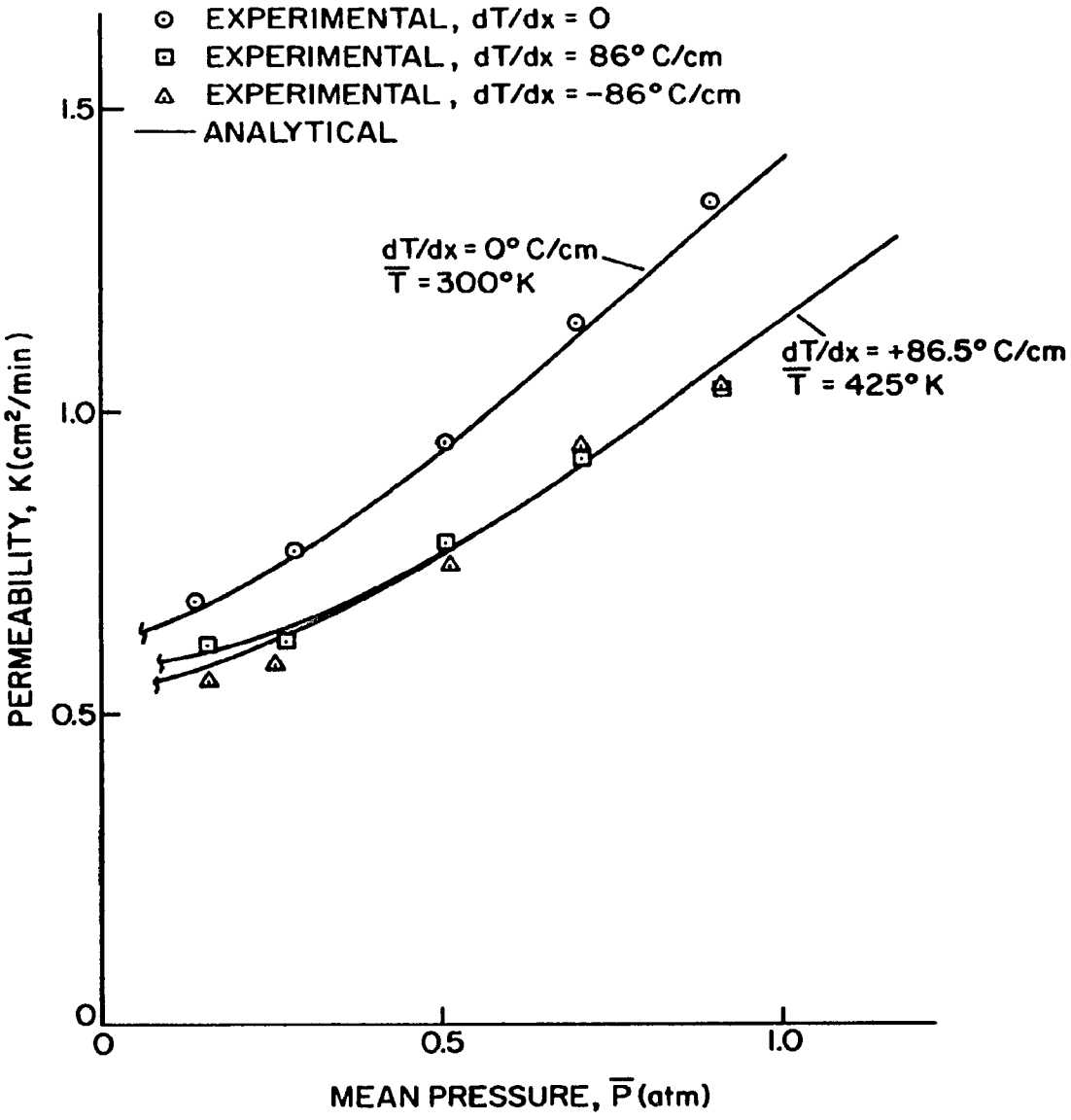

Figure 36 - Permeability Versus Mean Pressure for FC-01

The experimental pressure drop could be measured within 0.05 inches of mercury or ethylene glycol. This contributes a maximum error of $\pm$5% to the large values of the permeability and small error (< 1%) to the small values. The flow rate could be determined within $\pm$2 cm^3/min and contributes a maximum error of $\pm$20% at the smallest value of the permeability (0.55 cm^2/min). This error is reduced to $\pm$10% at a permeability of 1 cm^2/min and further reduced to $\pm$5% at 2 cm^2/min. At permeabilities greater than 2 cm^2/min, the flow error contribution is continuously reduced as the permeability value is increased. Thus all the experimental values of the permeability greater than 2 cm^2/min and all experimental values of the outlet pressures lie within $\pm$5% of their true values.

The permeability measurements and analytical data presented in Figures 33 through 36 agree qualitatively with results published in the literature (23, 24, 25). It is impossible to make a quantitative comparison with the published results because the pore size distributions of the porous media used in these references are unpublished.

In the continuum regime, the permeability is linear (18). This agrees quite well with the data of Figure 33 where slip and free molecule flow analytically account for less than 0.1% of the flow. The non-linear behavior of the permeability in Figures 34 through 36 is attributed to the onset of slip and free molecule flow.

The analytical solutions for FC-01 each exhibited a relative minimum as shown in Figure 37. After the solution had gone through the relative minimum, it appeared to reach a maximum and then approach zero.

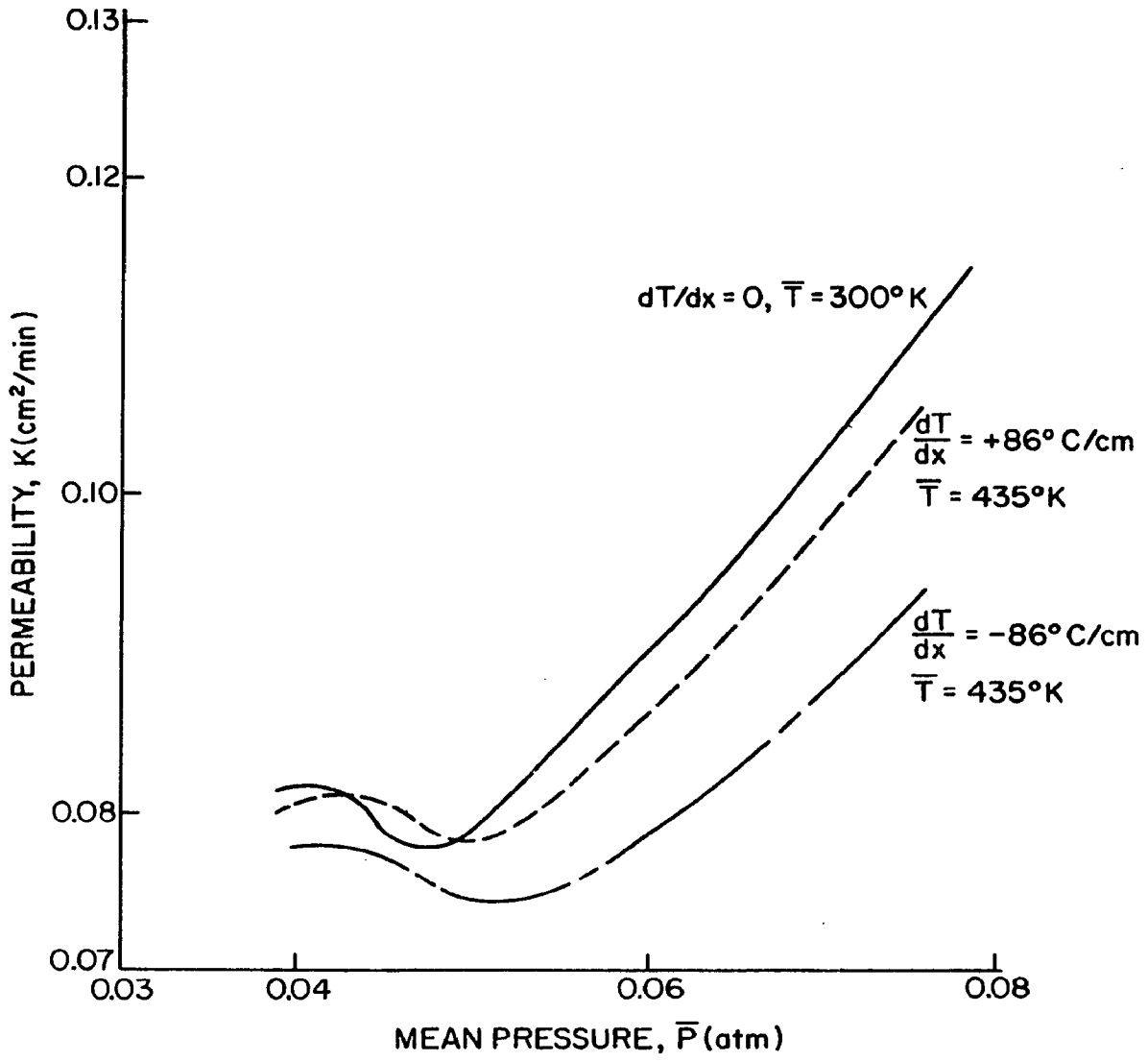

Figure 37 - FC-01 - Permeability Versus Mean Pressure at Low Pressures

Although no experimental data were collected by this author, Grove and Ford (25) have experimentally observed a minimum in the permeability curve. An attempt was made to obtain the numerical solution between the minimum and zero mean pressure. A complete numerical solution was not obtained because of the time required to perform the integration at very small (0.0001) step sizes over a large interval. The few points obtained beyond the relative maximums indicated that the permeability had started to decrease again. By lowering the inlet pressure, several solutions with relative minimum values were found. These minimums occurred at a point where 80% of the flow was free molecule. A plot of these analytically predicted minimum permeabilities and the mean pressures at which they occurred is shown in Figure 38. It is hypothesized that the minima occur because of the trade off between the slip and free molecule flow contributions and the two-step characteristic of the cumulative area distribution of FC-01 (Figure 21). The two step characteristic is important as this allows the area available for flow in the free molecule regime to increase, reach a constant, and then increase again as the solution proceeds. It should be emphasized that minima predicted are a characteristic of the model of the porous medium and not of the mechanics of the gas. This is important, as a similar phenomenon is found in flow through capillary tubes under free molecule flow conditions (43). It is this fact that implies that the phenomena observed by Grove and Ford (12) may be due to the mechanical behavior of the gas rather than the geometrical construction of the porous medium.

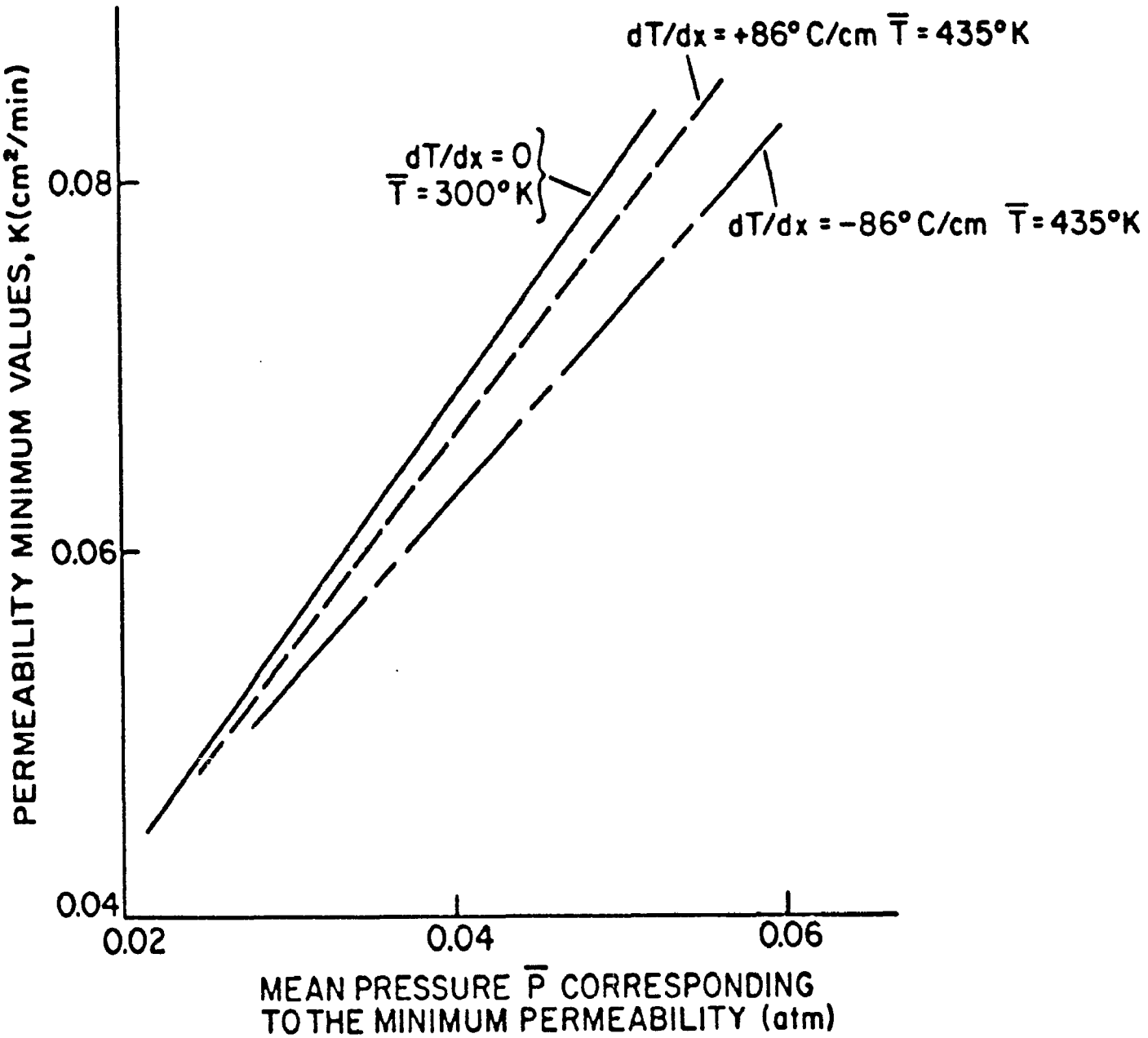

Figure 38 - FC-01 - Permeability Minimum Values Versus Corresponding Mean Pressure at Constant Mass Flux

Table IV presents a comparison between permeability constants of Equation (2.22) for the porous media tested here and other media reported in the literature.

Both Hutcheon (23) and Grove and Ford (25) were working with fine pored nuclear garde graphite which is considerably less porous than most of the media tested in this work, but similar to FC-01.

TABLE IV

PERMEABILITY CONSTANT FOR VARIOUS MEDIA - A COMPARISON BETWEEN PRESENT AND PREVIOUS WORK

Carbon or Author	$B_o \times 10^{10}$, cm^2	$K_o \times 10^3$, cm
FC-01	2.17	0.22
FC-11	1390.00	2.00
FC-25	5.46	0.21
POCO	200.00	0.20
Hutcheon (23)	0.014	0.025
Grove - Ford (25)	1.89	0.113

At large values of B_o, the intercept is difficult to determine accurately, as the curve is quite steep. Thus the values of K_o for FC-11 and POCO are open to question. Table V shows a comparison between the flow resistances reported by the manufacturer and those measured here. This agreement is considered good.

TABLE V

FLOW RESISTANCES* FOR VARIOUS MEDIA

Medium	Resistance - mm Hg		
	Analytical	Experimental	Pure**
FC-01	1750.00	1800.	2000.
FC-11	2.1	2.4	3.0
FC-25	6.40	6.60	500.

* Pressure drop for 1 cc/min cm^2 of N_2 exhausting to standard atmosphere at standard temperature 1 cm thick sample.

** Pure Carbon Co., Saint Mary's, Pennsylvania.

5.3.2 Pressures - Position Comparisons. The experimentally measured and analytically determined pressures as a function of position are presented in Figures 39 through 43. The analytical and experimental pressures drops lie within ten percent of one another; this correlation is considered good. A tabulation of the experimental exhaust pressures in presented in Appendix B.

In the continuum regime, the isothermal pressure profile is linear, as is apparent from Figures 39 and 40. The advent of slip flow tends to increase the isothermal pressure gradient resulting in a non-linear isothermal pressure curve. This phenomenon can be observed in Figures 41 and 42 where the isothermal pressure - position curves are non-linear. The transition from slip flow into free molecule flow is observed in Figure 43 as the decrease in the slope of the pressure curve.

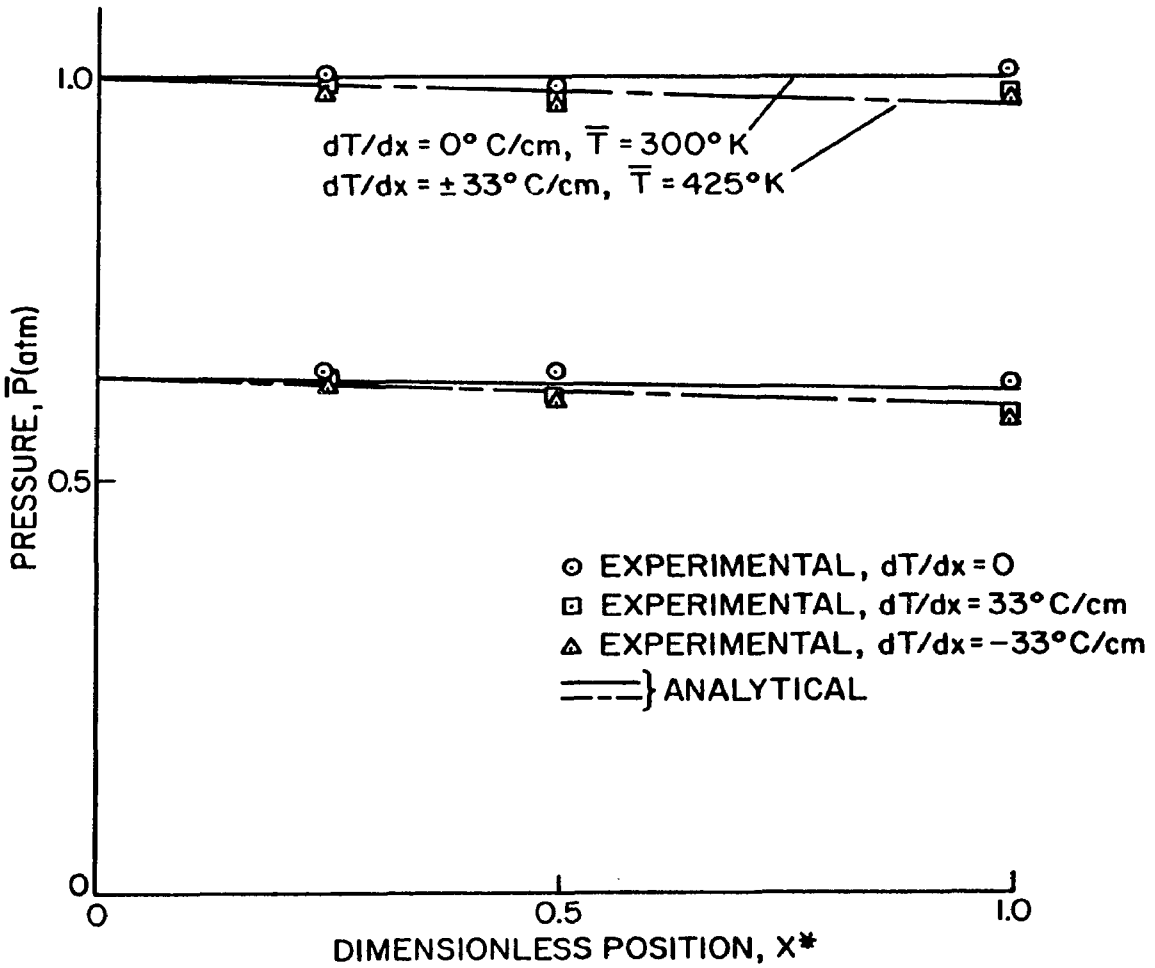

Figure 39 - Pressure Versus Position, FC-11, $\dot{m} = 0.168 \times 10^{-3}$ gms/cm^2 sec

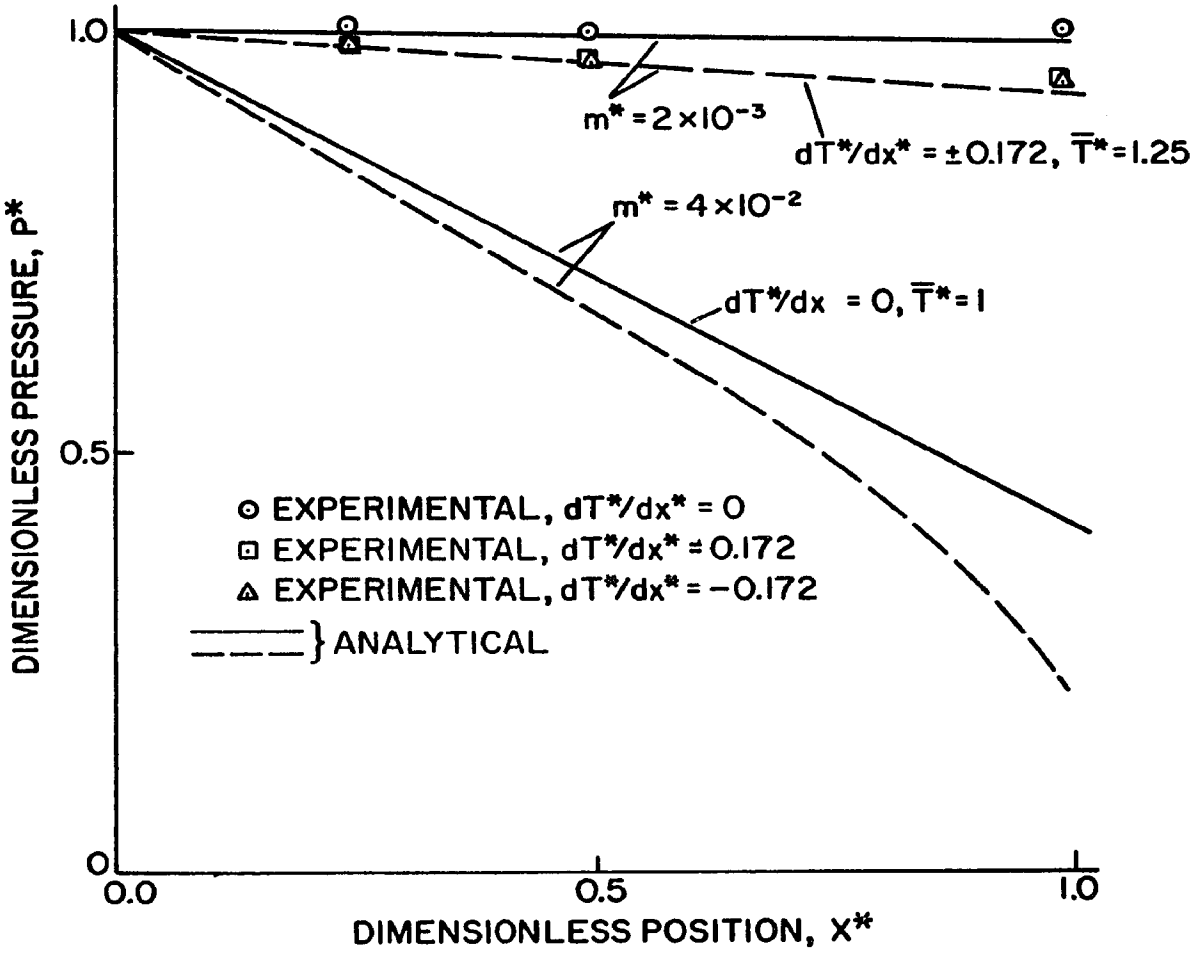

Figure 40 - Pressure Versus Position, POCO-AX, KN_r^{-10}, $\dot{m}^* = 2 \times 10^{-3}$

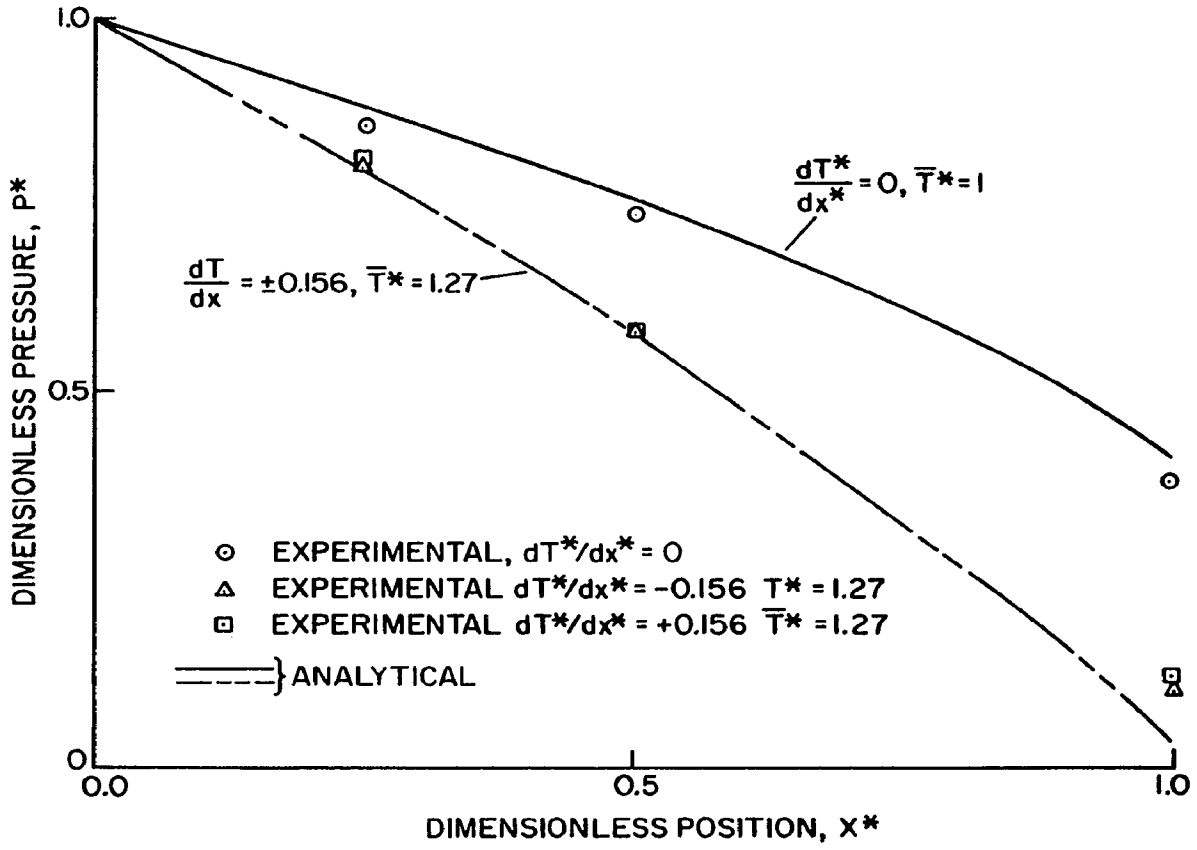

Figure 41 - Pressure Versus Position, FC-25, $KN_r = 6$, $\dot{m}^* = 0.95$

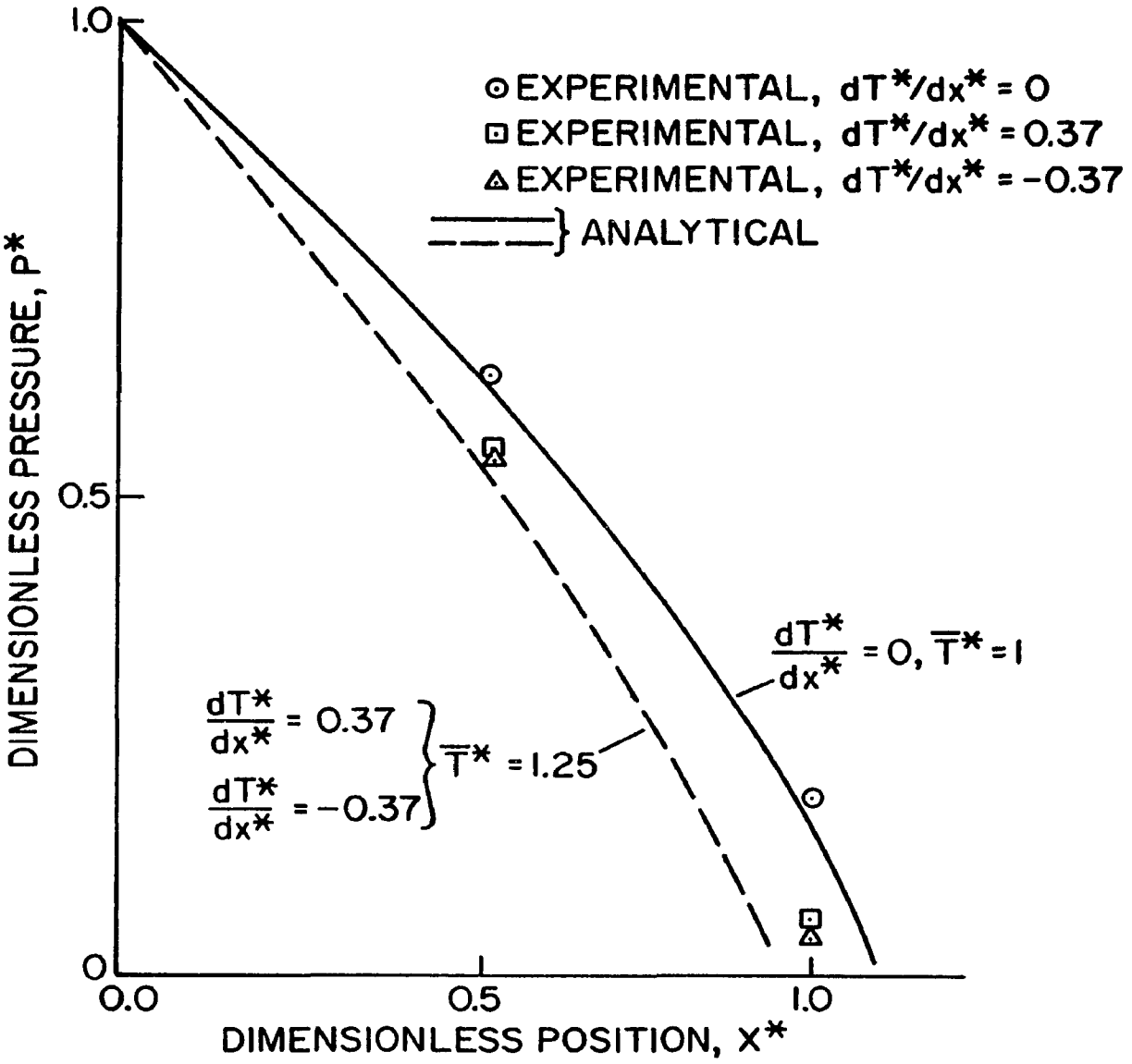

Figure 42 - Pressure Versus Position, FC-01, $KN_r = 2$, $\dot{m}^* = 0.072$

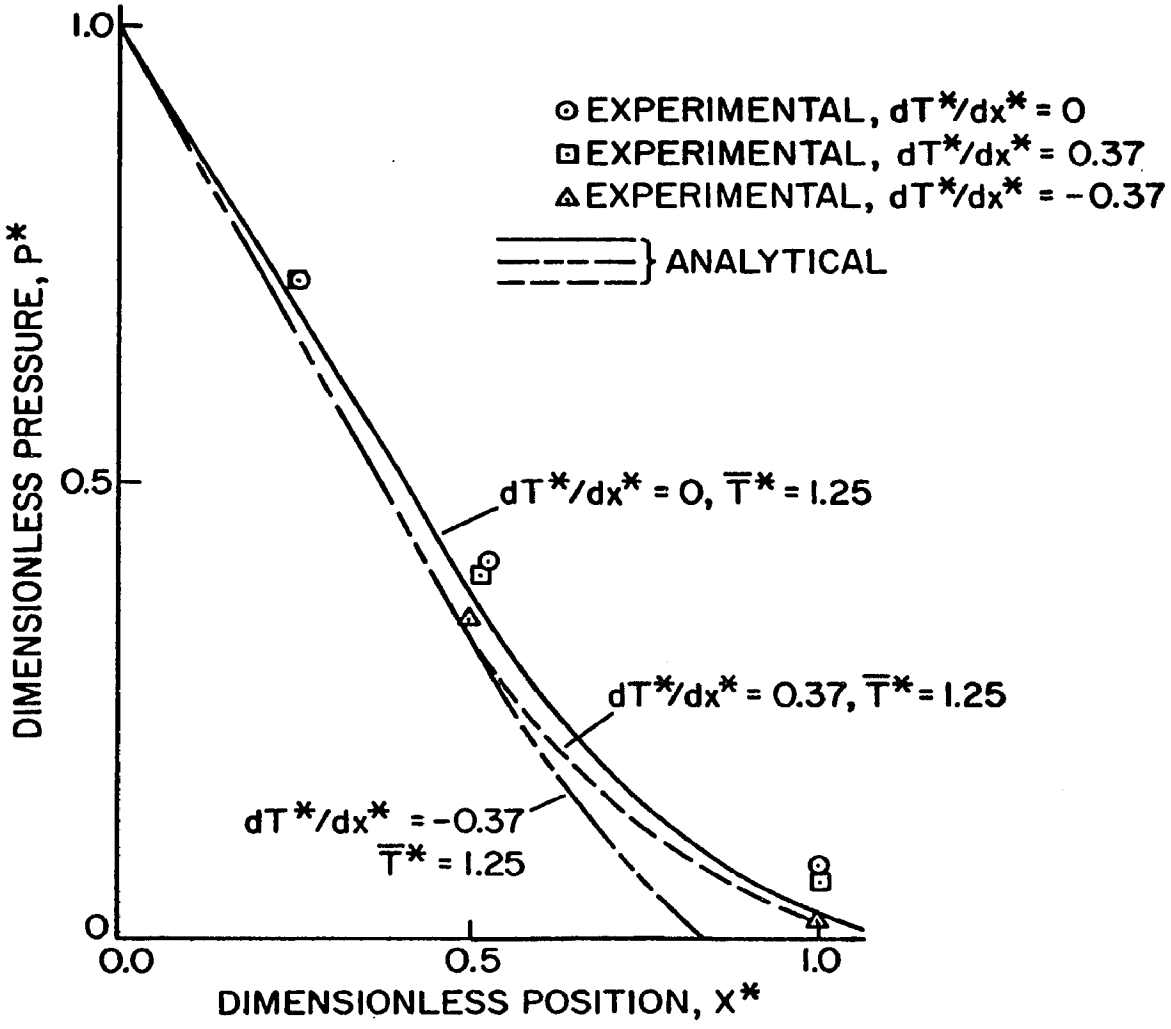

Figure 43 - Pressure Versus Position, FC-01, KN_r = 0.16, $\dot{m}^*$ = 0.084

The non-isothermal behavior of the pressure in the continuum and slip regimes (Figures 39 through 42) is due primarily to changes in the density and viscosity due to the increased absolute temperature. Both the experimental data and analytical model indicated that the magnitude and sign of the temperature gradient did not influence the flow in the continuum and slip regimes. Changes in the porous medium structure due to the non-isothermal conditions were investigated and found to be insignificant at the temperatures utilized in this study (less than 0.1% change in median pore diameter).

Non-isothermal effects were observed in the finest pored medium (FC-01) used and are evident in Figure 43. Here, the positive temperature gradient curve approaches the isothermal curve at the exit to the medium, while the negative temperature gradient curve departs from the isothermal curve at the exit. The positive temperature gradient aids flow in the free molecule regime, thereby offsetting the effect of the increase in the average temperature. In the free molecule regime, the effect of a negative temperature gradient is to hinder the flow. Since the average temperature of the system is also increased, the flow is further reduced, causing the negative temperature gradient curve to depart from the isothermal curve in Figure 43. This phenomenon was also observed in the experimental behavior of the system.

5.4 Analytical Predictions of Component Mass Fluxes

Figures 44 through 48 present analytical data describing the behavior of the component mass fluxes, continuum, slip, and free molecule

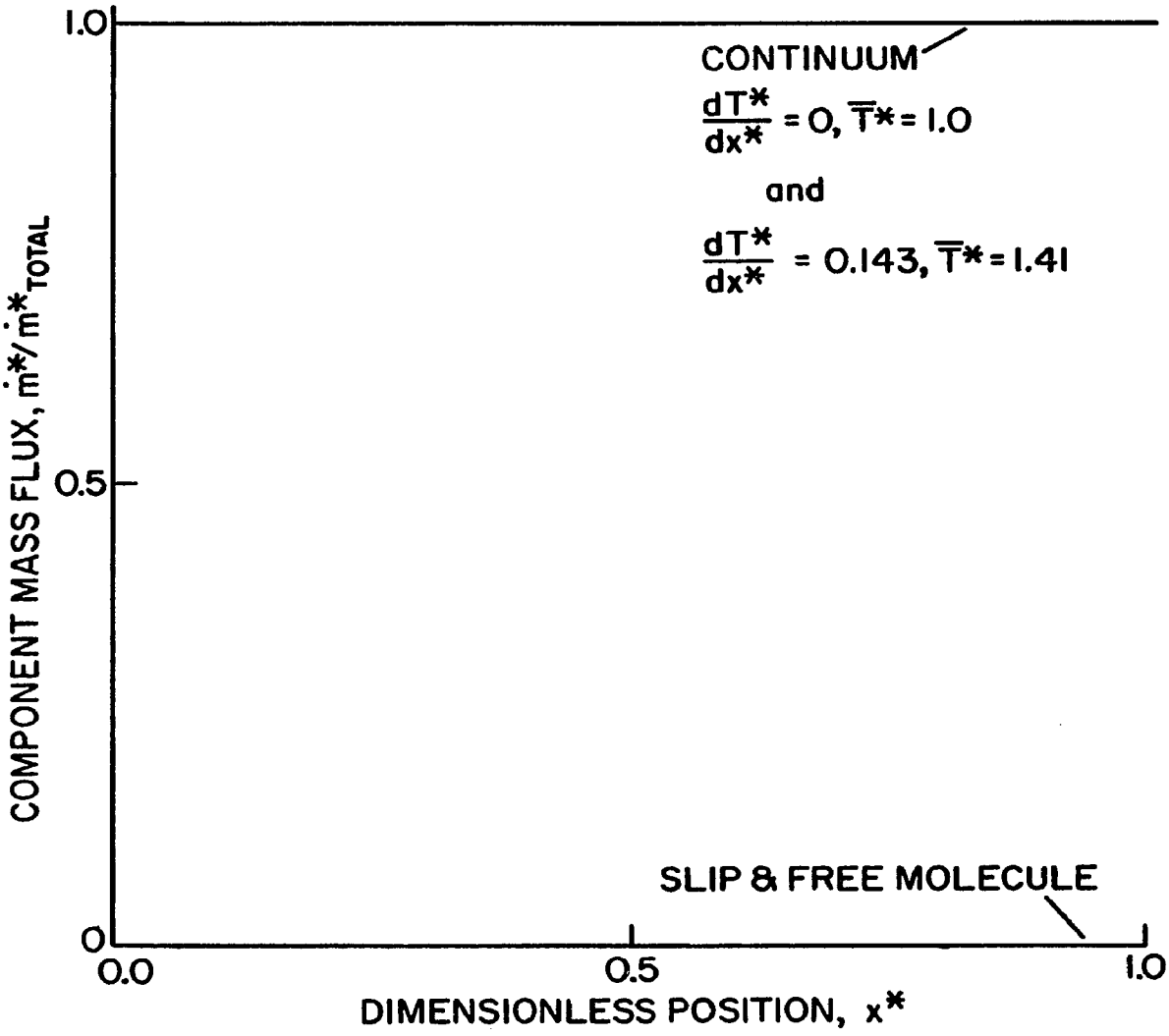

Figure 44 - Component Mass Fluxes for FC-11, KN_r = 50, $\dot{m}^*$ = 0.0011

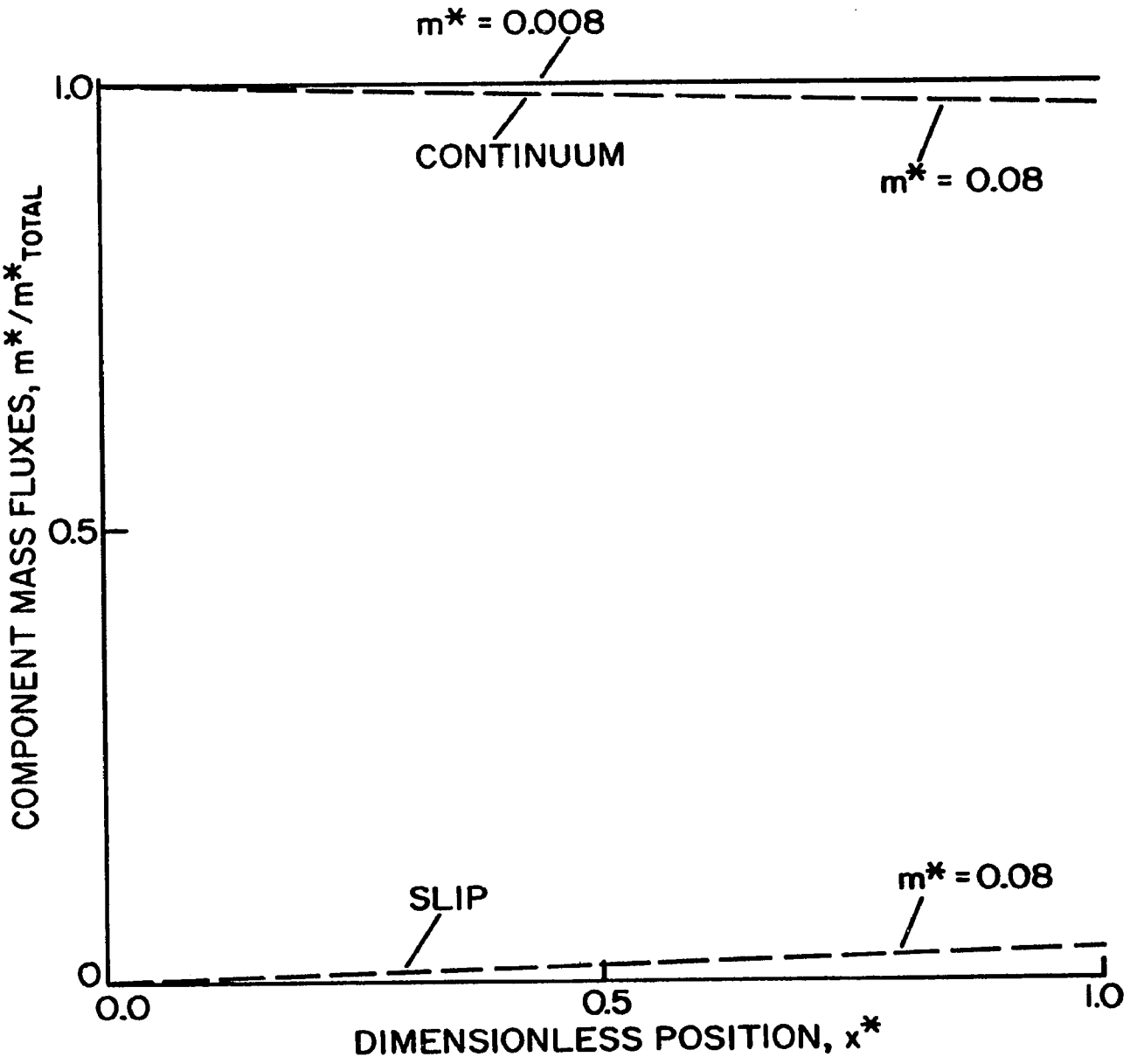

Figure 45 - Isothermal Component Mass Fluxes for POCO, KN_r = 10, $\dot{m}^*$ = 0.008 and $\dot{m}^*$ = 0.08

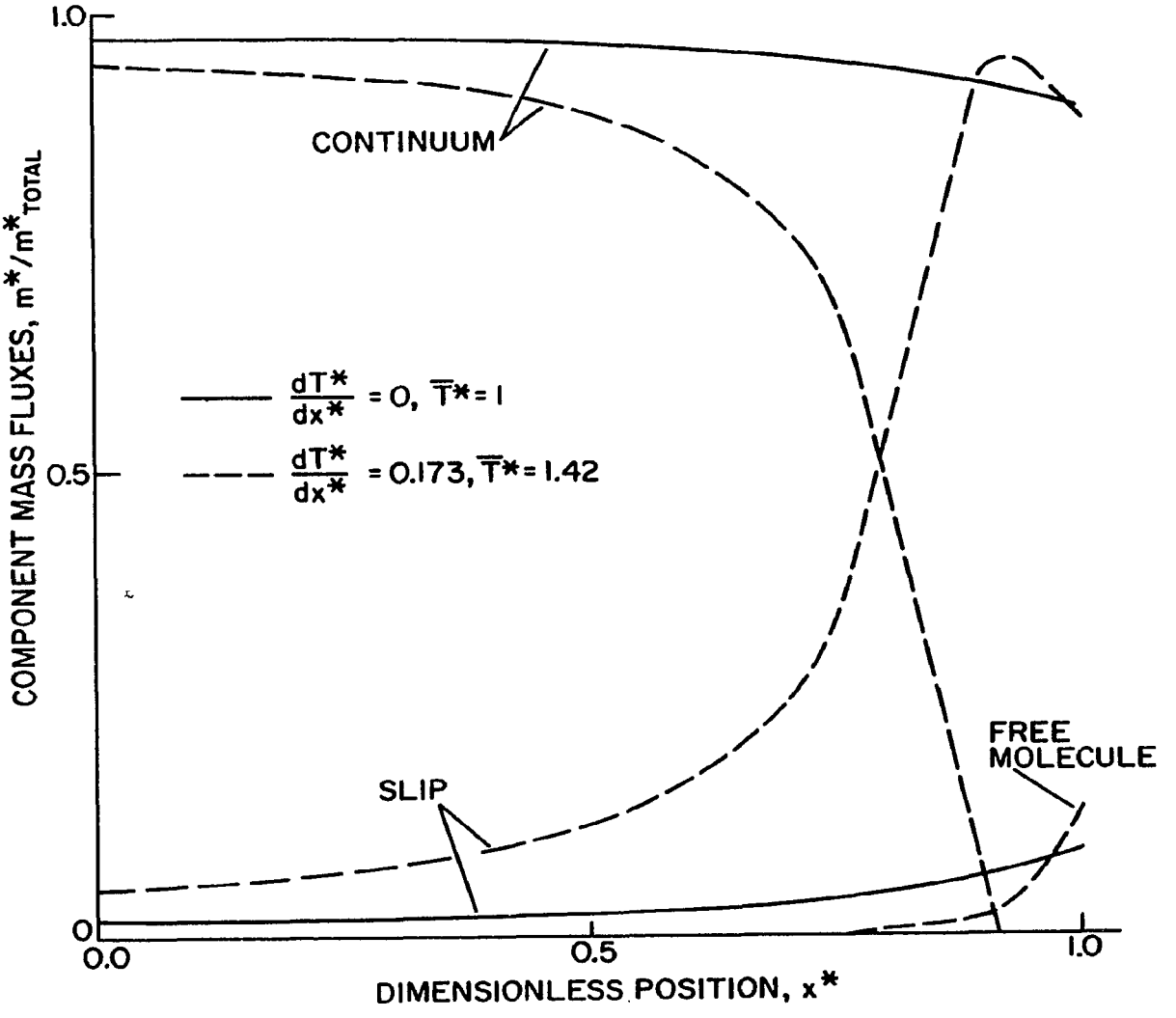

Figure 46 - Component Mass Fluxes for FC-25, $KN_r = 6$, $\dot{m}^* = 0.95$

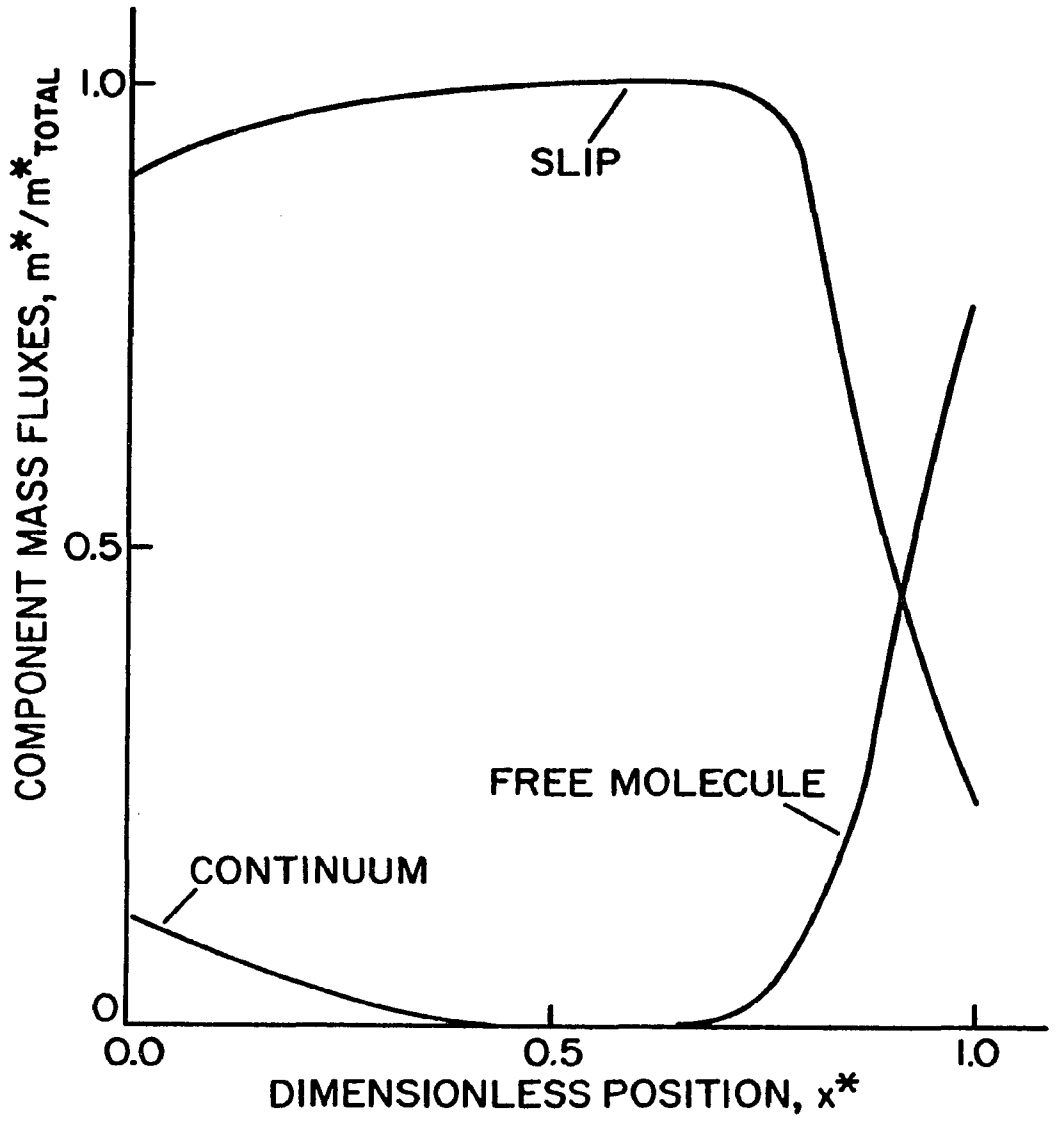

Figure 47 - Isothermal Component Mass Fluxes for FC-01, KN_r = 2.0, $\dot{m}^*$ = 0.23

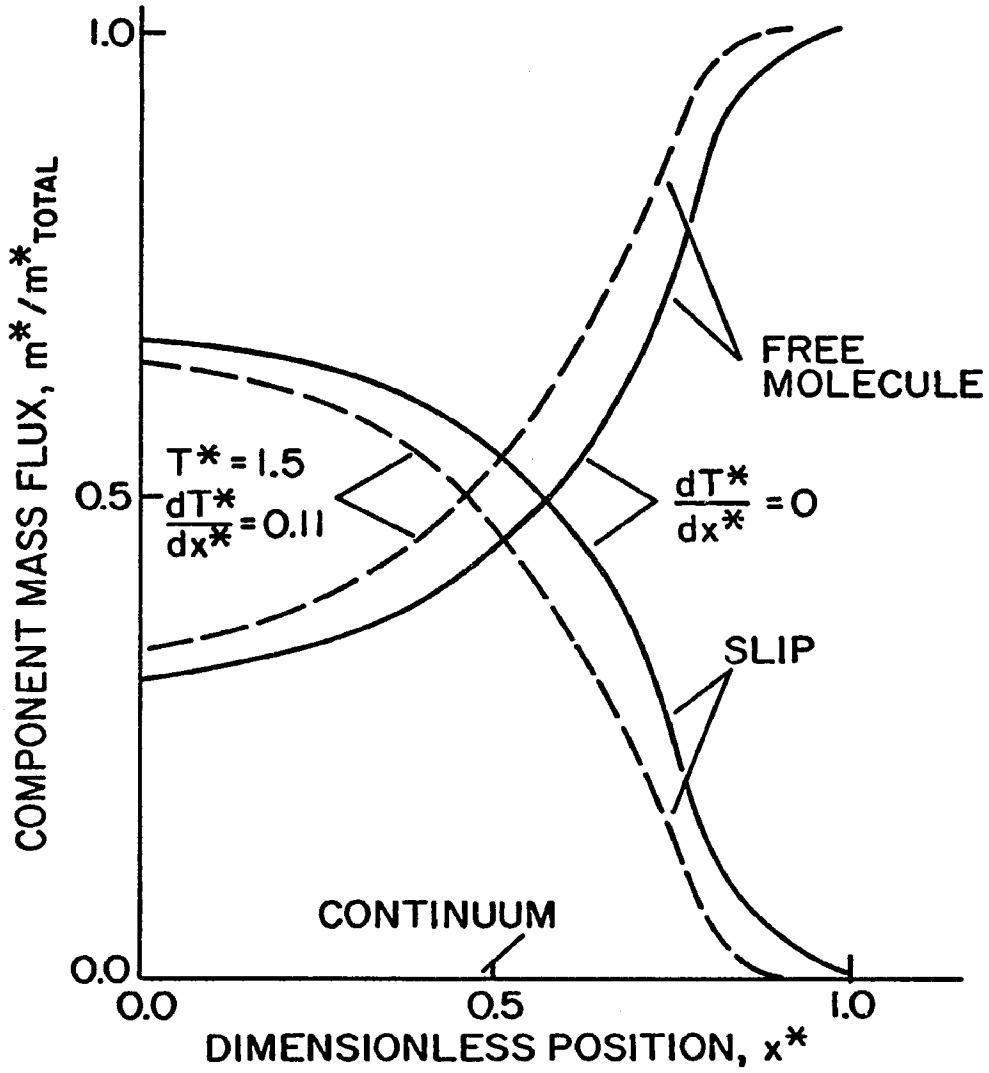

Figure 48 - Component Mass Fluxes, for FC-01, KN_r = 0.16, $\dot{m}^*$ = 2.3

as a function of position. The significant curve parameters are the component mass fractions, the reference Knudsen number, KN_r, and the dimensionless mass flux, $\mathring{m}^*$.

The reference Knudsen number, KN_r, by definition, is based upon the median pore diameter, the high pressure and low temperature of the system. As a result, it is only an indication of the flow regimes that will be encountered within the system. The local Knudsen number, KN, not the reference Knudsen number, determines the flow regime at a particular location and pore. As a result, the local Knudsen number varies with the mass flux that is forced through a medium, the state variables, and position. The reference Knudsen number is independent of the mass flux and position.

At very large values of the reference Knudsen number ($\gtrsim$ 50), continuum flow will dominate (Figure 44) and the slip and free molecule portions will be zero. At lower values of KN_r, slip flow can occur (Figure 45), and if reduced still further, free molecule flow can occur (Figures 46, 47, 48).

The effect of increasing the mass flux is also evident in Figure 45. The increased portion of slip flow at the higher mass is due to the increased pressure gradient required by the higher mass flux. A higher value of the dimensionless mass flux usually indicates that the flow portions will shift toward the free molecule regime, as seen in Figure 46. Figure 47 shows that this is not always the case. The definition of the non-dimensionalizing mass flux is based upon the continuum regime model and is proportional to the square of the median

pore diameter. In the free molecule regime, the flow is directly proportional to the median pore diameter. Thus, the dimensionless mass flux can become greater than unity (Figure 48) for a fine pored medium. Furthermore, the definition of the dimensionless mass flux does not take into account a complete description of the medium and therefore would not be expected to completely correlate data between different media.

The effect of increasing the average temperature of the system is to reduce the density, allowing slip and/or free molecule flow to occur at a lower value of the dimensionless position. The phenomenon is shown in Figures 46 and 48 as the broken lines.

5.5 Characteristics of the Model with Varying Model Parameters

The important model parameters are the probability exponent, N, the effective cumulative pore area, $\phi(a)$, and the cut-off Knudsen number.

The effect of changing the probability exponent upon the effective cumulative area distribution is shown in Figure 49. The median pore diameter typically decreases with increasing values of the probability exponent. Another characteristic is that the rate of change of the median pore diameter with respect to the probability exponent decreases with increasing values of the probability exponent. This can be seen in Figure 49 by noting that the median pore diameter at an exponent of 20 is much closer to the median at 30, than it is to the median at 10.

The value of the cut-off Knudsen number may or may not change the solution, depending upon the reference Knudsen number of the medium.

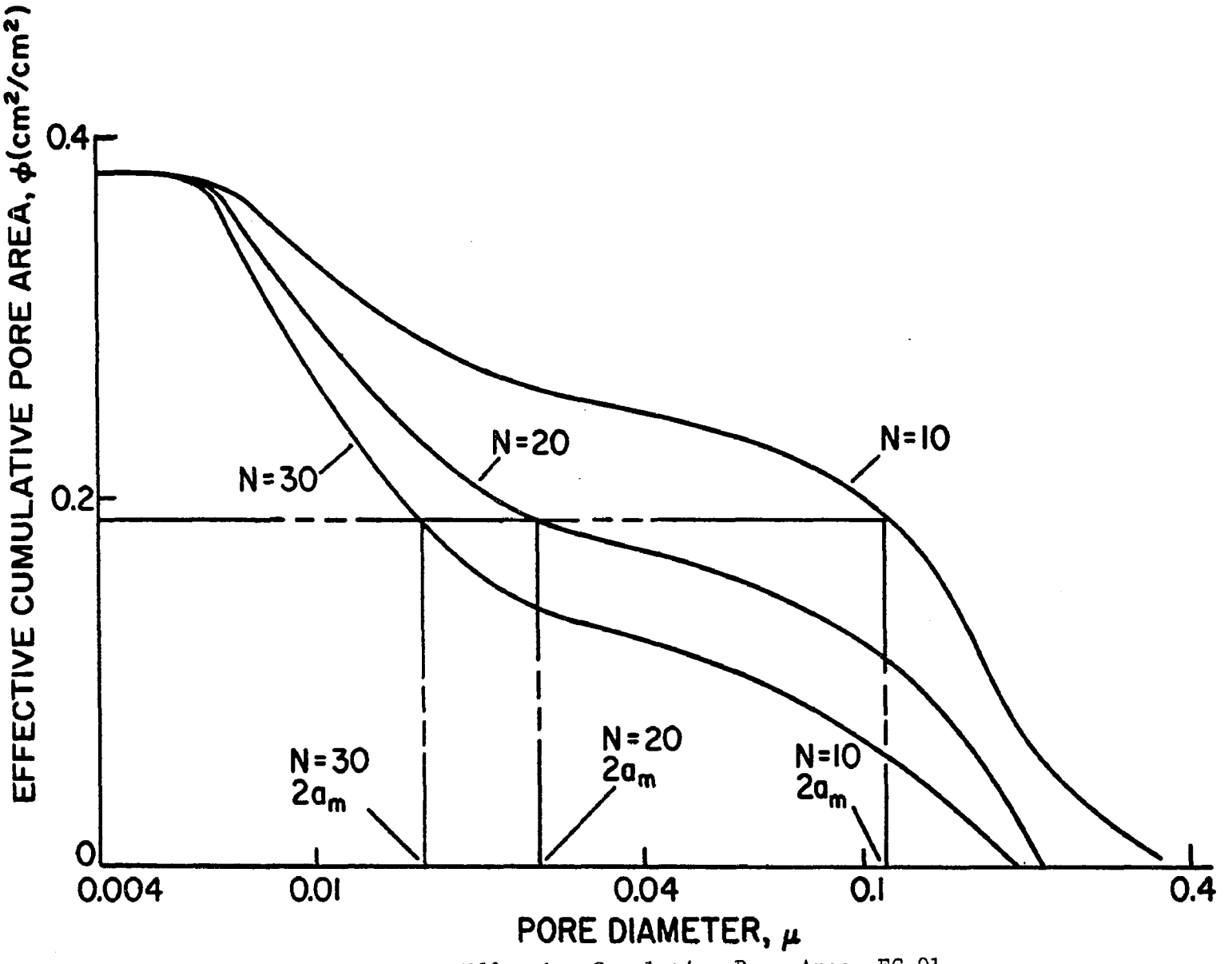

Figure 49 - Effect of Probability Exponent on Effective Cumulative Pore Area, FC-01

If the reference Knudsen number is large (> 10) (Figure 50), then the cut-off Knudsen number may be halved or doubled without an appreciable change in the solution. If, on the other hand, the reference Knudsen number is small (< 0.2) (Figure 51) and the cut-off Knudsen number is halved or doubled, a very pronounced change occurs in the solution. As the cut-off Knudsen number is decreased, the portion, at the inlet, of slip flow increases and the portion of free molecule flow decreases. At some distance from the inlet, the opposite effect is evident. Decreasing the cut-off Knudsen number has the effect of increasing the average pressure gradient. This can be observed in Figure 51 by noting that the thickness required to reach zero pressure decreases with decreasing cut-off Knudsen number with the mass flux held constant. The pressure gradient in the slip regime is proportional to the inverse of the square of the cut-off Knudsen number, KN_c. It is this relationship that causes the slip flow curve at a cut-off Knudsen number of five to cross the curves at larger values of KN_c.

The effect of changing the probability exponent upon the outlet pressure is shown in Figure 52. This behavior is typical of the porous media used in this study. The outlet pressure at constant mass flux decreases with increasing N because the effective diameter of the pores is decreasing (Figure 49) with increasing N.

The probability exponent is the key parameter in the model. Figure 53 shows a plot of the integer exponent values versus the logarithm of the median pore diameter. The four points represent a

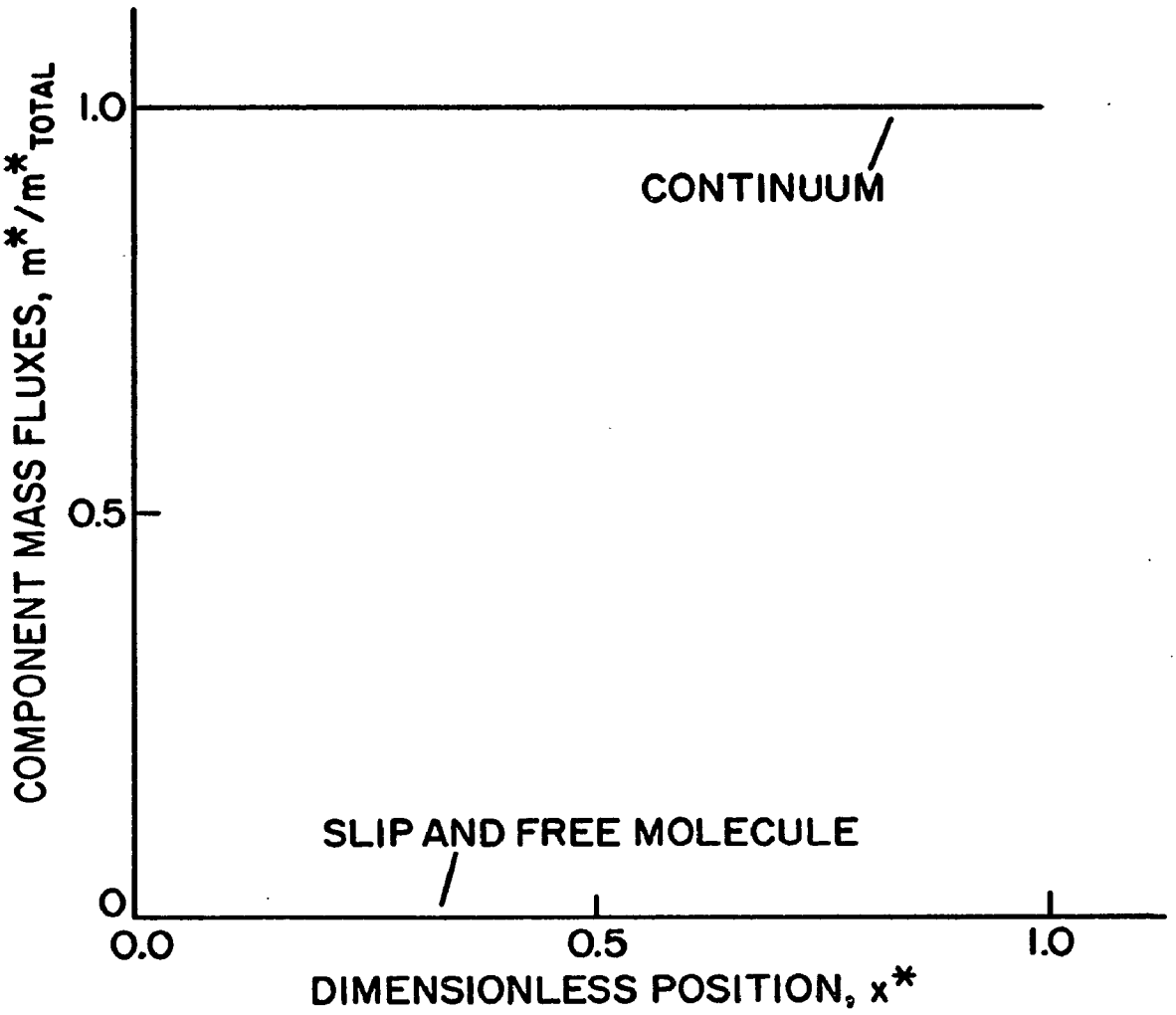

Figure 50 - Effect of Cut-Off Knudsen Number on the Mass Fractions of FC-11, $KN_r = 20$, $\dot{m}^* = .08 \times 10^{-3}$, $KN_c = 5, 10, 20$

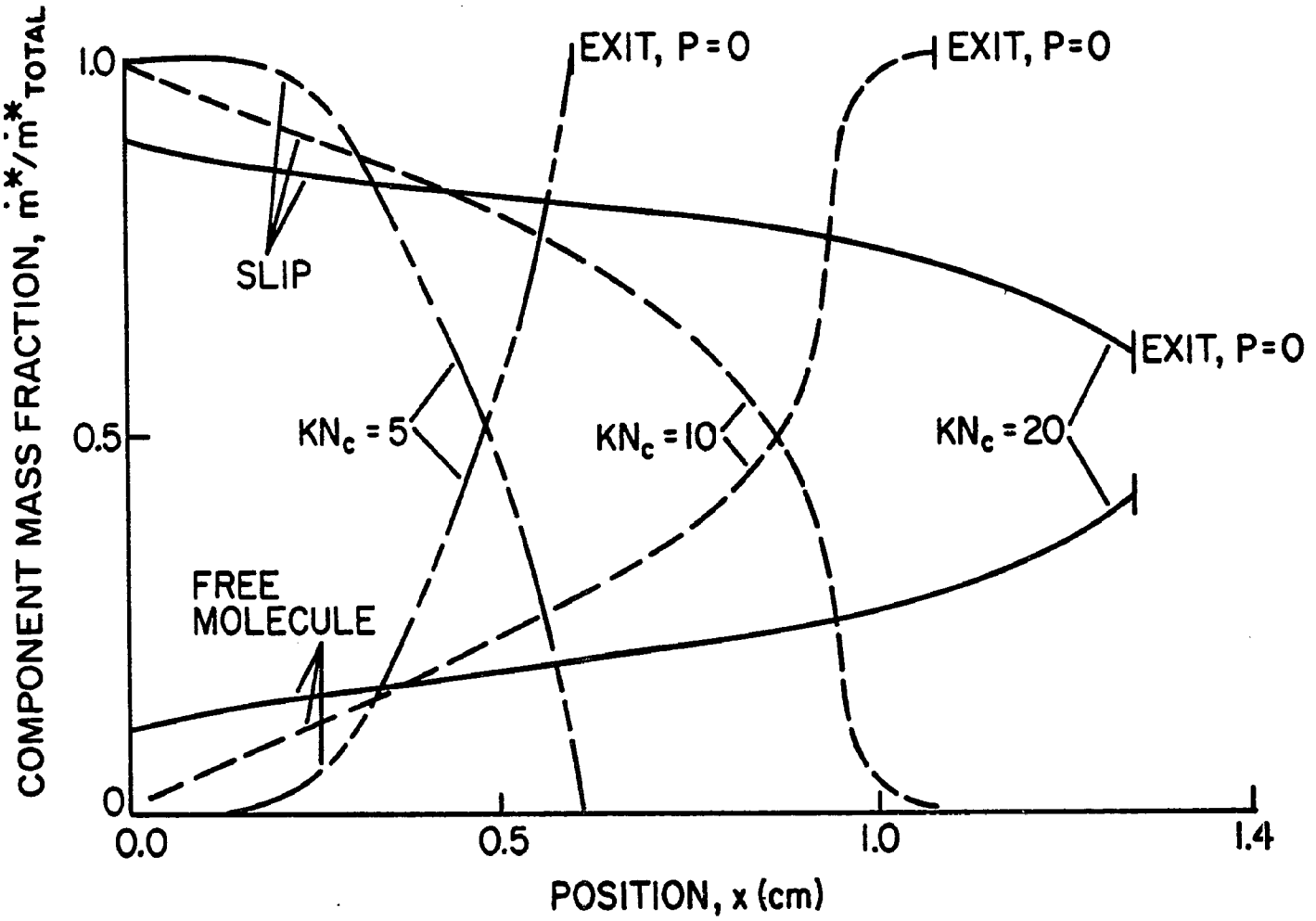

Figure 51 - Effect of Cut-Off Knudsen Number on the Isothermal Mass Fractions, FC-01, $KN_r = 0.2$, $\dot{m}^* = 2.3$

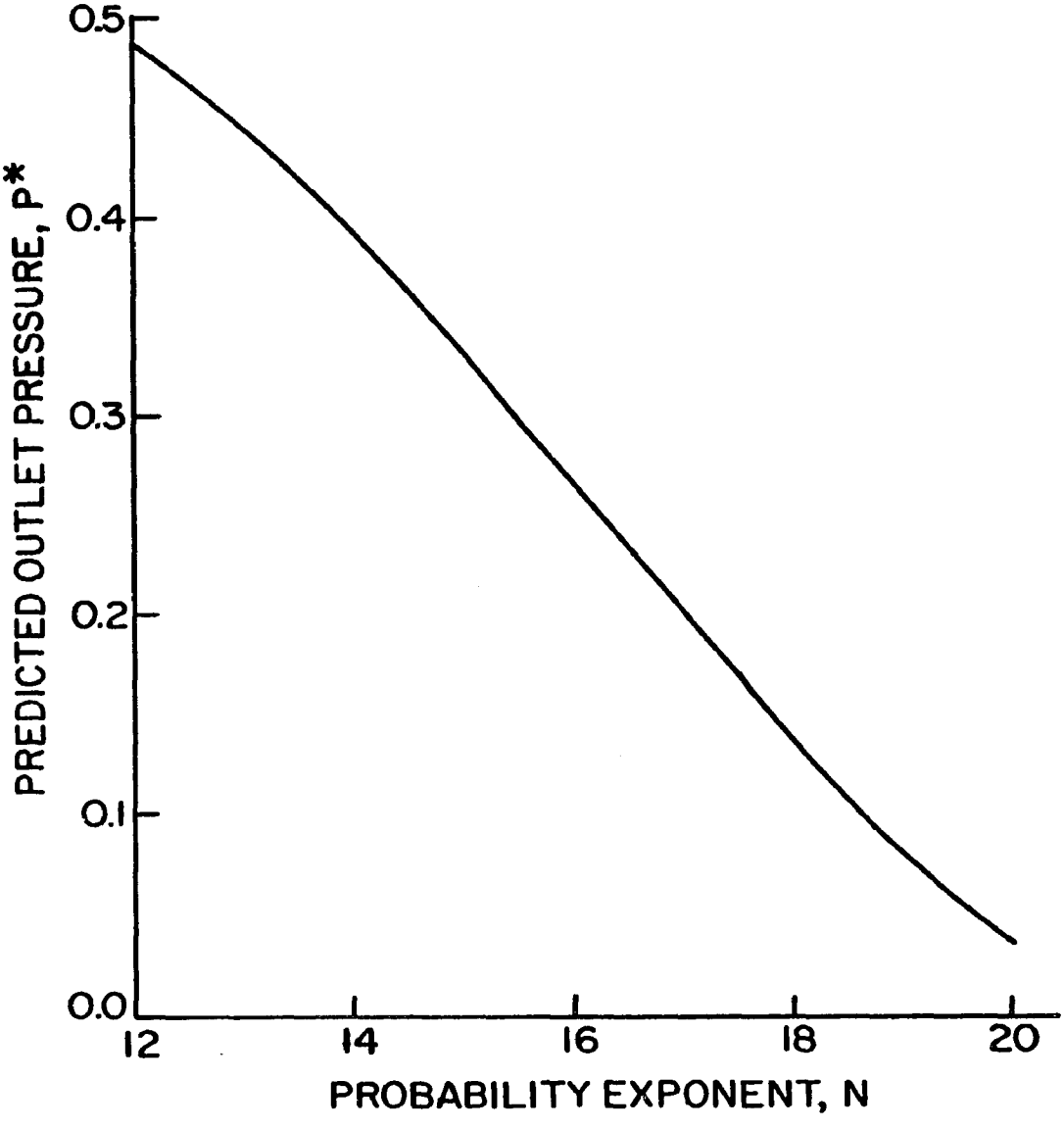

Figure 52 - Effect of Exponent N, on the Outlet Pressure

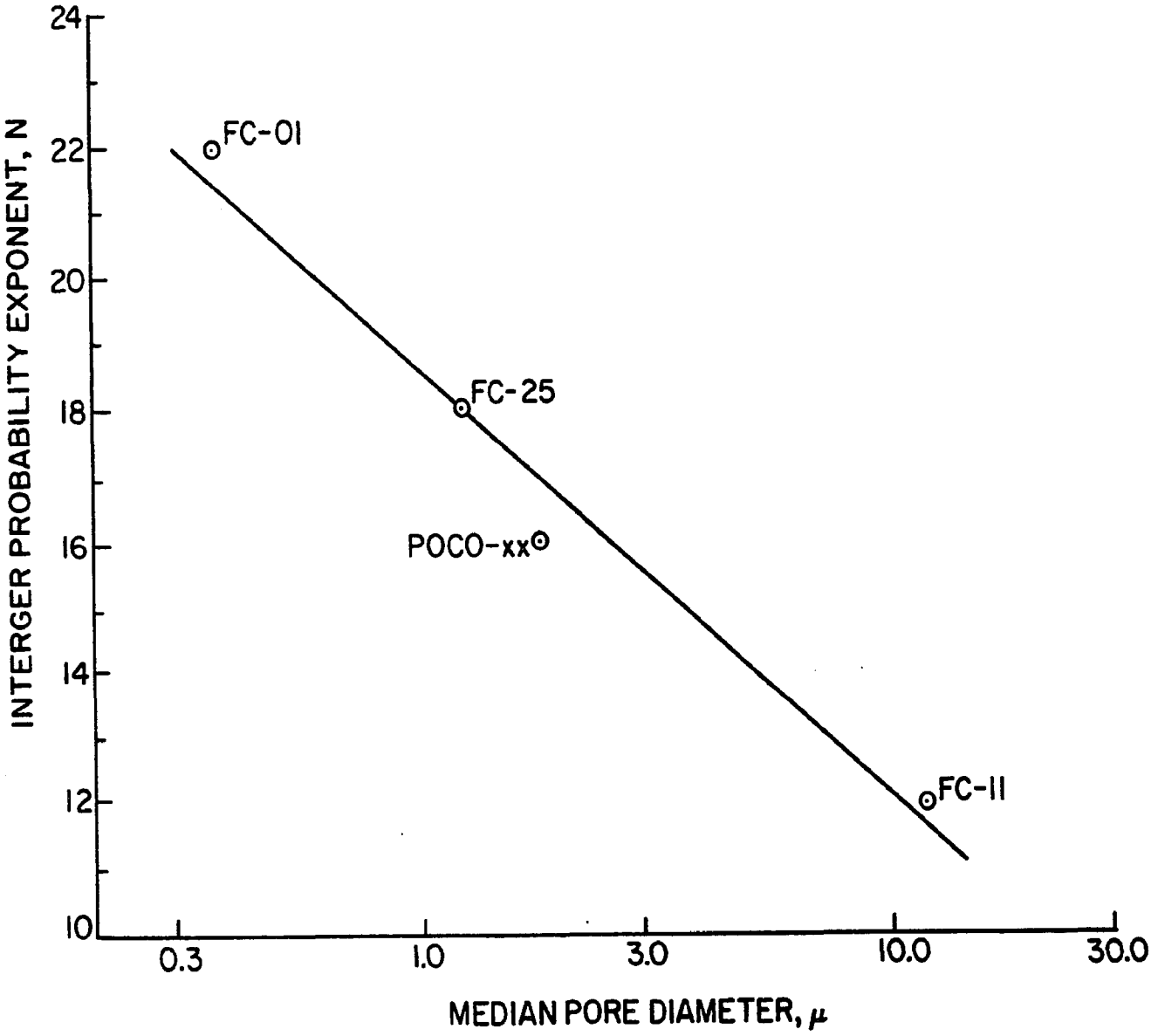

Figure 53 - Correlation of the Medium Pore Diameter and the Integer Probability Exponent

fairly straight line. The exponent plotted against the dimensionless resistance parameter, B [Equation (3.32)], is also approximately linear (Figure 54). Of the two correlations, the one between the medium resistance parameter and the probability exponent is preferred as this accounts for additional medium properties. This is felt to be particularly important when considering media manufactured by different firms.

5.6 Summary

A model of non-isothermal gaseous flow through fine pored media has been presented. The agreement between model and experiment under both isothermal and non-isothermal conditions was found to be good. The experimental and analytical permeability and pressure-position characteristics of four different porous media were presented. The analytical results predicting the component mass fluxes were presented. The scanning electron microscope and mercury porosimeter data predicted similar median pore diameters, but different cumulative areas. This discrepancy was hypothesized to be due to pores that were filled during the polishing process.

The model requires a knowledge of the cumulative porosity curve determined by a mercury porosimeter, gas properties, and inlet and outlet state conditions to predict the mass flux as a function of the medium thickness. The procedure for using the model is the following:

1. The cumulative pore area distribution is determined from the porosity curve.

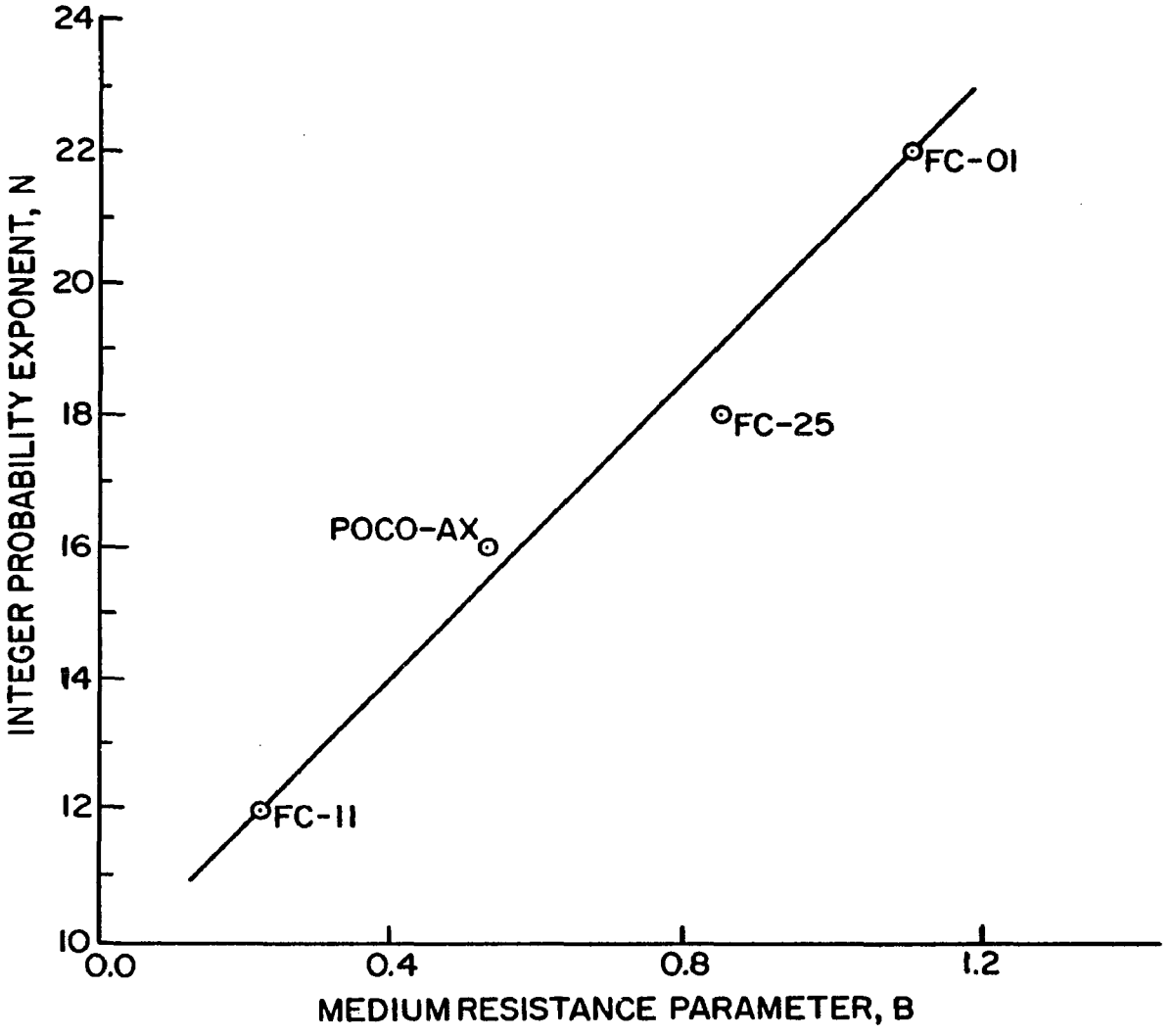

Figure 54 - Correlation of the Medium Resistance Parameter and the Integer Probability Exponent

2. The medium's resistance parameter is determined from the cumulative area curve.
3. The probability exponent is determined from Figure 54.
4. The effective cumulative pore area distribution is determined from the cumulative area distribution and the probability exponent.
5. The differential equation representing the model can then be solved with various mass fluxes, inlet conditions, and thickness.
6. Curves of the permeability versus the mean pressure can then be developed for both isothermal and non-isothermal conditions.
7. A typical mass flux can then be determined from the permeability curves knowing the inlet and outlet states and the desired medium thickness.

CHAPTER VI

SUMMARY AND CONCLUSIONS

6.1 Research Objective

The principle objectives of this research were to model a gaseous flow through a fine pored medium under non-isothermal conditions, to determine, evaluate and utilize the parameters that govern the flow, and to collect the necessary experimental data to verify the analytical model.

6.2 The Analytical Model

The analytical model consisted of two parts: a description of the medium itself, and a description of the mechanics of the gas within the medium. The description of the mass flux within a pore of the medium was obtained through the use of differential equations available in the literature for each of the three flow regimes; continuum, slip, and free molecule. The porous medium was modeled by calculating the probability of finding a pore of radius a or larger on the surface of the medium and multiplying by the probability that a pore of radius a or larger would go through N planes sequentially. The product of the two probabilities modeled the effective cumulative pore area distribution as a function of pore radius. The effective cumulative pore area distribution was used to characterize the flow area available to a differential thickness of the medium. The integral of the product of the effective differential cumulative pore area and the mass flux of a pore

in a particular flow regime yielded a differential equation which modeled the mass flux for the porous medium in that flow regime. The sum of these equations for the three flow regimes yielded a single differential equation in the pressure representing the total mass flux through the porous medium.

The differential equation so formed models the flow of a gas through a porous medium under both isothermal and non-isothermal conditions. The model requires a knowledge of the pore size distribution and temperature profile of the medium and the properties of the gas to predict the pressure displacement characteristics of a gas flowing through a porous medium under non-isothermal and isothermal conditions.

6.3 The Experimental Investigation

Porous media possessing a wide range of median pore diameters (0.4μ to 10μ) and of porosity (0.1 to 0.6 cc/gm) were investigated. Data were collected in all three flow regimes, but primarily in the continuum and slip regimes under both isothermal and non-isothermal conditions.

6.4 Summary and Conclusions

The major conclusions of this study, as presented in the preceding chapters, can be summarized as follows:

1. The model of the gas-porous medium system interaction predicts the behavior of the system with reasonable accuracy. The two fundamental assumptions of the model are

that the medium is homogeneous and that the pore size distribution as determined by the mercury penetration technique is accurate.

2. Additional research is required before a reliable cumulative pore area distribution can be obtained from Scanning Electron Microscope data. In particular, a polishing technique that does not fill the pores is required.

3. The model's probability exponent was found to vary approximately linearly with the medium resistance parameter.

4. The probability exponent of a medium should be determined from the medium's resistance parameter rather than the median pore diameter.

5. A large value (> 10) of the reference Knudsen number indicates that the medium can support continuum flow. A small value (< 0.1) indicates that free molecule flow will probably occur within the medium.

6. Increasing the average temperature of the system forces slip and free molecule flow to occur earlier in the medium than they would have at lower temperatures.

7. The temperature gradient does not influence the flow at high values of KN_r (> 10).

8. At low values of the reference Knudsen number the flow is aided by a positive temperature gradient and hindered by a negative one.
9. The temperature gradient primarily influences the measured fluxes by changing the physical properties of the gas.

6.5 Suggestions for Further Research

Additional studies would be desirable to provide data for the probability exponent-media resistance curve. The effect of gas properties on the flow should be investigated. An investigation of the permeability minimum would be of interest.

BIBLIOGRAPHY

1. Barrer, R. M., "Fluid Flow in Porous Media", Discussions, Faraday Society (1948), Vol. 3, p. 61.

2. Washburn, E. W., "The Dynamics of Capillary Flow", Physical Review (1921), Vol. 17, p. 273.

3. Washburn, E. W., Bunting, E. W., "Porosity: V Recommended Procedures for Determining Dorosity by Methods of Absorption", Journal American Ceramic Society,(1922), Vol. 5, p. 48.

4. Ritter H. L., Drake, L. C., "Pore Size Distribution in Porous Materials, Pressure Porosimeter and Determination of Complete Macropore-Size Distributions", Industrial and Engineering Chemistry, Analytical Edition, (1945), Vol. 17, p. 782.

5. Butterworth, B., The Structure and Properties of Porous Materials, (London: Butterworth Scientific Publications, 1958).

6. Cameron, A., Stacey, W. O., "Apparatus and Technique, A Low Pressure Mercury Porosity Meter", Chemistry and Industry, (1960), p. 222.

7. Scholten, J. J. F., "Mercury Porosimetry and Allied Techniques", in Carbon, (New York: Academic Press, 1967).

8. Orr, C., "Application of Mercury Penetration to Materials Analysis", Powder Technology, (1969), Vol. 3, p. 117.

9. Bickerman, J. J., Surface Chemistry, (New York: Academic Press, 1947, p. 322).

10. Winslow, N. M., Shapiro, J. J., "An Instrument for the Measurement of Pore Size Distribution by Mercury Penetration", American Society of Testing Materials Bulletin, February 1959, No. 236, p. 39.

11. White, E. H., Gorz, H., Johnson, G. G. and McMillan, R. E., "Particle Size Distributions of Particulate Aluminas from Computer-Processed SEM Images", Scanning Electron Microscopy/1970, Proceedings of the Third Annual Scanning Electron Microscope Symposium, Chicago (1970), p. 59.

12. Scheidegger, A. E., The Physics of Flow Through Porous Media, (Toronto: University of Toronto Press, 2nd Edition, 1960).

BIBLIOGRAPHY (CONT.)

13. Rohsenow, W. M., Choi, H., Heat, Mass, and Momentum Transfer, (Englewood Cliffs: Prentice-Hall, 1961, p. 283).

14. Carman, P. C., Flow of Gases Through Porous Media, (London: Butterworths, 1956).

15. Millikan, R. A., "Coefficients of Slip in Gases and the Law of Reflection of Molecules from the Surfaces of Solids and Liquids", Physical Review, V. 1923, Vol. 21, p. 217.

16. Klinkenbeg, L. J., "Drilling and Production Practice", Discussions of American Petroleum Institute, 1941, p. 200.

17. Hanley, H. J. M., Experimental Verification of the Dusty Gas Theory for Thermal Transpiration", Journal of Chemical Physics, 1965, Vol. 43, p. 1510.

18. Grove, D. M., "Permeability and Flow Studies" in Carbon, (New York: Academic Press, 1967, p. 155).

19. Carman, P. C. and Arnell, J. C., "Surface Area Measurements of Fine Powders using Modified Permeability Equations", Canadian Journal of Research, 1948, Vol. A-26, p. 128.

20. Adzumi, H., "On the Flow of Gases Through a Porous Wall", Bulletin of the Chemical Society of Japan, 1937, Vol. 12, p. 304.

21. Holmes, W. R., "Flow of Gases Through Fine Powders and the Measurement of Specific Surface", Nature, London, 1946, Vol. 157, p. 694.

22. Carman, P. C., Flow of Gases Through Porous Media, (London: Butterworths, 1956, p. 69).

23. Hutcheon, J. M., Longstaff, B. and Warner, R. K. in Society of Chemical Industry Sumposium on Industrial Carbon and Graphite, 1958, p. 259.

24. Barrer, R. M., Strachan, E., "Sorption and Surface Diffusion in Microporous Carbon Cylinders", Proceedings of the Royal Society, 1955, Vol. A-231, p. 52.

25. Grove, D. M., Ford, M. G., "Evidence for Permeability Minima in Low Pressure Gas Flow Through Porous Media", Nature, London, 1958, Vol. 132, p. 999.

BIBLIOGRAPHY (CONT.)

26. Ash, R., Grove, D. M., "Low Pressure Gas Flow in Consolidated Porous Media", Transactions of the Faraday Society, 1960, Vol. 56, p. 1357.

27. Owen, J. E., "Experimental Determination of the Tortuousity", Transactions American Institute of Mechanical Engineerings, 1952, Vol. 195, p. 169.

28. Hewitt, G. F., "Further Techniques for the Study of Pore Structure by Liquid Metal Penetration" in Carbon, (New York: Academic Press, 1967, p. 203).

29. Pollard, W. G., Present, R. D., "On Gaseous Self-Diffusion in Long Capillary Tubes", Physical Review, 1948, Vol. 73, p. 762.

30. Lammers, G. B., "The application of Thermal Transpiration to a No-Moving Part Pump", Ph.D. Thesis, Mechanical Engineering, Case Western Reserve University, 1969.

31. Evans, R. B., Watson, G. M., Mason, E. A., "Gaseous Diffusion in Porous Media at Uniform Pressure", Journal of Chemical Physics, 1961, Vol. 35, 6, p. 2076.

32. Evans, R. B., Watson, G. M., Mason, E. A., "Gaseous Diffusion in Porous Media II, Effect of Pressure Gradients", Journal of Chemical Physics, 1962, Vol. 36. p. 1894.

33. Evans, R. B., Watson, G. M., Mason, E. A., "Gaseous Diffusion in Porous Media III, Thermal Transpiration", Journal of Chemical Physics, 1963, Vol. 38, p. 1808.

34. Weber, S., "Uber Den Zusammen Hang Zwischen Der Laminaren Stromung Der Reinen Gas Durch Rohre und Dem Selbstdiffusionskoeffizienten", in Det Kongelige Danske Videnskabernes Selskab, Matematisk-Fysiske-Meddelelser, 1954, Vol. 28, No. 2.

35. Liang, S. C., "On the Calculation of Thermal Transpiration", Candian Journal of Chemistry, 1955, Vol. 33, p. 279.

36. Broadbent, S. R., and Hammersley, J. M., "Percolation Processes in Crystals and Mazes", Proceedings of Cambridge Philosophical Society, 1957, Vol. 53, p. 629.

37. Sutherland, W., "The Viscosity of Gases and Molecular Force", Philosophical Magazine, 1893, Vol. 36, Ser. 5, p. 507.

BIBLIOGRAPHY (CONT.)

38. Kennard, E. H., Kinetic Theory of Gases, (New York: McGraw-Hill, 1937, p. 293).

39. Kennard, E. H., Kinetic Theory of Gases, (New York: McGraw-Hill, 1937, p. 331).

40. Rosenow, W. M., Choi, H., Heat, Mass and Momentum Transfer, (Englewood Cliffs, Prentice Hall, 1961, p. 28).

41. Ralston, A., "Numberical Integration Methods for the Solution of Ordinary Differential Equations" in Mathematical Methods for Digital Computers, (New York: John Wiley and Sons Inc., 1967, p. 95).

42. Kunz, K. S., Numerical Analysis, (New York: McGraw-Hill, 1957, p. 187).

43. Hanley, H. J. M., Steele, W. A., "Low Pressure Flow of Gases", Journal of Physical Chemistry, 1965, Vol. 68 (10), p. 3087.

44. Hurst, C. J., "Transient Droplet Growth During Dropwise Condensation", Ph.D. Thesis, The Pennsylvania State University, 1966.

APPENDIX A

THE BARNES R8T1 INFRARED RADIOMETER

A.1 Background

The R8T1 infrared radiometer used in the experiments was designed to measure the radiance (watts/cm^2-ster) of a surface over an area 0.040 inches in diameter, at an optical distance of 40 inches. The target (the surface being viewed) radiance, $\overline{N}_t$, is computed from a knowledge of the system electronic gain, G, the system response factor, K_r, the reference radiance, $\overline{N}_r$, the background radiance, $\overline{N}_c$, the optical balance factor, ao the focal loss factor, l_f, the attenuation factor, SA, the output voltage, V_{out}, and the Electronic Temperature Offset voltage, V_{ETO}. The emissivity of the targets (carbon samples) was assumed to be unity because the surfaces of the samples were rough, black and inserted in a cavity. The results that follow bear out this assumption.

The Barnes R8T1 infrared radiometer is an extremely versatile device in that the sensitivity of the device can be varied from approximately 1 volt per $^{\circ}$C to 0.005 volts/$^{\circ}$C. In the experiments performed here, a sensitivity of approximately 0.005 volts/$^{\circ}$C was used. It should be noted a small temperature range ($\pm 5^{\circ}$C). Use of the instrument over a large temperature range ($\pm 100^{\circ}$C), although possible, is considerably more difficult and also not as reliable as when used at high sensitivities.

Hurst (44) measured the time constant of the R8T1 and found it to always be less than 0.2 seconds. This was judged to be sufficient to follow the transient warmup of the sample.

A.2 The Performance Equation

The performance equation allows one to calculate the target radiance, $\overline{N}_t$, from a knowledge of the system calibration factors, G, and K_s; the electronic settings of the instrumentation, SA, V_{ETO}, l_f, $\overline{N}_r$, ao; the output voltage, V_{out} and the background radiance, $\overline{N}_c$.

The performance equation is:

$$\overline{N}_t = \overline{N}_r + \frac{1}{l_f K_r}\left(\frac{SA}{G} V_{out} - V_{ETO}\right) - \frac{(l_f - ao)}{l_f} \overline{N}_c \quad . \tag{A-1}$$

The temperature of the reference blackbody was determined from Figure 55 and the heater setting chosen. Then the reference blackbody radiance, N_r, was determined from the effective radiance curve of the detector, Figure 56, provided with the instrument. The maximum background radiance was determined from the effective radiance curve, Figure 56, with the knowledge of the background temperature. The focal loss factor, l_f, was determined from the calibration curve, Figure 57, at a setting of 42 inches. The optical balance factor, ao, set at the factory, was assumed to be unity. The electronic temperature offset voltage is chosen by setting a ten turn potentiometer at a desired value. A three-position switch multiplies the potentiometer setting by one, zero, and minus one, respectively. The attenuation factor

$$SA = \log_{10}{}^{-1}(F/20) \quad , \tag{A-2}$$

where F is the setting of the attenuator contro. The output voltage, V_{out} is measured on a Dymec integrating digital voltmeter. The system

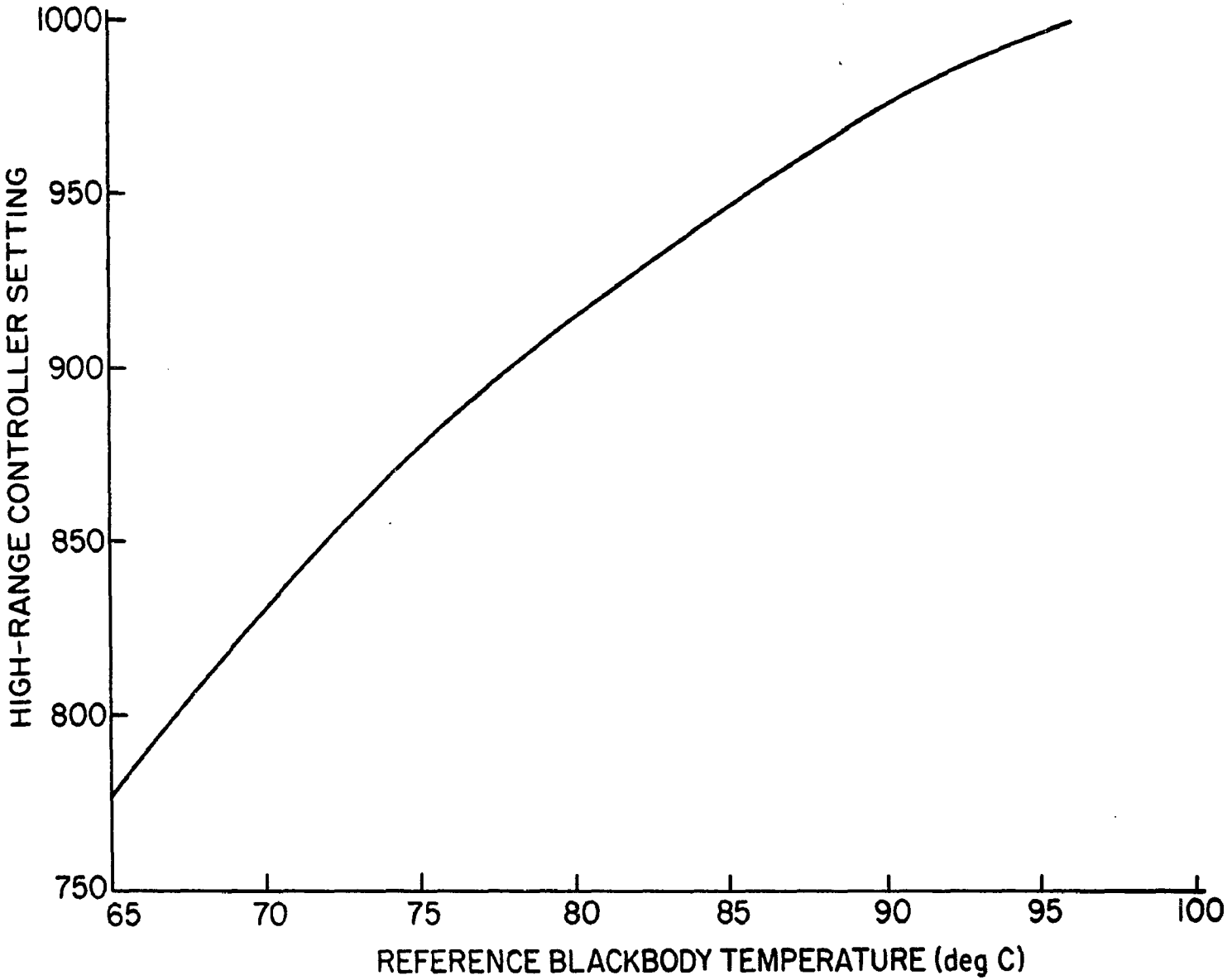

Figure 55 - Heater Controller Setting Versus Reference Blackbody Temperature

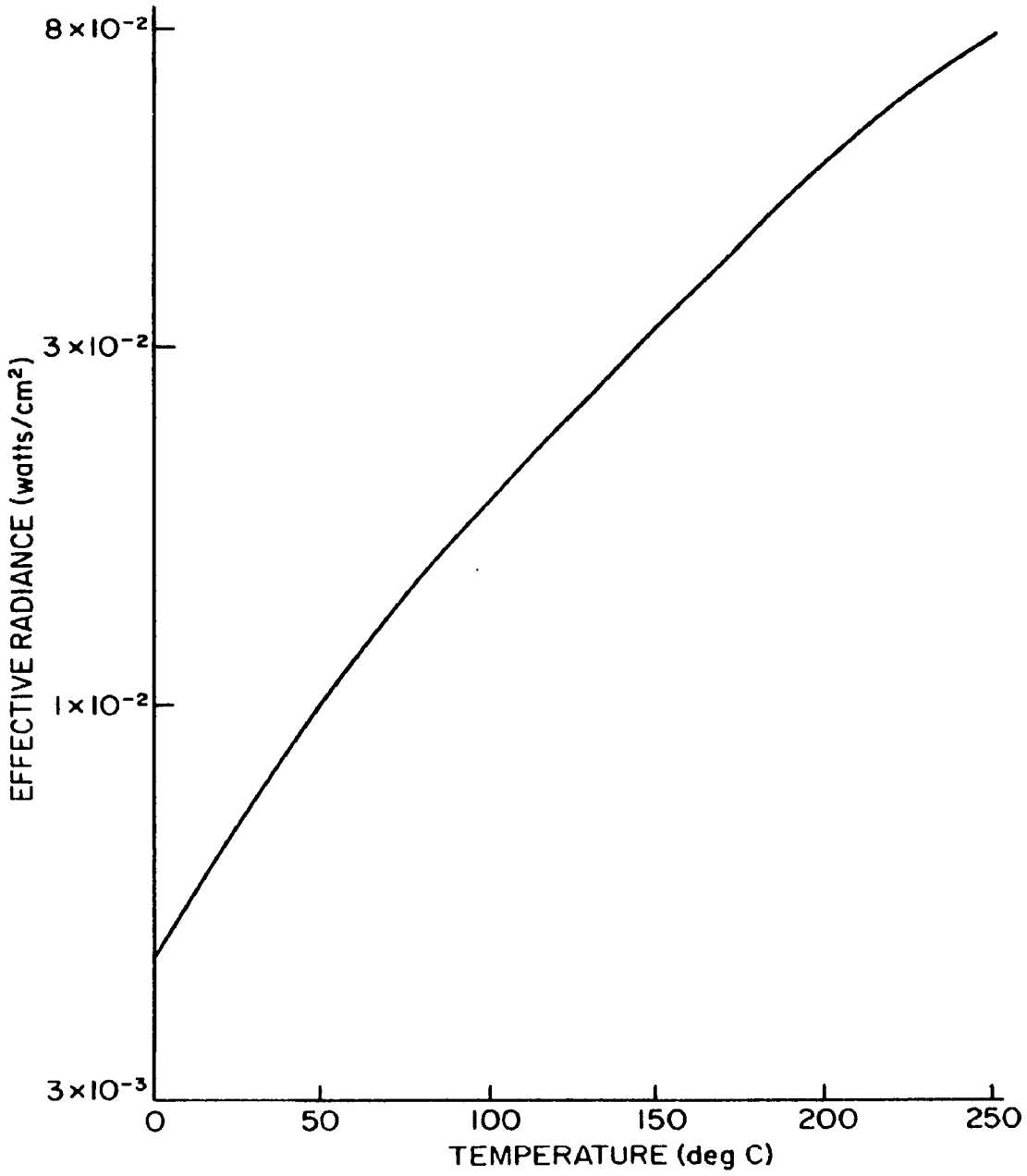

Figure 56 - Effective Radiance Versus Temperature

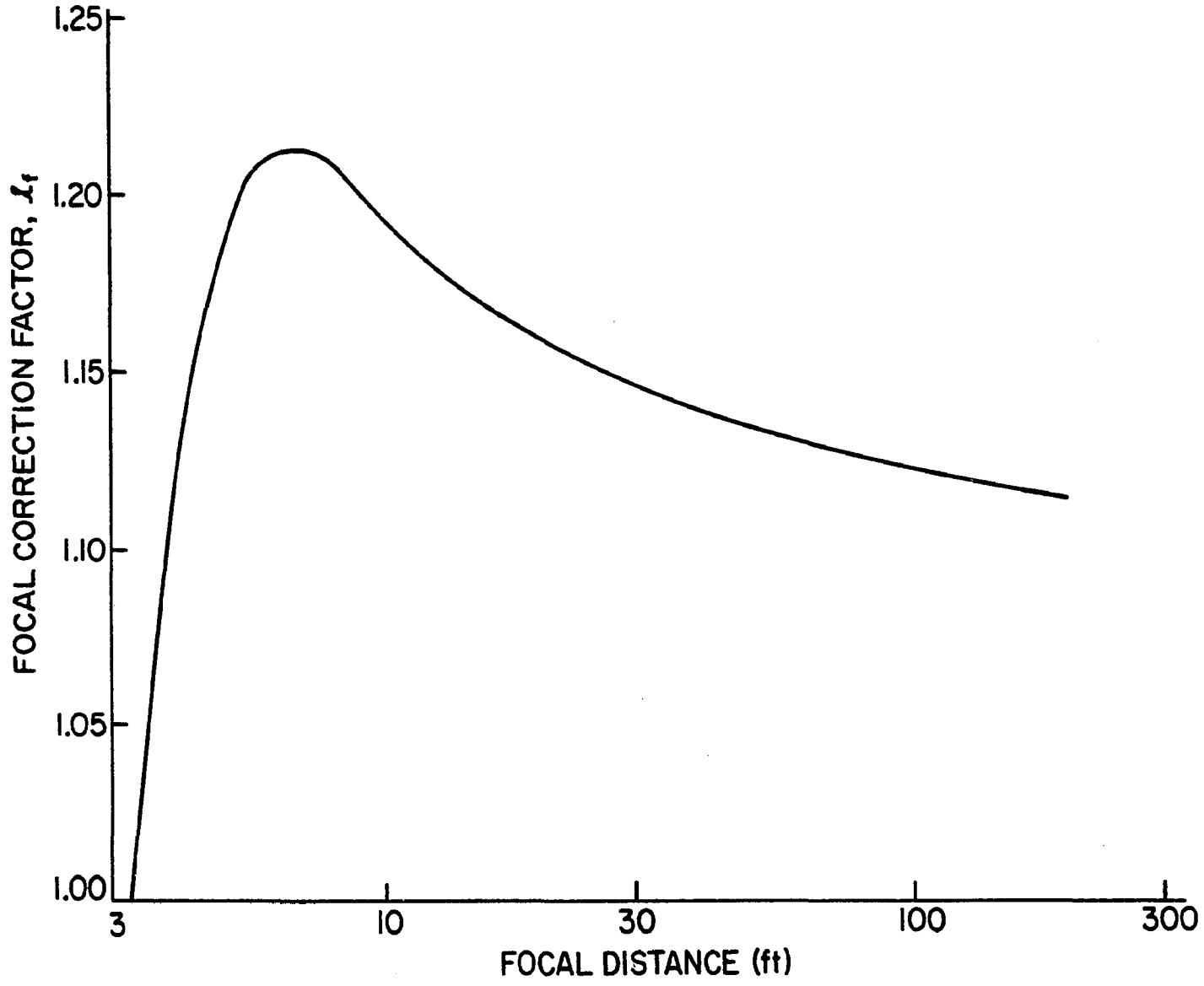

Figure 57 - Focal Correction Factor, l_f, Versus Distance

response factor, K_r and electronic gain, G were determined following the calibration procedures outlined in the R8T1 instruction manual. The value of the system response factor K_r, was found to be 5.4×10^{-2} cm^2 ster/watt-volt, with the salt windows in the optical path of the radiometer. The electronic gain, G, was 0.97×10^{6} volt/volt.

A.3 Sample Determination of the Target's Radiance and Temperature

The following data are assumed for the purposes of demonstration:

1. Focal distance: 42 inches
2. Background temperature: 25°C
3. $K_s = 5.4 \times 10^{-2}$ cm^2ster/watt volt
4. $G = 0.97 \times 10^{6}$ volt/volt
5. Attenuator control setting: 60
6. Heater setting: 1000
7. Electronic Temperature Offset, $+ 1000 \times 10^{-6}$ volts
8. Output voltage, 3.41 volts

Using the above data and Figures 55, 56, and 57, the components of Equation (A-1) can be evaluated. From Figure 57 with Item 1 above we find that the focal loss factor, l_f has a value of 1.05. The blackbody reference temperature, Figure 55, has a value of 95°C at a heater setting of 1000. The background radiance, $\overline{N}_c$ and the blackbody reference radiance, $\overline{N}_r$, are found on Figure 56 and have values of 0.7×10^{-2} and 1.8×10^{-2} watts/cm^2ster at their respective temperatures. The attenuation factor, SA is determined from Equation (A-2) and found to have a value of 1000. Substituting the above values into Equation (A-1), we find that:

$$\bar{N}_t = 1.8 \times 10^{-2} + \frac{1}{(1.05)(5.4\times10^{-2})}\left[\frac{1000}{0.97\times10^{-6}}(3.41)-1000\times10^{-6}\right]$$

$$\frac{(1.05-1)}{1.05}\,(0.7\times10^{-2}) \quad , \qquad \text{(A-3)}$$

or

$$\bar{N}_t = 6.41 \times 10^{-2} \text{ watts/cm}^2\text{ster} \quad . \qquad \text{(A-4)}$$

The temperature of the target is then determined from Figure 56 and found to be 220°C.

A.4 A Comparison Between the Radiometer and Thermocouple Surface Temperatures

A thermocouple was buried just beneath the surface of the sample (at an x/L of 0.85). Since the solution to the energy equation is known, the heated surface temperature can be determined if the cooled surface and thermocouple temperatures are known.

A comparison of the surface temperatures as computed from the thermocouple and radiometer data is shown in Figure 58. The data all fall well within a ±5% deviation line and around the 45° line representing 100% correlation. The data are plotted as absolute temperatures, as it is these values that control the flow rate. The flow in the continuum regime is approximately inversely proportional to the temperature raised to the three halves power; thus, an error of 5% could influence the flow by as much as 7.6%. The influence in the free molecular regime is less significant as the error is inversely proportional to the temperature.

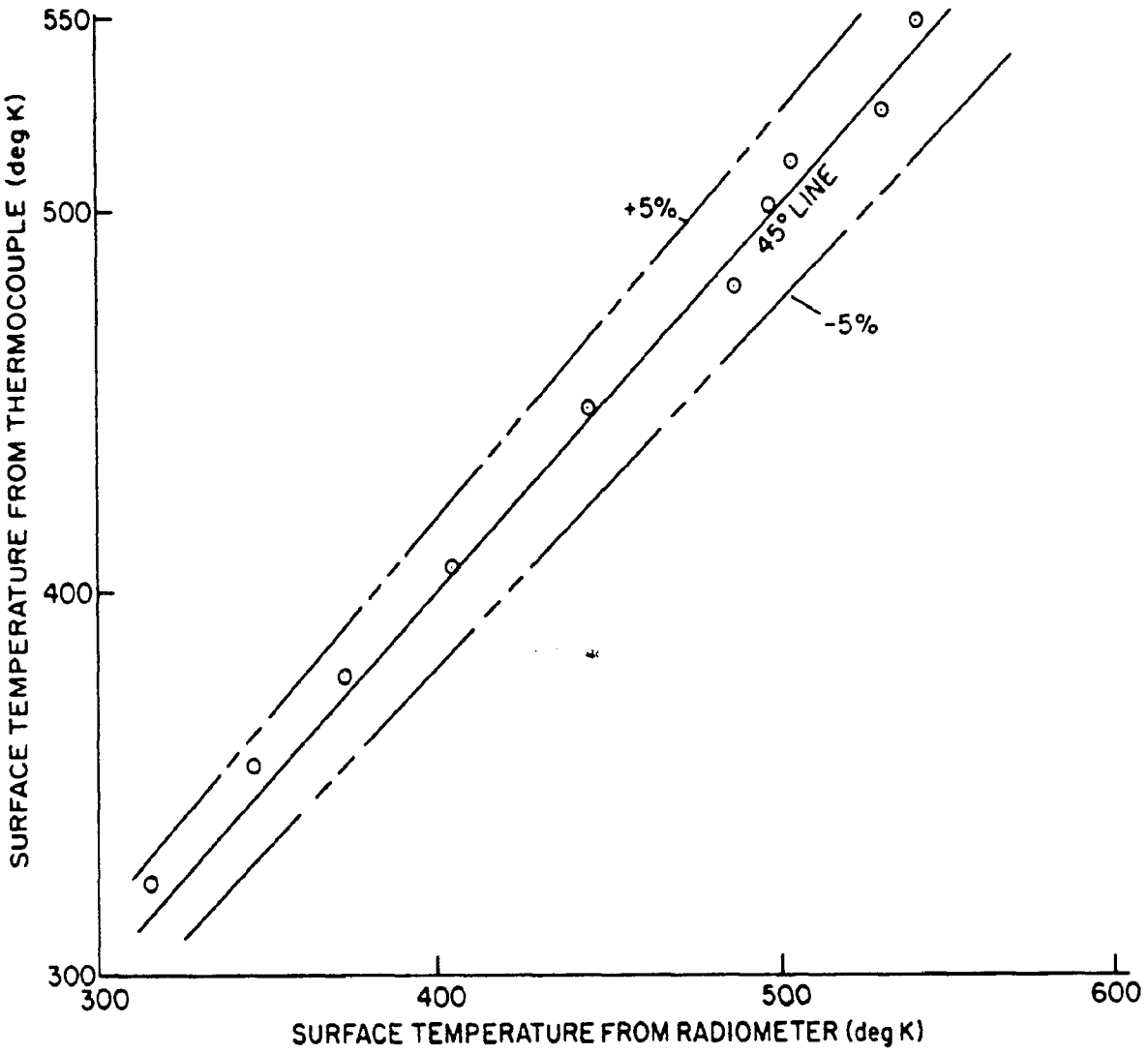

Figure 58 - Comparison of Surface Temperature Measurement Techniques

The results shown in Figure 58 indicate that the surface temperature of the sample can be determined using the radiometer, particularly at temperatures above 350°K (77°C), as the maximum error encountered under these conditions was less than 2%. The minimum surface temperature measured in the non-isothermal tests was 70°C. A surface temperature lower than 70°C could probably be determined accurately if the blackbody reference temperature and attenuation factors were changed. This was not done in the experiments because of a desire to keep constant as many parameters as possible.

APPENDIX B

EXPERIMENTAL TABULAR DATA

The following tables are a compilation of the experimental data collected and presented in the text in Figures 33 through 36 and 39 through 43.

TABLE VI

DATA OF FIGURE 33 - PERMEABILITY, FC-11

Permeability cm^2/min	Mean Pressure Atmospheres	$\bar{T}$ °K	dT/dx °C/cm
900.	1.09	300.0	0.0
858.	0.99	↓	↓
765.	0.90	↓	↓
590.	0.70	↓	↓
485.	0.57	↓	↓
455.	0.53	↓	↓
785.	1.20	350.0	+16°C/cm
595.	0.90	↓	↓
425.	0.65	↓	↓
405.	0.61	↓	↓

TABLE VI (CONT.)

DATA OF FIGURE 33 - PERMEABILITY, FC-11

Permeability	Mean Pressure	$\overline{T}$	dT/dx
cm^2/min	Atmospheres	°K	°C/cm
590.	1.20	425.	+33.
455.	0.89	↓	↓
379.	0.74	↓	↓
304.	0.61	↓	↓

TABLE VII

DATA OF FIGURE 34 - PERMEABILITY - POCO-AX

Permeability	Mean Pressure	$\overline{T}$	dT/dx
cm^2/min	Atmospheres	°K	°C/cm
110.0	0.97	300.	0.
80.5	0.71	↓	↓
61.5	0.54	↓	↓
70.5	0.95	425.	40.
52.5	0.72	↓	↓
37.1	0.53	↓	↓
71.0	0.95	425.	40.
53.0	0.72	↓	↓
34.5	0.54	↓	↓

TABLE VIII

DATA OF FIGURE 35 - PERMEABILITY - FC-25

Permeability cm^2/min	Mean Pressure Atmospheres	$\overline{T}$ °K	dT/dx °C/cm
3.00	0.81	300.	0.
2.37	0.58	↓	↓
1.06	0.20	↓	↓
2.14	0.85	340.	35.
1.61	0.56	↓	↓
0.72	0.20	↓	↓
2.08	0.85	340.	-35.
1.54	0.57	↓	↓
0.68	0.21	↓	↓

TABLE IX

DATA OF FIGURE 36 - PERMEABILITY FC-01

Permeability cm^2/min	Mean Pressure Atmospheres	$\overline{T}$ °K	dT/dx °C/cm
1.35	0.91	300.	0.
1.14	0.70	↓	↓
0.95	0.51	↓	↓
0.77	0.28	↓	↓
0.69	0.14	↓	↓
1.08	0.92	425.	86.
0.91	0.71	↓	↓
0.78	0.50	↓	↓
0.62	0.26	↓	↓
0.62	0.15	↓	↓
1.09	0.92	425.	-86.
0.94	0.71	↓	↓
0.74	0.51	↓	↓
0.58	0.25	↓	↓
0.55	0.16	↓	↓

TABLE X

DATA OF FIGURE 39 - PRESSURE - FC-11

Pressure	Position	$\overline{T}$	dT/dx
Atmospheres	Dimensionless	°K	°C/cm
1.0	0.0	300.	0.
0.98	0.25	↓	↓
0.97	0.50	↓	↓
0.965	1.00	↓	↓
0.65	0.0	300.	0.
0.64	0.25	↓	↓
0.64	0.50	↓	↓
0.63	1.00	↓	↓
1.00	0	425.	+33
0.64	0.25	↓	↓
0.63	0.50	↓	↓
0.62	1.00	↓	↓
0.65	0	425.	+33
0.64	0.25	↓	↓
0.63	0.50	↓	↓
0.62	1.00	↓	↓
1.00	0.0	425.	-33.
0.97	0.25	↓	↓
0.96	0.50	↓	↓
0.96	1.00	↓	↓

TABLE X (CONT.)

DATA OF FIGURE 39 - PRESSURE - FC-11

Pressure	Position	$\overline{T}$	dT/dx
Atmospheres	Dimensionless	°K	°C/cm
0.65	0.0	425.	-33.
0.64	0.25	↓	↓
0.63	0.50	↓	↓
0.62	1.00	↓	↓

TABLE XI

DATA OF FIGURE 40 - PRESSURE - POCO-AX

Pressure	Position	$\overline{T}$	dT^*/dx^*
Dimensionless	Dimensionless	Dimensionless	
1.0	0	1.0	0.0
0.99	0.25	↓	↓
0.98	0.50	↓	↓
0.97	1.00	↓	↓
1.0	0	1.4	+0.172
0.98	0.25	↓	↓
0.97	0.50	↓	↓
0.95	1.00	↓	↓
1.0	0	1.4	-0.172
0.98	0.25	↓	↓
0.97	0.50	↓	↓
0.95	1.00	↓	↓

TABLE XII

DATA OF FIGURE 41 - PRESSURE - FC-25

Outlet Pressure	Position	$\overline{T}$	dT*/dx
Dimenionless	Dimensionless	Dimensionless	
1.00	0.00	1.0	0.
0.85	0.25	↓	↓
0.75	0.50	↓	↓
0.43	1.00	↓	↓
1.00	0.00	1.27	.156
0.80	0.25	↓	↓
0.58	0.50	↓	↓
0.19	1.00	↓	↓
1.0	0.00	1.27	-0.156
0.80	0.25	↓	↓
0.58	0.50	↓	↓
0.18	1.00	↓	↓

TABLE XIII

DATA OF FIGURE 42 - PRESSURE - FC-01

Pressure	Position	$\overline{T}^*$	dT^*/dx^*
Dimensionless	Dimensionless	Dimensionless	
1.00	0.0	1.0	0.0
0.60	0.5	↓	↓
0.24	1.0	↓	↓
1.0	0.0	1.53	+0.37
0.56	0.5	↓	↓
0.09	1.0	↓	↓
1.0	0.0	1.53	-0.37
0.55	0.5	↓	↓
0.08	1.0	↓	↓

TABLE XIV

DATA OF FIGURE 43 - PRESSURE - FC-01

Pressure	Position	$\overline{T}^*$	dT^*/dx^*
Dimensionless	Dimensionless	Dimensionless	
1.00	0.0	1.0	0.0
0.75	0.25	↓	↓
0.41	0.50	↓	↓
0.10	1.00	↓	↓
1.00	0.0	1.53	+0.37
0.75	0.25	↓	↓
0.39	0.50	↓	↓
0.09	1.00	↓	↓
1.00	0.00	1.53	-0.37
0.75	0.25	↓	↓
0.32	0.50	↓	↓
0.04	1.00	↓	↓

VITA

Mason Harold Somerville was born in Worcester, Massachusetts, December 21, 1941. He graduated from Worcester Academy, Worcester, Massachusetts, in 1959. He then attended Worcester Polytechnic Institute, Worcester, Massachusetts, where he earned the degree of Bachelor of Science in Mechanical Engineering in 1964. He then accepted a position as a Graduate Teaching Assistant in the Department of Mechanical Engineering at Northeastern University. He subsequently was awarded the degree of Master of Science in Mechanical Engineering in 1966 by Northeastern University. In 1966, he accepted a position as a Graduate Research Assistant in the Department of Mechanical Engineering at The Pennsylvania State University and began his work toward the Doctor of Philosophy in Mechanical Engineering. In 1967, he accepted a position as Instructor of Mechanical Engineering at The Pennsylvania State University and continued his work toward the Doctor of Philosophy part-time. Upon the completion of his doctoral studies in 1971, he accepted a position as a Senior Engineer with The Westinghouse Electric Corporation.

As an undergraduate at Worcester Polytechnic Institute, he received the Peel Prize in 1963 and placed first in the American Society of Mechanical Engineers student paper contest. He is a member of the Society of Automotive Engineers, the American Society of Mechanical Engineers and Sigma Xi.